Interventional Perfusion Imaging Using C-arm Computed Tomography: Algorithms and Clinical Evaluation

Interventionelle Perfusionsbildgebung mittels C-Bogen-Computertomographie: Algorithmen und klinische Evaluation

Der Technischen Fakultät der
Universität Erlangen–Nürnberg

zur Erlangung des Grades

DOKTOR–INGENIEUR

vorgelegt von

Andreas Fieselmann, M.Sc.

Erlangen — 2012

Als Dissertation genehmigt von der
Technischen Fakultät der
Universität Erlangen-Nürnberg

Tag der Einreichung:	18.07.2011
Tag der Promotion:	09.09.2011
Dekan:	Prof. Dr.-Ing. habil. R. German
Berichterstatter:	Prof. Dr.-Ing. J. Hornegger
	Assoc. Prof. R. Fahrig, Ph.D.

Abstract

A stroke is a medical emergency which requires immediate diagnosis and treatment. For several years, image-based stroke diagnosis has been assisted using perfusion computed tomography (CT) and perfusion magnetic resonance imaging (MRI). A contrast agent bolus is injected and time-resolved imaging, at typically one frame per second, is used to measure the contrast agent flow. However, these two modalities are not accessible in the interventional suite where catheter-guided stroke treatment actually takes place. Thus, interventional perfusion imaging, which could lead to optimized stroke management, is currently not available.

In this thesis, a novel approach is developed that makes interventional perfusion imaging possible. It uses a C-arm angiography system capable of CT-like imaging (C-arm CT). This system can acquire projection images during a rotation around the object which are then used to reconstruct 3-D data sets. The comparably low C-arm rotation speed (typically 3–5 seconds per 200°) is the main technical challenge of this approach.

One of the major contributions of this thesis lies in the development and evaluation of a novel combined scanning and reconstruction method. It uses several interleaved scanning sequences to increase the temporal sampling of the dynamic perfusion signals. A dedicated reconstruction scheme is applied to process the data from this protocol. For the first time, *in vivo* C-arm CT perfusion studies have been carried out and the results have been compared to those from a reference perfusion CT exam. Promising correlation values ranging from 0.63 to 0.94 were obtained.

An additional contribution was made in the field of image reconstruction theory by deriving a theoretical model for image reconstruction artifacts due to time-varying attenuation values. The attenuation values in C-arm CT perfusion imaging vary due to the contrast agent flow during the long C-arm rotation time. It was shown that the magnitude of these artifacts can be reduced when using optimized reconstruction parameters.

Furthermore, investigations regarding special injection protocols were carried out and fundamental image quality measurements were made.

Through the methods developed, the measurements conducted and results obtained, this thesis made a number of significant and original contributions, both on a practical and on a theoretical level, to the novel and highly relevant research field of interventional C-arm CT perfusion imaging.

Kurzfassung

Der Schlaganfall ist ein medizinischer Notfall, der eine sofortige Diagnose und Therapie erfordert. Seit einigen Jahren werden die Perfusions-Computertomographie (CT) sowie die Perfusions-Magnetresonanztomographie (MRT) zur Unterstützung der bildbasierten Schlaganfalldiagnostik eingesetzt. Dabei wird ein Kontrastmittelbolus injiziert und eine zeitaufgelöste Aufnahme mit typischerweise einem Bild pro Sekunde durchgeführt, um den Kontrastmittelfluss zu messen. Allerdings stehen diese beiden Modalitäten nicht in Angiographieräumen zur Verfügung, in denen die kathetergestützte Schlaganfalltherapie durchgeführt wird. Daher ist interventionelle Perfusionsbildgebung, welche zu verbesserter Schlaganfallbehandlung führen kann, gegenwärtig nicht möglich.

In dieser Arbeit wird ein neuartiger Ansatz entwickelt, der interventionelle Perfusionsbildgebung ermöglicht. Dieser Ansatz verwendet ein C-Bogen-Angiographiesystem, mit dem CT-ähnliche Bildgebung durchgeführt werden kann (C-Bogen-CT). Mit diesem System werden Projektionsbilder während einer Rotation um das Objekt aufgenommen, aus denen dann 3-D-Datensätze rekonstruiert werden. Die vergleichsweise langsame Rotationsgeschwindigkeit des C-Bogens (typischerweise 3–5 Sekunden pro 200°) stellt bei diesem Ansatz die größte technische Herausforderung dar.

Ein Hauptbeitrag dieser Arbeit liegt in der Entwicklung und Evaluation einer neuartigen, kombinierten Aufnahme- und Rekonstruktionsmethode. Dabei werden mehrere, ineinander verschachtelte Aufnahmesequenzen akquiriert, um die zeitliche Abtastung der dynamischen Perfusionssignale zu erhöhen. Die Daten werden dann mit einer angepassten Rekonstruktionsmethode verarbeitet. Zum ersten Mal wurden *in vivo* C-Bogen-CT-Perfusionsstudien durchgeführt und deren Ergebnisse mit denen einer Perfusions-CT-Untersuchung verglichen. Dabei sind vielversprechende Korrelationswerte im Bereich von 0.63 bis 0.94 erzielt worden.

Ein weiterer Beitrag wurde im Bereich der Bildrekonstruktionstheorie geleistet, indem ein theoretisches Modell für Bildrekonstruktionsartefakte durch zeitlich veränderliche Schwächungswerte hergeleitet wurde. Die Schwächungswerte ändern sich in der Perfusions-C-Bogen-CT durch den Kontrastmittelfluss während der langandauernden C-Bogen-Rotation. Es wurde gezeigt, dass sich das Ausmaß dieser Artefakte mit optimierten Rekonstruktionsparametern reduzieren lässt.

Darüber hinaus wurden Fragestellungen hinsichtlich besonderer Injektionsprotokolle untersucht und grundlegende Bildqualitätsmessungen durchgeführt.

Durch die entwickelten Methoden, die durchgeführten Messungen und erzielten Ergebnisse leistet diese Arbeit, in theoretischer als auch in praktischer Hinsicht, mehrere wesentliche, neue Beiträge zu dem neuartigen und hochrelevanten Forschungsgebiet der interventionellen C-Bogen-CT-Perfusionsbildgebung.

Acknowledgment

During the last 3.5 years I have had the great opportunity to work as a Ph.D. candidate at the University of Erlangen-Nuremberg on an exciting research project in collaboration with Stanford University and Siemens Healthcare. I am grateful for the support and advice from numerous people, who have made this thesis become reality. In particular, I would like to thank

Prof. Dr.-Ing. Joachim Hornegger for giving me the opportunity to become a team member of the Pattern Recognition Lab (LME) at the University of Erlangen-Nuremberg where I was able to work on this thesis in a creative and stimulating environment. He provided a motivating atmosphere and supervised my research offering valuable feedback and advice. My work has profited substantially from the cooperation with

Assoc. Prof. Rebecca Fahrig, Ph.D., and her group at Stanford University. I am grateful for the friendly welcome offered during my stays at Stanford and her commitment when performing studies — even at inconvenient times of the day. Likewise, I also thank her for valuable feedback and advice regarding my research. I am indebted to my colleagues at Siemens Healthcare; especially to

Dipl.-Inf. Yu Deuerling-Zheng, M.Med., who has been my supervisor at Siemens since the second year of this thesis project and to Dr.-Ing. Michael Zellerhoff who was my supervisor during the first year. I am very grateful for your constant support regarding all kinds of questions, your dedication to this project, the feedback and advice, and the pleasant working atmosphere.

Furthermore, I wish to give thanks to Dr. rer. nat. Jan Boese for initiating this thesis project and enabling a perfect research environment in his group at Siemens, to Dr.-Ing. Markus Kowarschik for many valuable discussions and for feedback regarding my work, to Dr.-Ing. Frank Dennerlein for his advice in image reconstruction theory, and to Dr. rer. nat. Günter Lauritsch for sharing his knowledge on dynamic image reconstruction algorithms. I am also very grateful to those who helped with various aspects of the studies at Stanford; in particular to

Arundhuti Ganguly, Ph.D., for innumerable support while I was at Stanford and when I was in Germany, your help was indispensable. I also wish to thank Teri Moore, B.S., Marily Sarmiento, M.S., Wendy Baumgartner, RVT, and Pamela Hertz, RVT, for providing technical assistance before and during these studies.

Moreover, I want to thank my current and former colleagues at the LME; especially Dipl.-Inf. Johannes Feulner, Dr.-Ing. Christopher Rohkohl, and Dipl.-Ing. Michael Manhart for many useful discussions and Dr.-Ing. Dieter Hahn for his support regarding image registration issues. I also want to thank Dipl.-Inf. Martin Wagner from the University of Heidelberg for a lively exchange of ideas.

I gratefully acknowledge the financial support of Siemens AG and the Erlangen Graduate School in Advanced Optical Technologies (SAOT) that enabled my research.

Last but not least, I would like to thank my family and my wife for their great patience, support, and encouragement throughout all these years.

Andreas Fieselmann

Contents

Chapter 1

Introduction

1.1 Motivation: Enhancing Stroke Treatment

Nowadays, a significant amount of research is conducted to improve prevention and treatment of stroke. Often research is concerned with clinical aspects of stroke but also many research projects in engineering exist that contribute to this topic.

This thesis comes from a technical discipline and aims to find solutions to a particular technical challenge in order to enhance stroke treatment. For several years, perfusion imaging is used by physicians for stroke diagnosis and treatment planning. The term perfusion refers to the blood flow at the capillary level. Due to technical constraints perfusion imaging is, however, not available in the interventional suite yet, i.e. the room where certain kinds of stroke treatment actually take place.

The motivation of this thesis is to examine the feasibility of perfusion imaging in the interventional suite. This new application could enhance stroke treatment by providing additional perfusion information immediately before or during the treatment. The practical benefits of this application and the related technical challenges will be explained in the following two sections of this introductory chapter.

1.2 Clinical Background

1.2.1 Stroke Diagnosis and Treatment

According to the world health organization (WHO), stroke is one of the leading causes of death worldwide [1]. Estimations show that stroke and other cerebrovascular diseases have accounted for 5.6% (low-income countries), 14.2% (middle-income countries) and 9.3% (high-income countries) of deaths in 2004 [1]. The risk of stroke approximately doubles for each decade of life after the age of 55 [2]. Thus, with an increasing life expectancy, the global number of strokes is expected to further increase in the future. There are two types of stroke.

1. Ischemic strokes, which constitute about 85% of all stroke cases, and which will be the focus in the following explanations, occur if a cerebral artery is blocked and certain areas of the brain do not receive sufficient blood supply [3].

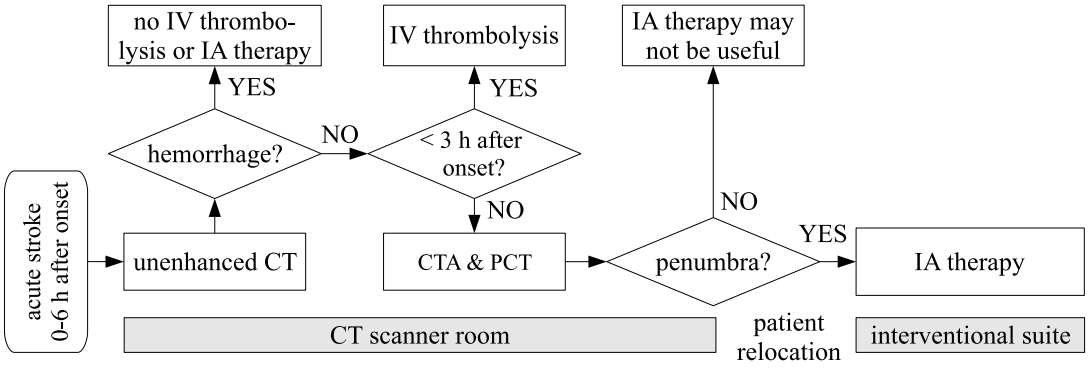

Figure 1.1: Typical stroke management protocol (adapted from [6]).

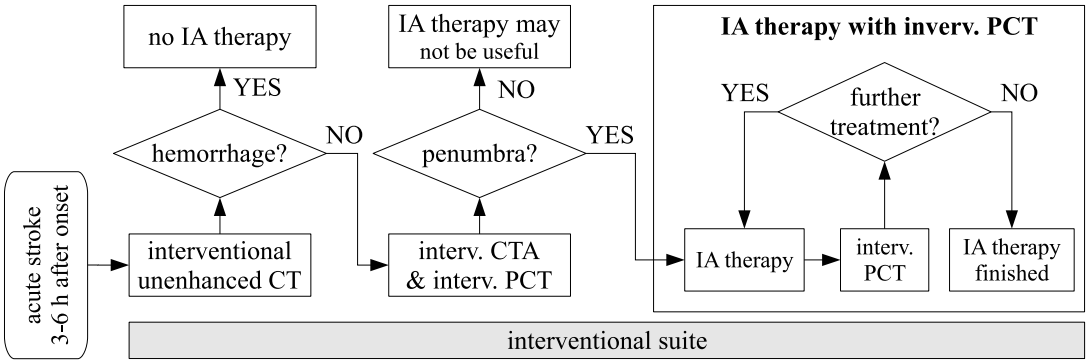

Figure 1.2: Potential stroke management protocol in the interventional suite.

2. Hemorrhagic strokes are caused by a ruptured cerebral vessel allowing blood to leak into the brain.

For ischemic stroke there are two main treatment options.

1. During intra-venous (IV) thrombolysis a pharmaceutical is injected intra-venously to dissolve the blocking of the artery [3].

2. The second therapeutic option is intra-arterial (IA) therapy which requires the patient to be in the interventional suite where a catheter can be guided to the cerebral arteries. Using this catheter, either a pharmaceutical can be administered locally near the blocking (IA thrombolysis) or the blocking can be dissolved mechanically (mechanical thrombolysis), see [3] for details.

The effectiveness of IV thrombolysis and IA therapy strongly depends on the elapsed time after the onset of stroke. According to [4], the time window for considering IA therapy is 0–6 hours after onset whereas for IV thrombolysis it is 0–3 hours after onset. Note, during every minute in which a typical ischemic stroke is untreated the average patient loses 1.9 million neurons [5]. For comparison, the average number of neurons in the human forebrain is reported to be 22 billion [5]. Thus, fast stroke treatment is mandatory.

Figure 1.1 shows a flow chart, adapted from [6], of a typical stroke management protocol for patients which present to the hospital less than 6 hours after onset of

symptoms. First, a non-contrast-agent-enhanced CT exam is performed to rule out intra-cranial hemorrhage which is a contraindication for IV thrombolysis or IA therapy. If the onset of symptoms is less than 3 hours ago IV thrombolysis can be performed. Otherwise further diagnosis with CT angiography (CTA) and perfusion CT (PCT) is necessary to determine the risk-to-benefit-ratio of IA therapy. Equivalent diagnostic exams could also be conducted using MRI.

Generally, a stroke is characterized by an infarct core which can be surrounded by a region of potentially salvageable tissue known as the penumbra. With PCT various cerebral perfusion parameters can be measured which help to decide if a penumbra exists that may actually benefit from IA therapy [3]. If the decision for IA therapy is made the patient must be relocated from the CT scanner room to the interventional suite and prepared for IA therapy.

Note, the perfusion scan in the CT scanning room is necessary but causes a delay before the start of IA therapy [7]. Furthermore, the state of perfusion may change between the CT perfusion scan and the start of IA therapy.

1.2.2 Benefits of Interventional Perfusion Imaging

Assuming perfusion imaging directly in the interventional suite would be possible, using a modality known as C-arm CT (Section 1.3.1), for example, then IA therapy could be enhanced by providing additional perfusion scans immediately before or during the intervention. The following potential advantages exist.

1. **Re-assessment of perfusion immediately before IA therapy:** As previously mentioned, the state of perfusion may change between the initial perfusion scan and the start of IA therapy. Therefore, re-assessment of perfusion in the interventional suite immediately before the start of the therapy could provide the physicians with more precise information about the current state of perfusion. If necessary, the treatment plans could be adapted.

2. **Monitoring of perfusion during IA therapy:** With interventional perfusion imaging the treatment success of IA therapy could be directly determined in the interventional suite during the procedure. This could support therapeutic decisions, e.g. to determine the treatment endpoint, and therefore make IA therapy more effective.

3. **Faster start of IA therapy:** In selected cases, when a stroke is suspected and the stroke onset is estimated to be 3–6 hours ago, the patient could be brought directly to the interventional suite. Unenhanced CT (also denoted as native CT), CTA and perfusion CT (the latter two if hemorrhage is excluded) could be acquired in the interventional environment using C-arm CT. Here, it is assumed that the image quality of unenhanced interventional CT is sufficient to exclude hemorrhage. If the patient would be assessed suitable for IA therapy then no relocation would be necessary which would make the overall workflow faster compared to the standard workflow. A flow chart of this workflow is shown in Figure 1.2. A recent study has suggested that IA thrombolysis may provide better results in reopening occluded vessels also in the 0–3 hours window

(a) monoplane system (Artis zee ceiling-mounted) (b) robotic, monoplane system (Artis zeego) (c) biplane system (Artis zee biplane)

Figure 1.3: Clinical C-arm angiography systems (Siemens AG, Healthcare Sector, Forchheim, Germany) capable of CT-like imaging (images courtesy of Siemens AG).

after onset of symptoms where normally IV thrombolysis is preferred [8]. Thus, this workflow may also apply to patients where the onset of stroke is estimated to be less than 3 hours ago.

1.3 Interventional Imaging with C-arm CT

1.3.1 Basics

The main application for an X-ray C-arm angiography system is to provide real-time, time-resolved (typically 1–30 frames per second) 2-D images of the organ of interest during interventional procedures. Figure 1.3 shows different state-of-the-art clinical C-arm angiography systems equipped with flat-panel detectors. With the C-arm at a fixed position, X-ray radiation is emitted from the X-ray source and recorded using the detector. The organ of interest is located between the source and the detector and attenuates the X-ray radiation.

The 2-D images may be used to navigate a catheter inside an artery, for example. Another well-established application is digital subtraction angiography (DSA) where images acquired after the injection of a contrast agent are processed by subtraction of a mask image of the same region without contrast agent. This technique is used to evaluate the blood flow in vessels or pathological structures like aneurysms [9].

This 2-D imaging method provides high temporal resolution and high spatial resolution (typically 0.3–0.6 mm pixel side length). However, since the images are projections of the 3-D organ of interest onto a 2-D plane certain disadvantages arise.

1. 3-D organs with a complex geometry are difficult to interpret using these 2-D projections only.

2. It is generally not possible to recognize low contrast differences between certain structures of the 3-D organ. As an example, the bleeding visible in the tomographic image shown in Figure 1.4(b) would not be obvious in a projection image as shown in Figure 1.4(a).

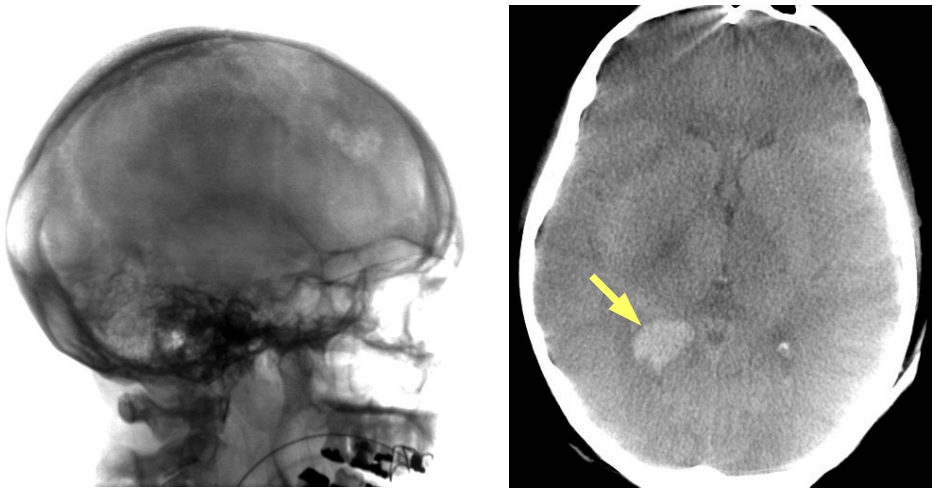

(a) X-ray projection image (b) reconstructed C-arm CT image

Figure 1.4: (a) X-ray projection image of a human head acquired with a C-arm angiography system and (b) transaxial C-arm CT reconstruction showing a bleeding in the right hemisphere (images courtesy of (a) Dr. T. Struffert, Department of Neuroradiology, University of Erlangen-Nuremberg, Germany and (b) Siemens AG).

To overcome these limitations of projections-based 2-D imaging, it is possible for several years to acquire tomographic, CT-like images in the interventional suite by using C-arm CT, also known as flat-detector CT (FD-CT) or 3D rotational angiography (3DRA) [10, 11, 12, 13]. While the C-arm rotates around the patient (typically through 200°) hundred to several hundreds of 2-D projection images are acquired. Using a cone-beam image reconstruction algorithm, a 3-D volume can be reconstructed from this data set [14, 15].

With C-arm CT, 3-D images of complex-shaped objects like the heart, for example, can be obtained for pre-procedural treatment planning or intra-cranial bleedings can be recognized. Depending on the object size, a state-of-the-art C-arm CT system can resolve objects with a contrast difference of 5–10 Hounsfield units (HU) [13]. Thus, it can significantly enhance the functionality of C-arm angiography systems during interventional procedures.

The principle of C-arm CT is closely related to that of conventional multi-slice CT (MSCT), but there are also some differences. As an example, the time needed to acquire one full set of projection data over an angular range of 200° typically takes 3–5 s with C-arm CT while it takes only 0.3–0.5 s per 360° with MSCT. Due to mechanical constraints and for the sake of patient safety, the C-arm rotation speed is restricted to a certain maximal value. Furthermore, current C-arm CT systems are not capable of performing uni-directional, continuous C-arm rotations as in MSCT. Instead, the C-arm can only perform alternating forward and backward rotations in order to sequentially acquire several reconstructed volumes.

Usually analytical image reconstruction algorithms such as Feldkamp-type algorithms [16] are used to reconstruct the large C-arm CT volume data sets (typically ranging from 256^3 to 512^3 voxels) [13]. These analytical algorithms assume a stationary object of interest during the acquisition of the projection data. For the human

heart, for example, this assumption is not valid and sophisticated C-arm CT image reconstruction algorithms have been developed to compensate for the cardiac motion [17, 18, 19].

Recently, quantitative imaging of cerebral blood volume with C-arm CT has been introduced [20, 21]. Using a specialized injection and scanning protocol, two reconstructed 3-D volumes are acquired before and after a contrast agent bolus injection, respectively. Cerebral blood volume describes a static parameter of cerebral perfusion. There are also dynamic perfusion parameters, such as cerebral blood flow and mean transit time (Chapter 2). Currently, these parameters cannot be measured using C-arm CT. The next section will provide a description of the challenges to measure (dynamic) perfusion parameters with C-arm CT.

1.3.2 Challenges of C-arm CT Perfusion Imaging

In perfusion CT imaging the flow of an injected contrast agent bolus is imaged at short intervals, typically one reconstructed image per second, and the time-resolved data is analyzed on a voxel-by-voxel basis to compute various perfusion parameters, see Chapter 2 for details.

Thus, perfusion-CT-like imaging could be implemented with C-arm CT by acquiring reconstructed images using alternating forward and backward C-arm rotations after a contrast agent bolus injection. However, there are two major challenges with respect to this approach which will be discussed next. Both of these challenges are related to the comparably long acquisition time for a complete set of projections which is about one order of magnitude greater in C-arm CT compared to MSCT.

1. Due to the longer sample period in C-arm CT — which is typically 3–5 seconds rotation time plus 1 second wait time between two rotations in alternating direction — temporal undersampling of the dynamic contrast agent flow can occur which in the following image analysis can lead to incorrect perfusion values.

2. In PCT the acquisition time for one set of projection data is sufficiently short such that the (intentional) change of attenuation values due to the contrast agent flow in the organ of interest can be assumed to be constant during this interval. However, in perfusion C-arm CT this assumption is not appropriate due to the longer acquisition times and image reconstruction artifacts can arise. These artifacts can also cause incorrect perfusion values.

1.4 Scope and Original Contributions of this Thesis

This thesis covers several topics from the field of medical image processing that are practically relevant for C-arm CT perfusion imaging. Generally, the two main steps in C-arm CT perfusion imaging — from an image processing point of view — are image reconstruction of a dynamic object due to contrast agent flow and image analysis of the reconstructed data.

Both of these steps were addressed in this thesis and, additionally, algorithms for the analysis of contrast agent bolus injection protocols were developed and fundamental image quality measurements (measurement of iodine concentration) were carried out. Furthermore, a software program was implemented as part of the work on this thesis to investigate a complete C-arm CT perfusion imaging workflow under realistic conditions.

The original contributions of this thesis are summarized below along with the corresponding publications.

1. **Novel Scanning Protocol and Reconstruction Approach:** In order to compensate the low temporal sampling of the reconstructed C-arm CT data (Section 1.3.2) an interleaved scanning (IS) protocol was developed. In combination with a specialized reconstruction approach, denoted as partial reconstruction interpolation (PRI), also the artifacts due to data inconsistencies can be reduced. This novel combined approach (IS-PRI) was investigated using numerical simulations and *in vivo* C-arm CT data from a pre-clinical study. Methods and results were also presented in journal articles and at conferences which were focused on technical applications, see [22, 23], and clinical applications, see [24, 25], respectively. Furthermore, results from physical phantom measurements were published in [26] but are not presented in this thesis.

2. **Novel Model for Reconstruction Artifacts:** Image reconstruction artifacts arise if the X-ray attenuation values vary during the acquisition of the projection data. This topic is of particular concern in perfusion C-arm CT imaging due to the intentional contrast agent flow and the low scanning speed, cf. Section 1.3.2. A novel mathematical model based on the concept of derivative-weighted point spread functions was developed in order to better understand this kind of reconstruction artifact. Using this model, the impact of this reconstruction artifact and suitable reduction strategies can be investigated. Methods and results were also presented in a journal article [27] and at a conference [28].

3. **Review of Perfusion Image Analysis:** Diagnostic CT and MR brain perfusion imaging is available for several years already and well-established image analysis methods exist. A review of both the theoretical model and the practical implementation of these methods was carried out. A particular novel aspect of this review was to outline the simplifications of the model that is necessary in order to apply it to real data. This review has been published as a journal article [29].

4. **Novel Approach for Contrast Agent Bolus Measurement:** Since perfusion C-arm CT imaging is conducted in the interventional suite, alternative IA contrast agent bolus injection strategies compared to a conventional IV injection could be applied. In order to investigate these alternative injection protocols, a novel approach to segment the carotid arteries and to measure the contrast agent bolus distribution has been developed. The segmentation technique is based on a suitable weighting of a temporal maximum intensity projection of a DSA sequence. This approach has also been presented at a conference [30].

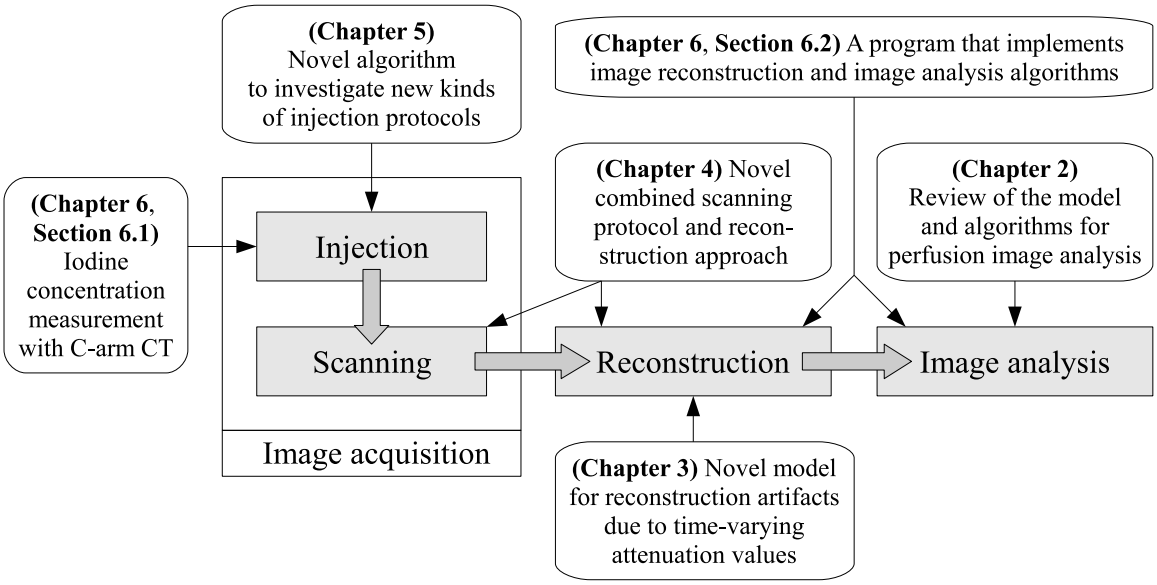

Figure 1.5: Graphical overview of the chapters of this thesis and how they are related to the workflow of C-arm CT perfusion imaging.

5. **Measurement of C-arm CT Image Quality:** An underlying assumption in CT perfusion imaging is that the measured X-ray attenuation values are proportional to the local contrast agent concentrations. Measurements with a physical phantom were carried out to verify this assumption for a clinical C-arm CT system. These measurements were also presented at a conference [31]

In summary, the results of this thesis were published in four journal articles [23, 25, 27, 29] and were presented at five conferences [22, 24, 28, 30, 31].

1.5 Organization of this Thesis

In this section, the organization of this thesis will be explained in order to provide a better orientation for the reader. A graphical overview of the chapters of this thesis and how they are related to the C-arm CT perfusion imaging workflow is provided in Figure 1.5. The depicted perfusion imaging workflow consists of the image acquisition (injection and scanning), image reconstruction and image analysis steps. Note, the first chapter (Introduction) and the last chapter (Summary and Conclusion) are not displayed in this figure. Furthermore, a short description of each chapter will be given next.

Chapter 1 — Introduction

This chapter introduces the reader to the necessary clinical and technical background of this thesis. In particular, the benefits of interventional perfusion imaging and the related technical challenges are discussed. An overview of the scope and the original contributions as well as the organization of this thesis is presented.

Chapter 2 — Review of Image Analysis for Brain Perfusion Measurement

In this chapter, a review of existing work on image analysis techniques for CT and MR brain perfusion data is provided. Since CT and MR brain perfusion is available for several years, well-established image analysis techniques exist. These techniques are used to process the C-arm CT data obtained using the novel reconstruction methods described in Chapter 4. They are also implemented in the software program that is described in Section 6.2.

Chapter 3 — A Model for Filtered Backprojection Reconstruction Artifacts due to Time-Varying Attenuation Values

The intention of this theoretically oriented chapter is to provide a detailed understanding of filtered backprojection reconstruction artifacts when the attenuation values vary during the data acquisition. A short summary of FBP image reconstruction is given and a novel spatio-temporal model is derived. This model is used to analyze artifact reduction techniques. Measurements using C-arm CT were compared to predictions of the artifact model.

Chapter 4 — C-arm CT Perfusion Imaging Using Interleaved Scanning and Partial Reconstruction Interpolation

This chapter presents the main practical contribution of this thesis which is a novel approach for C-arm CT perfusion imaging. This approach is a combined scanning protocol and reconstruction technique that increases temporal sampling of the reconstructed data. It also provides a mean to reduce the reconstruction artifacts that were described in Chapter 3. The approach is described in detail and is evaluated using numerical simulations and *in vivo* data.

Chapter 5 — Evaluation of Contrast Agent Bolus Injection at the Aortic Arch: Automatic Measurement of Bolus Distribution

In this chapter, methods and results of a novel approach to measure the contrast agent bolus distribution in the carotid arteries using 2-D DSA are presented. In the preclinical studies presented in Chapter 4 the contrast bolus was injected at the aortic arch. To verify that equal amounts of contrast agent flow into both carotid arteries, this automated segmentation and image analysis method was actually developed. The method is evaluated using real data from a clinical C-arm angiography system.

Chapter 6 — Practical Aspects Regarding C-arm CT Perfusion Imaging

This chapter covers two aspects that have been identified to be practically relevant when CT-like perfusion imaging is to be implemented using C-arm CT.

1. The first part of this chapter addresses fundamental C-arm CT image quality measurements. In order to investigate the feasibility of C-arm CT for perfusion imaging, the linearity of contrast agent concentration and measured X-ray attenuation was verified. The measurements were performed using the same C-arm CT system as for acquiring the *in vivo* data in Chapter 4.

2. As part of this thesis, a software program was developed to implement a complete perfusion imaging workflow with C-arm CT. In the second part of this chapter, this program is described and an overview of the corresponding workflow is given. The program implements the algorithms from Chapters 2 and 4.

Chapter 7 — Summary and Outlook

This chapter summarized the work presented in this thesis, provides general conclusions, and gives an outlook for future work.

Chapter 2

Review of Image Analysis for Brain Perfusion Measurement

Overview:
In this chapter, a review of the theory and the practical implementation of image analysis algorithms for CT and MR brain perfusion measurement is provided. It focuses on deconvolution-based image analysis algorithms which are the most commonly applied algorithms for this purpose. In particular, the deconvolution methods that utilize the regularized singular value decomposition are described. First, a detailed explanation of the underlying physiological model will be provided (Section 2.2). Then the practical implementations are described (Section 2.3) and relevant pre-processing steps are explained (Section 2.4).

The algorithms presented in this chapter will be used to analyze the C-arm CT perfusion data reconstructed with the methods described in Chapter 4 and they are implemented in the software program described in Chapter 6.2.

This chapter is based on "Deconvolution-based CT and MR brain perfusion measurement: theoretical model revisited and practical implementation details", by A. Fieselmann, M. Kowarschik, A. Ganguly, J. Hornegger, and R. Fahrig. *International Journal of Biomedical Imaging*, vol. 2011, article ID 467563, 20 pages [29].

2.1 Introduction

CT and MR brain perfusion imaging is commonly used for image-based stroke diagnosis. It is conducted by injecting a contrast agent bolus into a vein followed by repeated scanning of the brain. Typically, one reconstructed image per second is obtained over an interval of about 40–50 s [3]. A different application for perfusion imaging is to evaluate the blood flow in tumors, for example, which also uses a contrast agent bolus injection and repeated scanning [32].

A time-concentration curve (TCC) can be extracted at each voxel position of this time-resolved data set. This TCC describes the change of contrast agent concentration over time after the contrast agent bolus injection. Various perfusion parameters can be computed from each TCC. Thus, a parameter map can be obtained that provides information about the local state of tissue perfusion at different voxel positions.

As an example, Figure 2.1 shows common parameter maps based on a brain perfusion CT exam (Somatom Definition AS+, Siemens AG, Healthcare Sector, Forchheim, Germany) of a 69-year-old male stroke patient. The patient presented to the hospital with an acute high grade hemiparesis on the right side. A CT angiography scan indicated an occlusion of the left middle cerebral artery. The time-to-peak (TTP) image shows a large lesion that illustrates the maximum involved tissue. In addition, the cerebral blood flow (CBF), cerebral blood volume (CBV), and mean transit time (MTT) images exhibit perfusion deficits in a smaller brain territory.

These perfusion parameters will be explained in Section 2.2, where a detailed derivation of the underlying model of the tissue perfusion will be presented.

2.2 Theoretical Model

In this section, the theoretical physiological model of tissue perfusion for intravascular tracer systems will be introduced and the derivation of a deconvolution-based mathematical approach for the estimation of diagnostically important perfusion parameters will be presented.

2.2.1 Model of the Microcirculation at the Tissue Level

For computing the tissue perfusion, a physiological model of the blood supply to the tissue is assumed. Figure 2.2 shows this model that consists of a volume of interest $\mathcal{V}_{\text{voi}}$ covering the organ-specific parenchyma, the interstitial space, as well as the capillary bed. The volumes of the parenchyma and the interstitial space are denoted by $\mathcal{V}^*_{\text{voi}}$, while the volume of the capillary bed is referred to as $\mathcal{V}_{\text{cap}}$. The entire volume of interest $\mathcal{V}_{\text{voi}} = \mathcal{V}^*_{\text{voi}} \cup \mathcal{V}_{\text{cap}}$ shall be supplied with blood by a single arterial inlet and correspondingly drained by a single venous outlet. In general, it may have a different shape than the cuboid shown in Figure 2.2. A blood cell can take various paths through the capillary bed. The transit time t it needs to pass through the capillary bed depends on the chosen path. A stationary probability density function $h_{\text{cap}}(t)$ of transit times is assumed.

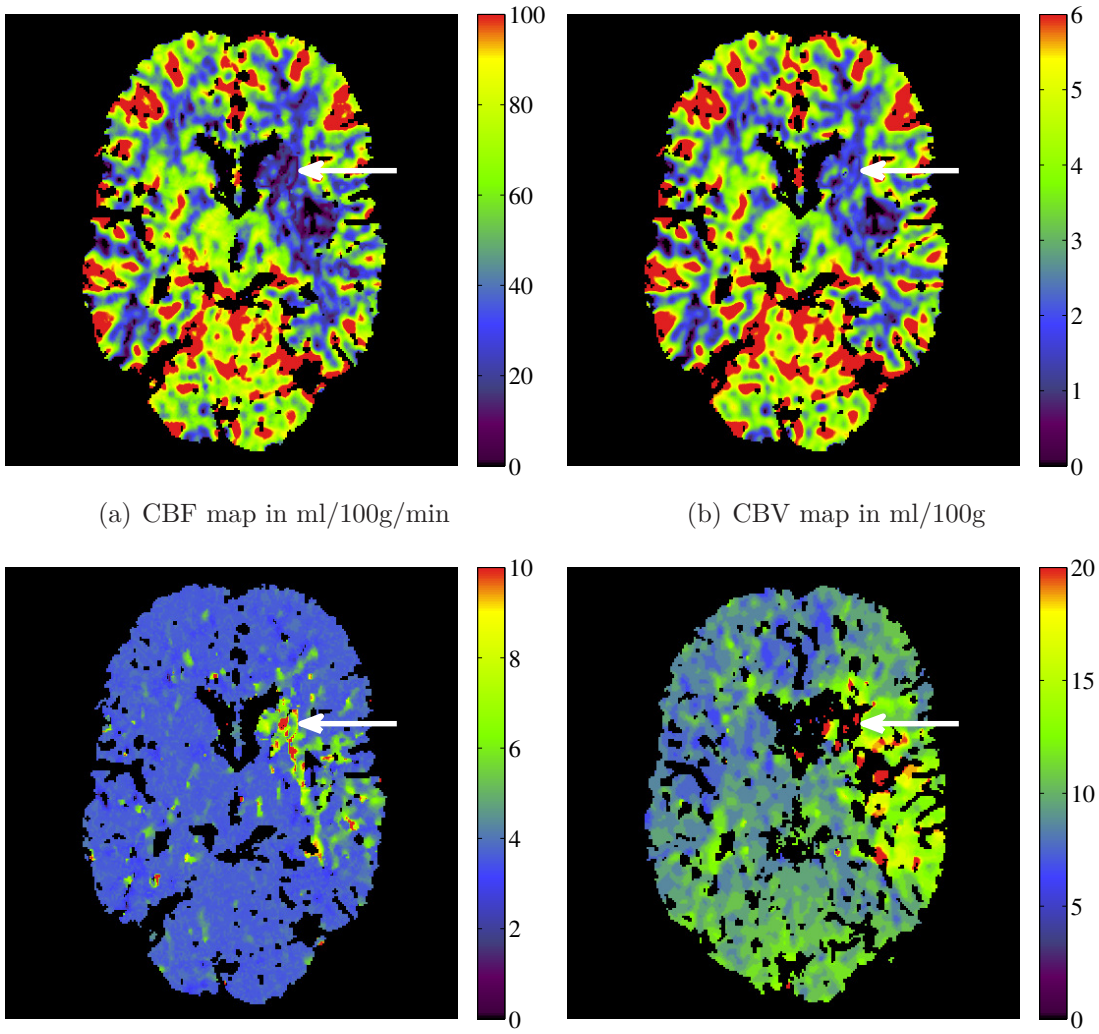

(a) CBF map in ml/100g/min

(b) CBV map in ml/100g

(c) MTT map in s

(d) TTP map in s

Figure 2.1: CT perfusion parameter maps of cerebral blood flow (CBF), cerebral blood volume (CBV), mean transit time (MTT), and time-to-peak (TTP). The ischemic stroke lesion is marked with arrows (images courtesy of Dr. T. Struffert, Department of Neuroradiology, University of Erlangen-Nuremberg, Germany).

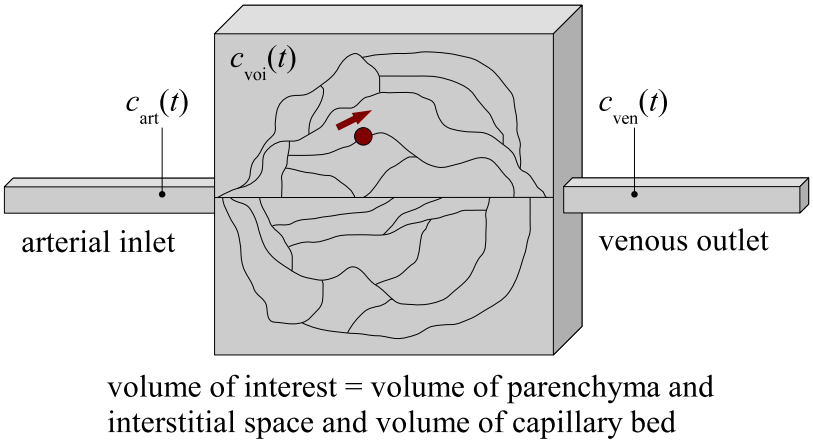

Figure 2.2: Physiological model of the tissue perfusion. A blood cell can take several paths through the capillary bed. The variables are defined in Table 2.1.

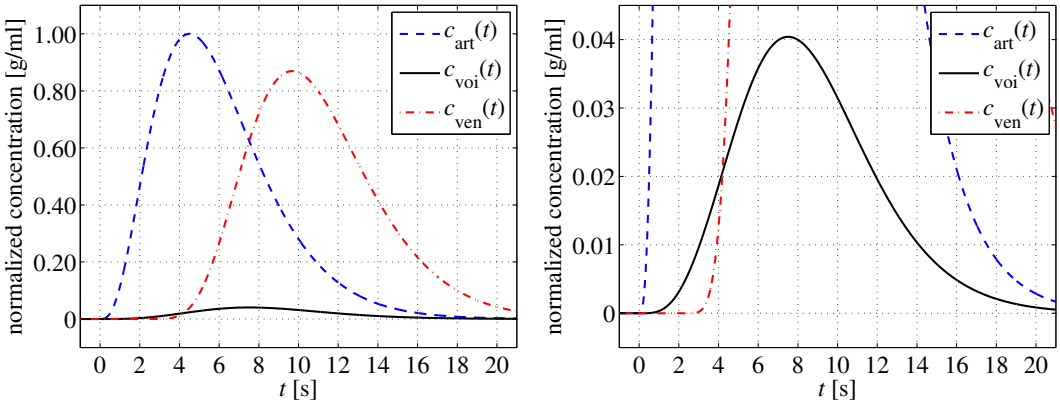

(a) typical TCCs (b) zoomed view of (a)

Figure 2.3: Examples of the time-concentration curves (TCC) $c_{\text{art}}(t)$, $c_{\text{voi}}(t)$, and $c_{\text{ven}}(t)$ given in arbitrary units (a.u.). The right figure (b) represents a zoomed view of the left figure (a) with a rescaled ordinate.

Once a contrast agent bolus has been injected, it enters the volume $\mathcal{V}_{\text{voi}}$ under consideration via the arterial inlet and is then diluted into the capillary bed. The local contrast agent concentrations $c_{\text{art}}(t)$ and $c_{\text{ven}}(t)$ are measured directly adjacent to the capillary bed on the arterial and venous sides, respectively. Furthermore, the average contrast agent concentration $c_{\text{voi}}(t)$ within the volume of interest can also be measured. In perfusion CT an iodinated contrast agent is used, whereas in perfusion MRI the measured signal difference is created by a paramagnetic contrast agent based on gadolinium (Gd). The contrast agent concentration is defined as mass of iodinated contrast agent per volume (unit: g/ml) or amount of Gd-based contrast agent per volume (unit: mol/ml), respectively [33]. For the following analysis, the contrast agent concentration is assumed to be measured as mass per volume, which can easily be related to amount per volume.

Figure 2.3 illustrates TCCs $c_{\text{art}}(t)$, $c_{\text{voi}}(t)$, and $c_{\text{ven}}(t)$ that may be measured in brain tissue, for example. For the sake of simplicity, the maximum contrast agent

concentration has been normalized to one. Note, the (average) enhancement within the volume of interest is commonly more than an order of magnitude below the enhancements of the feeding artery and the draining vein.

An additional, important assumption is that the contrast agent remains in the intravascular space. For our case of cerebral perfusion, it should therefore not cross the blood-brain barrier (BBB). As a consequence, this means that all contrast agent entering from the arterial inlet will eventually leave the volume of interest at the venous outlet. A breakdown of the BBB may occur in tumor patients, in stroke patients, and in patients that suffer from inflammations or infections, for example. In these cases, the methods presented in this chapter may lead to inaccurate perfusion estimates and particularly to an overestimation of the blood volume [34, 35]. Note, there exist other modeling approaches which do not assume that the contrast agent remains in the intravascular space. These models can be used for measuring tumor perfusion, for example [32, 33, 36].

Finally, it is supposed that the contrast agent mixes perfectly with the blood and that the physical properties of the blood (its flow behavior, in particular) are not influenced by the contrast agent.

In fact, only knowledge of the functions $c_{\mathrm{art}}(t)$ and $c_{\mathrm{voi}}(t)$ is needed to compute the blood flow within the volume under consideration. In practice, the function $c_{\mathrm{art}}(t)$ — also known as the arterial input function (AIF) — is not measured directly at the respective volume of interest, but in a larger feeding artery in order to achieve a reasonable signal-to-noise ratio (SNR) (see Section 2.3.1).

As a first diagnostically relevant perfusion parameter, the mean transit time (MTT) of the volume under consideration is defined as the first moment of the probability density function $h_{\mathrm{cap}}(t)$ of the transit times; i.e.,

$$\mathrm{MTT} = \int_0^\infty \tau \, h_{\mathrm{cap}}(\tau) \, \mathrm{d}\tau \ , \tag{2.1}$$

considering that $h_{\mathrm{cap}}(t) = 0 \ \forall \, t < 0$. Furthermore, the residue (or residual) function $r(t)$ — cf. [37] — represents an intermediate quantity of interest and is defined as

$$r(t) = \begin{cases} 1 - \int_0^t h_{\mathrm{cap}}(\tau) \, \mathrm{d}\tau & \text{for } t \geq 0 \ , \\ 0 & \text{for } t < 0 \ . \end{cases} \tag{2.2}$$

The (dimension-less) residue function thus quantifies the relative amount of contrast agent that is still inside the volume $\mathcal{V}_{\mathrm{voi}}$ of interest at time t after an (idealized) delta-shaped contrast agent bolus has entered the volume at the arterial inlet at time $t = 0$; i.e., $c_{\mathrm{art}}(t) = \delta(t)$. Due to the various transit times within the capillary bed, the contrast agent will not leave the volume instantaneously, but gradually over time. In particular, this means that the residue function decreases continuously from $r(0) = 1$ to 0. Figure 2.4 shows typical examples of a probability density function $h_{\mathrm{cap}}(t)$ of transit times as well as the corresponding residue function $r(t)$. In this example, the PDF $h_{\mathrm{cap}}(t)$ is modeled by a gamma PDF [38].

Variable	Unit	Description
$\mathcal{V}_{\text{voi}}$	ml	total volume under consideration
$\mathcal{V}_{\text{cap}}$	ml	volume of the capillary bed within the volume $\mathcal{V}_{\text{voi}}$
$\mathcal{V}^*_{\text{voi}}$	ml	volume $\mathcal{V}_{\text{voi}}$ without the volume of the capillary bed, $\mathcal{V}^*_{\text{voi}} = \mathcal{V}_{\text{voi}} \setminus \mathcal{V}_{\text{cap}}$
ρ_{voi}	g/ml	mean density of the volume $\mathcal{V}_{\text{voi}}$
ρ^*_{voi}	g/ml	mean density of the volume $\mathcal{V}^*_{\text{voi}}$
$m_{\text{c,voi}}(t)$	g	total mass of contrast agent in volume $\mathcal{V}_{\text{voi}}$
$m_{\text{c,voi,in}}(t)$	g	in-flown accumulated mass of contrast agent in $\mathcal{V}_{\text{voi}}$ at time t
$m_{\text{c,voi,out}}(t)$	g	out-flown accumulated mass of contrast agent from $\mathcal{V}_{\text{voi}}$ at time t
$c_{\text{art}}(t)$	g/ml	local contrast agent concentration at the arterial inlet, $c_{\text{art}}(t) = \frac{\mathrm{d}m}{\mathrm{d}\lvert\mathcal{V}\rvert}\Big\rvert_t$, measured at the arterial inlet
$c_{\text{ven}}(t)$	g/ml	local contrast agent concentration at the venous outlet, $c_{\text{ven}}(t) = \frac{\mathrm{d}m}{\mathrm{d}\lvert\mathcal{V}\rvert}\Big\rvert_t$, measured at the venous outlet
$c_{\text{voi}}(t)$	g/ml	average contrast agent concentration in the total volume $\mathcal{V}_{\text{voi}}$, $c_{\text{voi}}(t) = m_{\text{c,voi}}(t) \,/\, \lvert\mathcal{V}_{\text{voi}}\rvert$
$c_{\text{cap}}(t)$	g/ml	average contrast agent concentration in the capillary bed, $c_{\text{cap}}(t) = m_{\text{c,voi}}(t) \,/\, \lvert\mathcal{V}_{\text{cap}}\rvert$
$c^*_{\text{voi}}(t)$	g/ml	average contrast agent concentration corresponding to $\mathcal{V}^*_{\text{voi}}$, $c^*_{\text{voi}}(t) = m_{\text{c,voi}}(t) \,/\, \lvert\mathcal{V}^*_{\text{voi}}\rvert$
F	ml/s	volume flow at the arterial inlet and at the venous outlet
$h_{\text{cap}}(t)$	1/s	probability density function of the transit times

Table 2.1: Summary of parameters used to derive the indicator-dilution theory and to define clinically relevant tissue perfusion quantities.

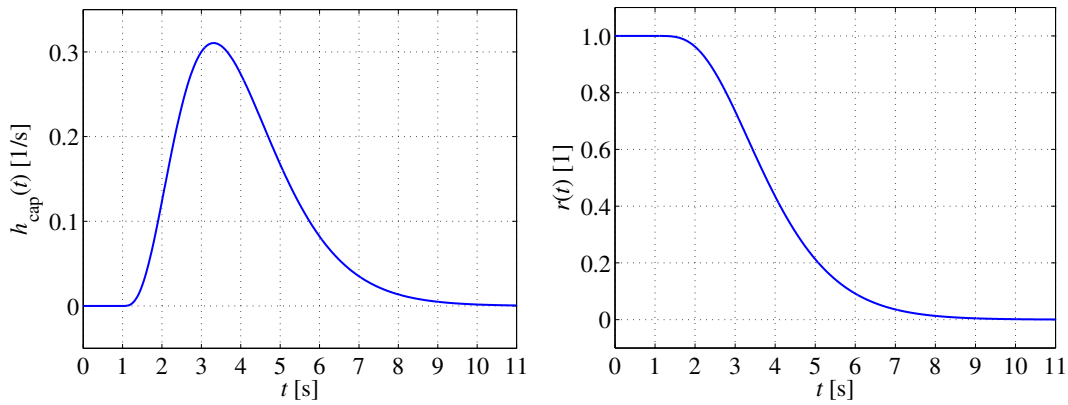

(a) PDF $h_{\text{cap}}(t)$ of transit times

(b) residue function $r(t)$

Figure 2.4: Examples of the probability density function (PDF) $h_{\text{cap}}(t)$ of transit times (the mean transit time is 4 s) and the corresponding residue function $r(t)$.

2.2.2 Derivation of the Indicator-Dilution Theory

Using the parameters defined in Table 2.1, the accumulated masses of contrast agent that have entered and left the volume of interest during the time interval $[0, t]$, denoted as $m_{\mathrm{c,voi,in}}(t)$ and $m_{\mathrm{c,voi,out}}(t)$, respectively, can be expressed as

$$m_{\mathrm{c,voi,in}}(t) = F \int_0^t c_{\mathrm{art}}(\tau)\,\mathrm{d}\tau\ , \tag{2.3}$$

$$m_{\mathrm{c,voi,out}}(t) = F \int_0^t c_{\mathrm{ven}}(\tau)\,\mathrm{d}\tau\ . \tag{2.4}$$

The volume flow F (unit: ml/s) is assumed to be constant over time. The contrast agent concentrations $c_{\mathrm{art}}(t)$ and $c_{\mathrm{ven}}(t)$ at the arterial inlet and the venous outlet, respectively, are time-dependent functions which are assumed to be 0 for $t < 0$. These functions primarily depend on the parameters of the contrast agent injection and the patient's cardiac cycle.

The mass $m_{\mathrm{c,voi}}(t)$ of a contrast agent within the volume of interest at time t can be computed using the principle of conservation of mass as

$$m_{\mathrm{c,voi}}(t) = m_{\mathrm{c,voi,in}}(t) - m_{\mathrm{c,voi,out}}(t) = F \int_0^t \left(c_{\mathrm{art}}(\tau) - c_{\mathrm{ven}}(\tau)\right)\,\mathrm{d}\tau\ . \tag{2.5}$$

The contrast agent concentration $c_{\mathrm{ven}}(t)$ at the venous outlet can be computed from the contrast agent concentration $c_{\mathrm{art}}(t)$ at the arterial inlet by convolving it with the probability density function $h_{\mathrm{cap}}(t)$. One therefore obtains

$$c_{\mathrm{ven}}(t) = \int_{-\infty}^{+\infty} c_{\mathrm{art}}(\xi)\, h_{\mathrm{cap}}(t-\xi)\,\mathrm{d}\xi\ . \tag{2.6}$$

Note, throughout this chapter, all integrals with infinite integration endpoints shall be interpreted as the limit of the integral when the respective endpoint approaches $\pm\infty$. Using Equation (2.6), Equation (2.5) can be rewritten, by applying the Dirac delta function $\delta(t)$, as

$$m_{\mathrm{c,voi}}(t) = F \int_0^t \left(\int_{-\infty}^{+\infty} c_{\mathrm{art}}(\xi)\,\delta(\tau-\xi)\,\mathrm{d}\xi - \int_{-\infty}^{+\infty} c_{\mathrm{art}}(\xi)\, h_{\mathrm{cap}}(\tau-\xi)\,\mathrm{d}\xi \right) \mathrm{d}\tau\ . \tag{2.7}$$

Changing the order of integration and re-arranging this equation leads to

$$m_{\mathrm{c,voi}}(t) = F \int_{-\infty}^{+\infty} c_{\mathrm{art}}(\xi) \left(\int_0^t \left(\delta(\tau-\xi) - h_{\mathrm{cap}}(\tau-\xi)\right) \mathrm{d}\tau \right) \mathrm{d}\xi\ . \tag{2.8}$$

By applying the substitution $\tau' = \tau - \xi$, one obtains

$$\int_0^t \left(\delta(\tau-\xi) - h_{\mathrm{cap}}(\tau-\xi)\right) \mathrm{d}\tau = \int_{-\xi}^{t-\xi} \left(\delta(\tau') - h_{\mathrm{cap}}(\tau')\right) \mathrm{d}\tau' = r(t-\xi)\ . \tag{2.9}$$

For the last step it is useful to recall that, for $t \geq 0$, it holds

$$r(t) = 1 - \int_0^t h_{\mathrm{cap}}(\tau)\,\mathrm{d}\tau = \int_0^t \left(\delta(\tau) - h_{\mathrm{cap}}(\tau)\right) \mathrm{d}\tau\ , \tag{2.10}$$

and that $h_{\mathrm{cap}}(t) = 0$ for $t < 0$. Equation (2.8) thus eventually reads

$$m_{\mathrm{c,voi}}(t) = F \int_{-\infty}^{+\infty} c_{\mathrm{art}}(\xi)\, r(t-\xi)\, \mathrm{d}\xi \ . \tag{2.11}$$

The cerebral blood flow (CBF) is introduced as the blood volume flow normalized by the mass of the volume $\mathcal{V}_{\mathrm{voi}}$,

$$\mathrm{CBF} = \frac{F}{|\mathcal{V}_{\mathrm{voi}}| \cdot \rho_{\mathrm{voi}}} \ . \tag{2.12}$$

Here, $|\mathcal{V}_{\mathrm{voi}}|$ denotes the absolute value of the volume $\mathcal{V}_{\mathrm{voi}}$. The normal value for CBF in humans is between 50 and 60 ml/100g/min for grey matter [39]. Inserting this definition into Equation (2.11) yields

$$\frac{m_{\mathrm{c,voi}}(t)}{|\mathcal{V}_{\mathrm{voi}}|} = \mathrm{CBF} \cdot \rho_{\mathrm{voi}} \cdot \int_{-\infty}^{+\infty} c_{\mathrm{art}}(\xi)\, r(t-\xi)\, \mathrm{d}\xi \ . \tag{2.13}$$

According to Table 2.1, the contrast agent concentration $c_{\mathrm{voi}}(t)$ within the volume $\mathcal{V}_{\mathrm{voi}}$ of interest is defined as

$$c_{\mathrm{voi}}(t) = \frac{m_{\mathrm{c,voi}}(t)}{|\mathcal{V}_{\mathrm{voi}}|} \ , \tag{2.14}$$

which finally leads to the following formulation of the indicator-dilution theory,

$$\begin{aligned} c_{\mathrm{voi}}(t) &= \mathrm{CBF} \cdot \rho_{\mathrm{voi}} \cdot \int_{-\infty}^{+\infty} c_{\mathrm{art}}(\xi)\, r(t-\xi)\, \mathrm{d}\xi \\ &= \mathrm{CBF} \cdot \rho_{\mathrm{voi}} \cdot (c_{\mathrm{art}} \ast r)(t) \ , \end{aligned} \tag{2.15}$$

where $\ast$ denotes the convolution operator as usual, see also [34, 40]. An alternative derivation of the same mathematical result is presented in [33]. A historical overview of the development of the indicator-dilution theory with numerous references to mathematical aspects can be found in [41]. Note, the solution of Equation (2.15) with respect to CBF and other clinically important perfusion parameters will be discussed in Section 2.2.3.

From a physiological point of view, it would be more meaningful to normalize CBF by the mass of the volume $\mathcal{V}^*_{\mathrm{voi}}$. This volume $\mathcal{V}^*_{\mathrm{voi}}$ contains the mass of the parenchyma (and the interstitium) only. In that case, CBF would be a local measure for the blood volume flow per mass of parenchyma (and interstitium) that actually requires blood supply for oxygen and nutrient delivery. In Equation (2.12), however, the volume $\mathcal{V}_{\mathrm{voi}}$ also contains the mass of the blood-filled capillary bed itself. Another aspect to consider is that the mean density ρ_{voi} of the volume, which influences the CBF value, actually depends on the (varying) mass of the contrast agent in the capillary bed. The alternative definition of CBF,

$$\mathrm{CBF}^* = \frac{F}{|\mathcal{V}^*_{\mathrm{voi}}| \cdot \rho^*_{\mathrm{voi}}} \ , \tag{2.16}$$

would then lead to a corresponding alternative formulation of the indicator-dilution theory,

$$c^*_{\mathrm{voi}}(t) = \mathrm{CBF}^* \cdot \rho^*_{\mathrm{voi}} \cdot (c_{\mathrm{art}} \ast r)(t) \ . \tag{2.17}$$

From a practical perspective, however, it is more convenient to use the definition of CBF given by Equation (2.12), see Section 2.3.1.

The derivation of the indicator-dilution theory in this section was focused on brain perfusion imaging. This theoretical model can be used in stroke patients if the BBB is intact — cf. Section 2.2.1 — but it is not suited for semi-permeable tumors, for example. With slight adaptations, this theoretical model can also be applied in other applications of perfusion imaging such as pulmonary perfusion imaging. See [42] for detailed discussions. A discussion of models in hepatic and renal perfusion imaging is given in [43] and [44], respectively.

In the context of perfusion measurement, the term recirculation refers to the physiological phenomenon that, due to the patient's cardiac activity, the contrast agent passes through the volume under consideration multiple times. It can easily be shown, however, that there is no need to correct for recirculation when deconvolution methods are applied to determine perfusion parameters [45].

2.2.3 Computation of Perfusion Parameters Using Deconvolution

In Equation (2.15), the variables $c_{\text{art}}(t)$ and $c_{\text{voi}}(t)$ can be measured and have known values whereas the values of CBF, $r(t)$, and ρ_{voi} are unknown. In order to compute CBF as well as other diagnostically relevant tissue perfusion parameters, first an intermediate quantity of interest is introduced, the flow-scaled residue function $k(t)$,

$$k(t) = \text{CBF} \cdot \rho_{\text{voi}} \cdot r(t) \ , \tag{2.18}$$

which is given in units of 1/s and can be determined directly from the measured data $c_{\text{art}}(t)$ and $c_{\text{voi}}(t)$. Using Equation (2.18), Equation (2.15) can be written as

$$c_{\text{voi}}(t) = (c_{\text{art}} \ast k)(t) \ . \tag{2.19}$$

Hence, $k(t)$ can be obtained from the measured data $c_{\text{art}}(t)$ and $c_{\text{voi}}(t)$ using a deconvolution method. Since a fundamental property of the residue function $r(t)$ is $r(0) = \max_t(r(t)) = 1$, one may then determine CBF as

$$\text{CBF} = \frac{1}{\rho_{\text{voi}}} \cdot \max_t(k(t)) \ . \tag{2.20}$$

Using $\max_t(k(t))$ instead of $k(0)$ has particular practical advantages that will be discussed in detail in Section 2.3.1.

The flow-scaled residue function $k(t)$ can further be used to determine the MTT parameter of the tissue volume under consideration. From Equation (2.2), it follows that, for $t > 0$, the following holds:

$$\frac{\mathrm{d}r(t)}{\mathrm{d}t} = -h_{\text{cap}}(t) \ . \tag{2.21}$$

Equation (2.1) can thus be rewritten, and then using integration by parts and Equation (2.18) and Equation (2.20), one obtains

$$\begin{aligned}\mathrm{MTT} &= \int_0^\infty \tau \left(-\frac{\mathrm{d}r(\tau)}{\mathrm{d}\tau}\right) \mathrm{d}\tau \\ &= \int_0^\infty r(\tau)\,\mathrm{d}\tau - \lim_{\xi\to\infty}\left(\tau\, r(\tau)\Big|_0^\xi\right) \\ &= \int_0^\infty r(\tau)\,\mathrm{d}\tau \\ &= \frac{1}{\max\limits_t(k(t))} \cdot \int_0^\infty k(\tau)\,\mathrm{d}\tau\ . \end{aligned} \tag{2.22}$$

Note, it was assumed that there is a constant $T > 0$ such that $r(t) = 0$ for $t > T$. This assumption ensures that

$$\lim_{\xi\to\infty}\left(\tau\, r(\tau)\Big|_0^\xi\right) = \lim_{\xi\to\infty}\left(\xi\, r(\xi)\right) = 0\ . \tag{2.23}$$

The cerebral blood volume (CBV) corresponding to the tissue volume $\mathcal{V}_{\mathrm{voi}}$ represents another diagnostically relevant perfusion parameter and is defined as

$$\mathrm{CBV} = \frac{|\mathcal{V}_{\mathrm{cap}}|}{\rho_{\mathrm{voi}} \cdot |\mathcal{V}_{\mathrm{voi}}|}\ . \tag{2.24}$$

It quantifies the blood volume normalized by the mass of $\mathcal{V}_{\mathrm{voi}}$ and is typically measured in units of ml/100g. The quantity CBV can be computed from the parameters CBF and MTT using the central volume theorem [35, 40], according to which

$$\mathrm{CBF} = \frac{\mathrm{CBV}}{\mathrm{MTT}} \tag{2.25}$$

holds for the perfused volume of interest. Interestingly, this theorem has been recognized for a long time and is already found in a historical publication from 1893 [46]. It states that the perfusion parameters CBV and CBF corresponding to the volume $\mathcal{V}_{\mathrm{voi}}$ of interest are related by the respective temporal parameter MTT that quantifies the mean time that a blood cell needs to pass through its capillary bed. With Equation (2.20) and Equation (2.22), it follows from Equation (2.25) that

$$\mathrm{CBV} = \mathrm{MTT} \cdot \mathrm{CBF} = \frac{1}{\rho_{\mathrm{voi}}} \cdot \int_0^\infty k(\tau)\,\mathrm{d}\tau\ , \tag{2.26}$$

which demonstrates that the CBV parameter can be derived from the flow-scaled residue function $k(t)$ as well. A healthy human brain exhibits a CBV of about 4 ml/100g for grey matter and a CBV of about 2 ml/100g for white matter [39].

Note, the definition of CBV that corresponds to the alternative definition of CBF in Equation (2.16) is

$$\mathrm{CBV}^* = \frac{|\mathcal{V}_{\mathrm{cap}}|}{\rho^*_{\mathrm{voi}} \cdot |\mathcal{V}^*_{\mathrm{voi}}|}\ . \tag{2.27}$$

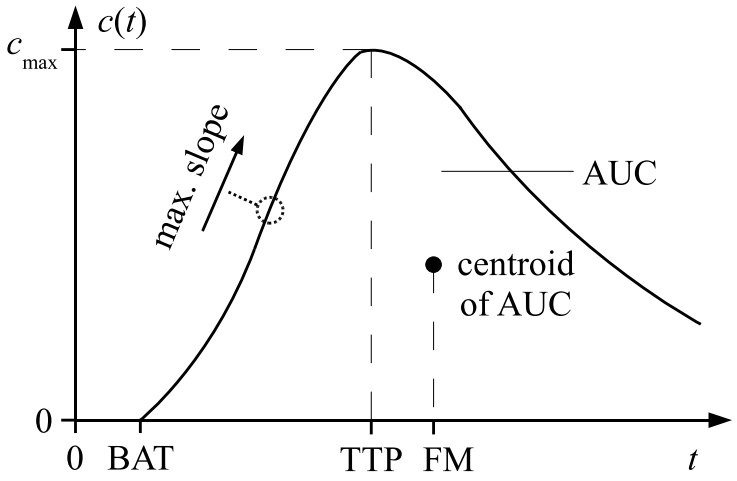

Figure 2.5: Perfusion parameters that are measured directly using the time-concentration curve. See Section 2.2.4 and Section 2.3.1 for explanations (BAT: bolus arrival time, TTP: time-to-peak, FM: first moment, AUC: area under curve).

Accordingly, this alternative definition relates the blood volume to the mass of the parenchyma (and the interstitium) only and explicitly omits the mass of the capillary bed itself.

Furthermore, there are references in the literature that suggest measuring the blood volume in units of ml/ml. This alternative dimensionless quantity may therefore be considered as a measure of blood (or vascular) volume fraction. When relating the absolute volume $|\mathcal{V}_{\text{cap}}|$ of the capillary bed to the entire absolute volume $|\mathcal{V}_{\text{voi}}|$ of interest, a typical average ratio of about 4% will result for the human brain. The reader is referred to [47] for both technical and clinical details.

2.2.4 Additional Perfusion Parameters

Besides the aforementioned quantities CBV, CBF, and MTT, there are additional perfusion parameters such as the time-to-peak (TTP) of the TCC, the maximum contrast agent concentration $c_{\max}$, as well as the first moment (FM) of the TCC, for example. The first moment can be computed by projecting the centroid of the area under the curve (AUC) of the TCC onto the time axis.

Figure 2.5 illustrates the quantities $c_{\max}$, TTP, and FM. The remaining parameter bolus arrival time (BAT) will be explained in Section 2.3.1. In practical measurements, the time point $t = 0$ represents the start of the scanning. A comparison of several perfusion parameters and their clinical impact on the treatment of stroke patients is given in [48].

In summary, Table 2.2 covers the definitions of the most common diagnostically relevant perfusion parameters. Note, this chapter has focused on deconvolution-based methods to determine perfusion parameters. There exist also nondeconvolution-based methods to compute CBF, CBV and MTT. The reader is referred to [29] for the nondeconvolution-based definitions of these parameters.

Parameter	Definition
CBV	$(1/\rho_{\mathrm{voi}}) \cdot \int_0^\infty k(\tau)\,\mathrm{d}\tau$
CBF	$(1/\rho_{\mathrm{voi}}) \cdot \max_t(k(t))$
MTT	$\int_0^\infty k(\tau)\,\mathrm{d}\tau \,/\, \max_t(k(t))$
TTP	$\arg\max_t(c_{\mathrm{voi}}(t))$
FM	$\int_0^\infty c_{\mathrm{voi}}(\tau)\,\tau\,\mathrm{d}\tau \,/\, \int_0^\infty c_{\mathrm{voi}}(\tau)\,\mathrm{d}\tau$

Table 2.2: Summary of perfusion parameters definitions.

2.3 Practical Implementation

This section is devoted to the practical implementation of algorithms for perfusion image analysis. First, the necessary adaptations of the theoretical model from Section 2.2 that are needed for its application to data from real CT and MR scanners will be discussed. Afterwards, commonly used algebraic deconvolution methods will be described and also an overview of alternative approaches will be given. The need for suitable regularization will be motivated and the influence of the regularization parameter on the resulting perfusion estimates will be discussed. For the sake of completeness, also techniques for the pre-processing of the acquired perfusion data will be addressed.

2.3.1 Adaptations of the Model of the Microcirculation

In Section 2.2.1, a model of microcirculation at the tissue level was presented. It was assumed that the average contrast agent concentration $c_{\mathrm{voi}}(t)$ could be measured, which corresponds to a volume $\mathcal{V}_{\mathrm{voi}}$ under consideration that is supplied by one single capillary bed only. Furthermore, it was supposed that the contrast agent concentration $c_{\mathrm{art}}(t)$ could be measured locally at the arterial inlet into the capillary bed. However, real CT and MR scanners are characterized by limited spatial (and contrast) resolution and, in reality, one cannot rely on these two aforementioned assumptions. Thus two major adaptations of the physiological model will be introduced which are necessary once it is to be applied to data from real scanners.

First, during a standard CT and MR perfusion exam, a volume of interest is scanned and the data is reconstructed on a grid of regularly spaced voxels. In the object domain, each voxel volume $\mathcal{V}_{\mathrm{vox}}$ ($|\mathcal{V}_{\mathrm{vox}}| \gg |\mathcal{V}_{\mathrm{voi}}|$) contains numerous capillary beds as well as arterioles and venules that supply and drain these capillary beds, respectively. For the particular case when the volume $\mathcal{V}_{\mathrm{vox}}$ is located completely within a larger artery or vein, there are of course no capillary beds located within $\mathcal{V}_{\mathrm{vox}}$.

The measured signal (X-ray attenuation or MR relaxation rate) in a voxel is thus a combination of the signals from both the capillary beds as well as the arterial and venous vessels [49]. The perfusion parameters that are computed from the voxel's TCC are therefore not true parameters of the capillary perfusion. If no larger artery or vein is located inside the volume $\mathcal{V}_{\mathrm{vox}}$, the model introduced in Section 2.2.1 may be adapted as follows: the measured time-concentration curve $c_{\mathrm{voi}}(t)$ refers to the

average perfusion from the arterioles through the capillary beds to the venules found in $\mathcal{V}_{\text{vox}}$.

The second adaptation of the model concerns the measurement of $c_{\text{art}}(t)$. In reality, it is not possible to locally measure the concentration at the arterial inlet into the volume $\mathcal{V}_{\text{vox}}$. Instead, it is common practice that a global arterial input function is chosen in a large arterial vessel. In brain perfusion imaging, for example, the anterior cerebral artery is often selected [50].

This approach leads to a traveling time of the contrast agent bolus from where the AIF is measured to the location of the tissue volume where $c_{\text{voi}}(t)$ is measured. This traveling time will be referred to as bolus delay. Another physical effect that needs to be taken into consideration is bolus dispersion [51]. It appears as a widening of the shape of the bolus that is caused during the flow from the remote AIF location to the measurement site of $c_{\text{voi}}(t)$.

The bolus delay has two implications. The curve $c_{\text{voi}}(t)$ does not start to rise at the same time point as $c_{\text{art}}(t)$ starts to rise. The difference between these two time points can be defined as the bolus arrival time (BAT), which may be considered as an additional perfusion parameter [52]. Alternatively, the BAT can be defined as the time interval between the start of the scanning and the time when $c_{\text{voi}}(t)$ begins to rise, see Figure 2.5. The results obtained with this alternative definition differ from the results obtained with the first definition by a constant value only.

Second, the flow-scaled residue function $k(t)$ is equal to 0 from $t = 0$ to $t = \text{BAT}$. In addition, due to the bolus dispersion, $k(t)$ will not rise instantaneously to its maximum at $t = \text{BAT}$, but it will have a finite rise time. The time-to-maximum (TMAX) of the flow-scaled residue function, defined as

$$\text{TMAX} = \arg\max_t(k(t)) \,, \tag{2.28}$$

has also been suggested as an additional perfusion parameter [53, 54]. Since the function $k(t)$ can be 0 at $t = 0$ (due to bolus delay), it is reasonable and recommended to estimate CBF as the maximum of $k(t)$ — cf. Equation (2.20) — and not as the value of $k(t)$ at time $t = 0$.

Bolus delay and dispersion may lead to an underestimation of CBF [51]. In order to correct for bolus delay and dispersion several methods have been proposed [55, 56]. The use of local arterial input functions could also reduce the effect of bolus dispersion, see Section 2.4.6. On the other hand, new perfusion parameters (BAT, TMAX) are motivated by these two effects and can be defined accordingly. They represent perfusion characteristics related to the flow of the contrast agent bolus from the selected feeding artery to the respective tissue site.

2.3.2 Deconvolution Using Algebraic Methods

In this section, the robust numerical solution of the main equation of the indicator-dilution theory — Equation (2.19) — by means of algebraic deconvolution methods will be discussed. An overview of further deconvolution methods will then be given in Section 2.3.3. The discretization of Equation (2.19) will be introduced and it will be shown that its solution without regularization leads to nonphysiological results.

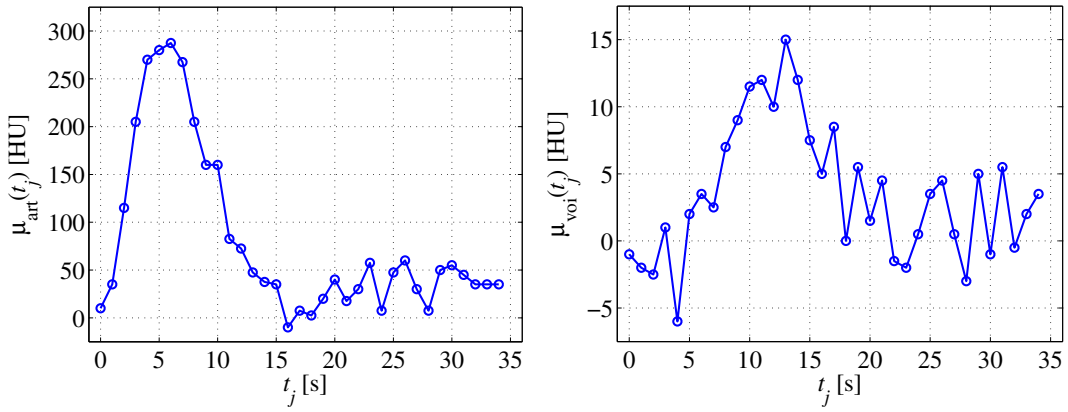

(a) arterial time curve $\mu_{\text{art}}(t_j)$ (b) tissue time curve $\mu_{\text{voi}}(t_j)$

Figure 2.6: Examples of measured time-attenuation curves in perfusion CT in (a) an arterial vessel and (b) in tissue. The time curves have been pre-processed by baseline subtraction and removal of the baseline time frames. The example data is measured at $N = 35$ discrete time points.

Suitable regularization approaches will be explained and motivated by a singular-value-decomposition-based analysis. To illustrate the mathematical concepts, examples will be provided using the time-attenuation curves (TAC) μ_{art} and μ_{voi} shown in Figure 2.6 that were extracted from a real perfusion CT scan.

It is assumed that the measured TACs can be converted to time-concentration curves using a constant of proportionality of 1 g/ml/HU. Details about the conversion, also discussing perfusion MRI data, will be explained in Section 2.4.4.

In practice, the TCCs $c_{\text{art}}(t)$ and $c_{\text{voi}}(t)$ are sampled at discrete time points. These time points are denoted as $t_j = (j-1) \cdot \Delta t$ with $j = 1, \ldots, N$. A typical value of the sampling period Δt is 1 s, for example. Equation (2.19) can be discretized as

$$c_{\text{voi}}(t_j) = \int_0^\infty c_{\text{art}}(\tau)\, k(t_j - \tau)\, \mathrm{d}\tau \approx \Delta t \sum_{i=1}^{N} c_{\text{art}}(t_i)\, k(t_{j-i+1}) \;, \tag{2.29}$$

see [57]. It is assumed that the values of $c_{\text{art}}(t)$ can be neglected for $t > N\Delta t$. Since $k(t) = 0$ for $t < 0$, the end summation index could also be set to j instead of N. By rewriting this expression using matrix-vector notation, one obtains

$$\Delta t \cdot \begin{pmatrix} c_{\text{art}}(t_1) & 0 & \ldots & 0 \\ c_{\text{art}}(t_2) & c_{\text{art}}(t_1) & \ldots & 0 \\ \vdots & \vdots & \ddots & \vdots \\ c_{\text{art}}(t_N) & c_{\text{art}}(t_{N-1}) & \ldots & c_{\text{art}}(t_1) \end{pmatrix} \begin{pmatrix} k(t_1) \\ k(t_2) \\ \vdots \\ k(t_N) \end{pmatrix} = \begin{pmatrix} c_{\text{voi}}(t_1) \\ c_{\text{voi}}(t_2) \\ \vdots \\ c_{\text{voi}}(t_N) \end{pmatrix} , \tag{2.30}$$

or shortly

$$\boldsymbol{A}\,\boldsymbol{k} = \boldsymbol{c} \tag{2.31}$$

where Δt and $c_{\text{art}}(t_j)$ are contained in the matrix $\boldsymbol{A} \in \mathbb{R}^{N \times N}$, and $k(t_j)$ and $c_{\text{voi}}(t_j)$ represent the entries of the vectors $\boldsymbol{k} \in \mathbb{R}^N$ and $\boldsymbol{c} \in \mathbb{R}^N$, respectively. Different ways to discretize Equation (2.19) are investigated in [58]. For example, it was suggested

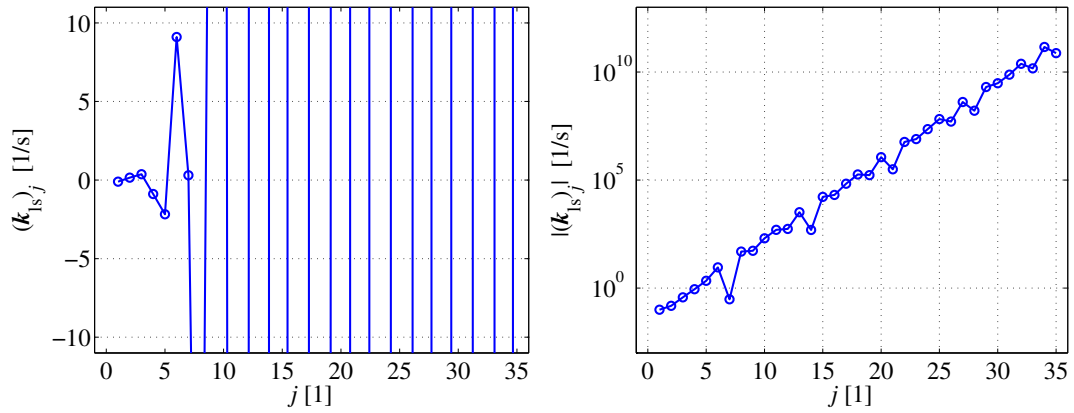

(a) entries of $\boldsymbol{k}_{\mathrm{ls}}$ on a linear scale

(b) absolute values of the entries of $\boldsymbol{k}_{\mathrm{ls}}$ on a logarithmic scale

Figure 2.7: Least-squares solution vector $\boldsymbol{k}_{\mathrm{ls}}$ of Equation (2.31) using the example data from Figure 2.6. $(\boldsymbol{k}_{\mathrm{ls}})_j$ denotes the j-th entry of the vector $\boldsymbol{k}_{\mathrm{ls}}$. The plot shown in figure (a) illustrates the strong oscillations of $(\boldsymbol{k}_{\mathrm{ls}})_j$. The plot given in figure (b) shows the absolute values $|(\boldsymbol{k}_{\mathrm{ls}})_j|$ on a logarithmic scale.

in [59, 60] to use a discretization method with a block-circulant matrix $\boldsymbol{A}$ in order to reduce the influence of the bolus delay. See Appendix A for details.

In order to solve Equation (2.31) for $\boldsymbol{k}$, the least-squares solution $\boldsymbol{k}_{\mathrm{ls}}$ could be computed. It minimizes the squared Euclidean residual norm of the linear systems given by Equations (2.30) and (2.31) and is defined as [61]:

$$\boldsymbol{k}_{\mathrm{ls}} = \underset{\boldsymbol{k}\in\mathbb{R}^N}{\arg\min} \left(||\boldsymbol{A}\,\boldsymbol{k} - \boldsymbol{c}||_2^2 \right) \ . \tag{2.32}$$

Several numerical methods exist that can be used to compute $\boldsymbol{k}_{\mathrm{ls}}$. The reader is referred to [62] for details. However, the least-squares solution $\boldsymbol{k}_{\mathrm{ls}}$ does not represent a suitable solution of Equation (2.31), if the matrix $\boldsymbol{A}$ is ill-conditioned. It can be shown that a matrix $\boldsymbol{A}$ with a structure as shown in Equation (2.30) or Equation (A.3), also known as a Toeplitz matrix, is in fact ill-conditioned [63, 64]. In that case, a small change in $\boldsymbol{c}$ (e.g., due to projection noise) can cause a large change in $\boldsymbol{k}_{\mathrm{ls}}$. The rate at which a change in $\boldsymbol{c}$ influences the solution $\boldsymbol{k}_{\mathrm{ls}}$ is roughly proportional to the condition number of $\boldsymbol{A}$, defined as $\sigma_1/\sigma_{\hat{r}}$ where $\hat{r} \equiv \mathrm{rank}(\boldsymbol{A})$ [61].

As an example, Figure 2.7 shows the solution $\boldsymbol{k}_{\mathrm{ls}}$ of the example data from Figure 2.6. The solution is strongly oscillating and even has a rising amplitude. It is obvious that this solution has nothing in common with the real physiological behavior of the flow-scaled residue function.

In order to get a better understanding of why $\boldsymbol{k}_{\mathrm{ls}}$ is not a meaningful solution and to motivate the regularization approach, the matrix equation Equation (2.31) will be investigated. The singular value decomposition (SVD) which is a well-known method for the analysis of matrix equations [61, 64] will be used for this purpose and

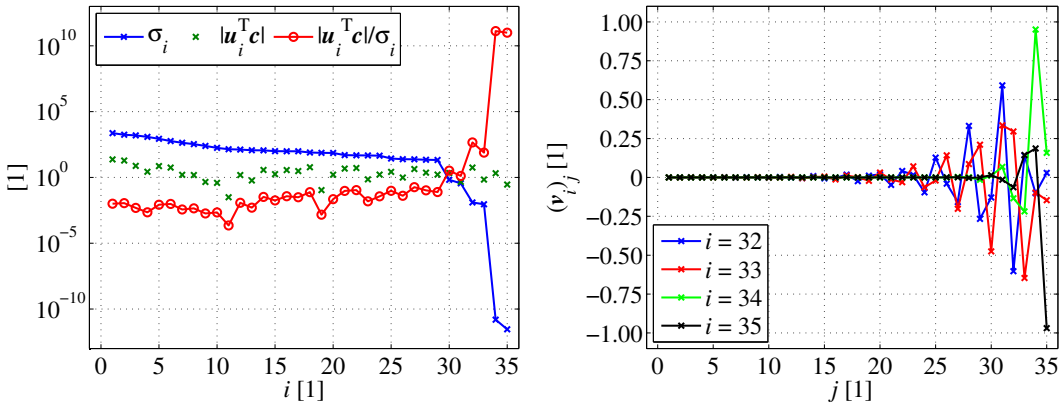

(a) $|\boldsymbol{u}_i^{\mathrm{T}}\boldsymbol{c}|/\sigma_i$ on a logarithmic scale (b) entries of $\boldsymbol{v}_i$ on a linear scale

Figure 2.8: SVD analysis of the matrix $\boldsymbol{A}$ constructed from the example data shown in Figure 2.6. (a) Plot of the absolute values of the weighting factors $(\boldsymbol{u}_i^{\mathrm{T}}\boldsymbol{c})/\sigma_i$ and of their individual components $|\boldsymbol{u}_i^{\mathrm{T}}\boldsymbol{c}|$ and σ_i. (b) Plot of the entries of the right singular vectors $\boldsymbol{v}_i$ of $\boldsymbol{A}$ for $i \in \{32, 33, 34, 35\}$. $(\boldsymbol{v}_i)_j$ denotes the j-th entry of $\boldsymbol{v}_i$.

it will be described next. For the particular case of a square matrix $\boldsymbol{A} \in \mathbb{R}^{N\times N}$ with $\hat{r}$ linearly independent rows and columns[2], it is defined as

$$\boldsymbol{A} = \boldsymbol{U}\,\boldsymbol{\Sigma}\,\boldsymbol{V}^{\mathrm{T}} = \sum_{i=1}^{\hat{r}} \boldsymbol{u}_i\,\sigma_i\,\boldsymbol{v}_i^{\mathrm{T}}\ , \tag{2.33}$$

where $\boldsymbol{U} = [\boldsymbol{u}_1, \ldots, \boldsymbol{u}_{\hat{r}}]$ and $\boldsymbol{V} = [\boldsymbol{v}_1, \ldots, \boldsymbol{v}_{\hat{r}}]$ are unique orthogonal matrices composed of the left and right singular vectors $\boldsymbol{u}_i$ and $\boldsymbol{v}_i$, respectively [61]. The diagonal matrix $\boldsymbol{\Sigma} = \mathrm{diag}\,(\,\sigma_1, \ldots, \sigma_{\hat{r}}\,)$ contains the singular values σ_i in non-increasing order $\sigma_1 \geq \sigma_2 \geq \ldots \geq \sigma_{\hat{r}} > 0$. The least-squares solution $\boldsymbol{k}_{\mathrm{ls}}$ of Equation (2.31) using the SVD of $\boldsymbol{A}$ is actually given by

$$\boldsymbol{k}_{\mathrm{ls}} = \sum_{i=1}^{\hat{r}} \frac{\boldsymbol{u}_i^{\mathrm{T}}\,\boldsymbol{c}}{\sigma_i}\,\boldsymbol{v}_i\ , \tag{2.34}$$

see again [61].

The SVD will now be used to analyze Equation (2.31) with $\boldsymbol{A}$ and $\boldsymbol{c}$ which are constructed from the data shown in Figure 2.6. Figure 2.8(a) represents a plot of the absolute values of the expressions $(\boldsymbol{u}_i^{\mathrm{T}}\boldsymbol{c})/\sigma_i$ that occur in Equation (2.34). These factors weight the right singular vectors $\boldsymbol{v}_i$ of $\boldsymbol{A}$. The entries of the right singular vectors $\boldsymbol{v}_i$ are shown in Figure 2.8(b) for $i \in \{32, 33, 34, 35\}$.

It is known from numerical analysis that the discrete Picard condition represents a means to analyze discrete ill-conditioned problems [63, 64]. This condition is violated, if the expressions $\boldsymbol{u}_i^{\mathrm{T}}\boldsymbol{c}$ do not decay faster, on average, than the singular values σ_i until a threshold value is reached where the singular values level off. The reader is

[2]The number of rows and columns in $\boldsymbol{A}$ that only contain zeros is determined by the number N_{lz} of leading zeros in the series $c_{\mathrm{art}}(t_j), j = 1, \ldots, N$. Therefore, the rank of $\boldsymbol{A}$ is less or equal $N - N_{\mathrm{lz}}$. After the subtraction of the baseline, it may happen that the first entry $c_{\mathrm{art}}(t_1)$ is zero, see Section 2.4.4, and that $\boldsymbol{A}$ thus becomes rank-deficient.

referred to [64] for a more detailed explanation of the discrete Picard condition and its relation to the Picard condition from which it is derived. A usual reason for the violation of the discrete Picard condition is noise in the measured data that the matrix $\boldsymbol{A}$ is based on. One can see that the discrete Picard condition is actually violated in the example shown in Figure 2.8(a) [65]. Consequently, the absolute values of the ratios $(\boldsymbol{u}_i^{\mathrm{T}}\boldsymbol{c})/\sigma_i$ — which represent the weighting factors of the right singular vectors $\boldsymbol{v}_i$ — become very large.

The absolute values of the entries of the right singular vectors $\boldsymbol{v}_i$ shown in Figure 2.8(b) tend to be larger for higher vector indices j compared to lower indices j. A similar trend can also be seen in the solution vector $\boldsymbol{k}_{\mathrm{ls}}$, see Figure 2.7(b).

To obtain a numerically stable result, a filter is used for regularization. The filter should suppress the influences of small singular values σ_i or, equivalently, the influences of high absolute values of the weighting factors $(\boldsymbol{u}_i^{\mathrm{T}}\boldsymbol{c})/\sigma_i$. The regularized solution $\boldsymbol{k}_l$, where l is a regularization parameter, is given by

$$\boldsymbol{k}_l = \sum_{i=1}^{\hat{r}} \left(f_{l,i} \, \frac{\boldsymbol{u}_i^{\mathrm{T}} \, \boldsymbol{c}}{\sigma_i} \right) \boldsymbol{v}_i \; . \tag{2.35}$$

Two common definitions of the filter factors $f_{l,i}$ will be introduced. First, the filter factors $f^{\,(\mathrm{tsvd})}$ correspond to the truncated singular value decomposition (TSVD) approach and are defined with a sharp threshold at l,

$$f_{l,i}^{(\mathrm{tsvd})} = \begin{cases} 0 & \text{for } \sigma_i < l \; , \\ 1 & \text{for } \sigma_i \geq l \; . \end{cases} \tag{2.36}$$

Second, the filter factors $f_{l,i}^{(\mathrm{tikh})}$ are based on the Tikhonov regularization approach and characterized by a smooth weighting function centered around l,

$$f_{l,i}^{(\mathrm{tikh})} = \frac{\sigma_i^2}{\sigma_i^2 + l^2} \; . \tag{2.37}$$

The (absolute) regularization parameter l is usually computed relative to the maximum singular value σ_1, i.e.,

$$l = l_{\mathrm{rel}} \, \sigma_1 \; . \tag{2.38}$$

The relative regularization parameter l_{rel} is supposed to lie in the interval between 0 and 1.

In order to illustrate the Tikhonov filter factors, Figure 2.9 shows a plot of the function $f_l^{\,(\mathrm{tikh})}(\sigma) = \sigma^2/(\sigma^2 + l^2)$ which is — unlike Equation (2.37) — defined for a continuous range of σ. For determining $f_l^{\,(\mathrm{tikh})}(\sigma)$, $\sigma_1 = 1$ was assumed. It can be seen that, for increasing l (i.e., stronger regularization), the values of $f_l^{\,(\mathrm{tikh})}(\sigma)$ decrease for all σ.

Interestingly, the solution $\boldsymbol{k}_l^{(\mathrm{tikh})}$ of Equation (2.31) using the filter factors $f_{l,i}^{(\mathrm{tikh})}$ is equivalent to minimizing the weighted sum of the squared Euclidean residual norm $||\boldsymbol{A}\,\boldsymbol{k} - \boldsymbol{c}||_2^2$ and the squared Euclidean solution norm $||\boldsymbol{k}||_2^2$ [64]; i.e.,

$$\boldsymbol{k}_l^{(\mathrm{tikh})} = \underset{\boldsymbol{k} \in \mathbb{R}^N}{\arg\min} \left(\, ||\boldsymbol{A}\,\boldsymbol{k} - \boldsymbol{c}||_2^2 + l^2 \, ||\boldsymbol{k}||_2^2 \, \right) \; . \tag{2.39}$$

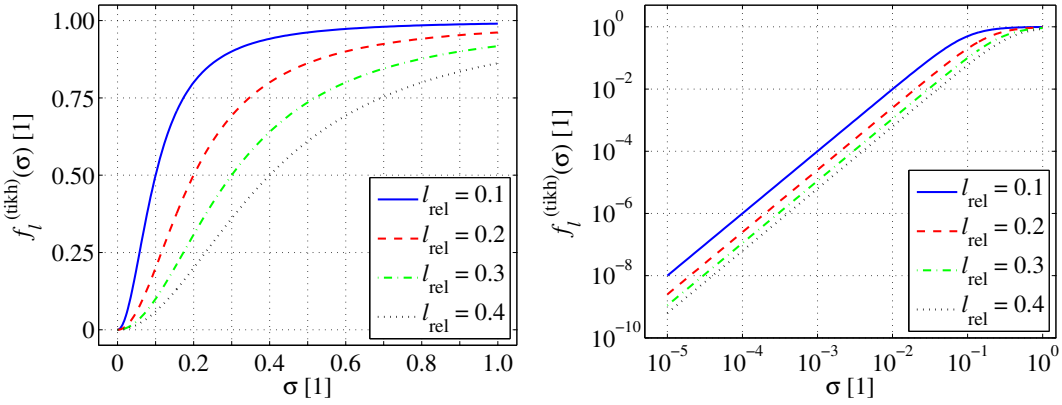

(a) linear plot of $f_l^{(\mathrm{tikh})}(\sigma)$ (b) double logarithmic plot of $f_l^{(\mathrm{tikh})}(\sigma)$

Figure 2.9: (a) Linear and (b) double logarithmic plot of the Tikhonov filter factor $f_l^{(\mathrm{tikh})}(\sigma)$ as a function of the singular value $\sigma \in [10^{-5}, 1]$.

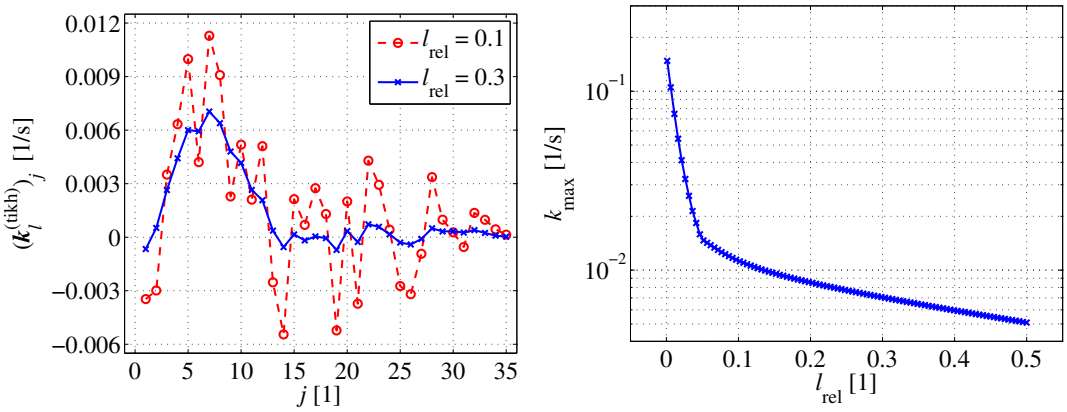

(a) entries of regularized solution $\boldsymbol{k}_l^{(\mathrm{tikh})}$ (b) dependency of $k_{\max} \equiv \max_j((\boldsymbol{k}_l^{(\mathrm{tikh})})_j)$ on l_{rel} plotted on a logarithmic scale

Figure 2.10: Deconvolution with Tikhonov regularization: (a) Regularized solution $\boldsymbol{k}_l^{(\mathrm{tikh})}$ for two different regularization parameters l_{rel} and (b) maximum entry of $\boldsymbol{k}_l^{(\mathrm{tikh})}$ as a function of l_{rel}. $(\boldsymbol{k}_l^{(\mathrm{tikh})})_j$ denotes the j-th entry of the vector $\boldsymbol{k}_l^{(\mathrm{tikh})}$.

Figure 2.10(a) shows the solution $\boldsymbol{k}_l^{(\mathrm{tikh})}$ computed for two different regularization parameters. The solution for $l_{\mathrm{rel}} = 0.1$ still shows some nonphysiological oscillations. However, the solution for $l_{\mathrm{rel}} = 0.3$ can in fact be interpreted as a flow-scaled residue function in the presence of bolus delay and dispersion, cf. Section 2.3.1. Figure 2.10(b) illustrates a plot of $\max_j((\boldsymbol{k}_l^{(\mathrm{tikh})})_j)$, which is proportional to CBF (see Section 2.2.3 and Table 2.2), as a function of l_{rel}. Apparently, CBF depends on the choice of regularization parameter. Choosing an optimal regularization parameter that will lead to physiologically reasonable estimates will be discussed in Section 2.3.4.

Finally, Algorithm 2.1 summarizes the algorithm to compute perfusion parameters based on the TSVD approach. This algorithm will actually be used in Chapter 4 to compute the relevant perfusion parameters. Note, the factors 6000, 100, and 60 in line 13–15 ensure that the output values have the desired units.

2.3.3 Alternative Deconvolution Approaches

The algebraic deconvolution approach from Section 2.3.2 is very commonly applied to analyze perfusion data. Yet, deconvolution problems arise in many other applications, and numerous alternative algorithms to solve these problems have been developed [66]. This section will provide a brief overview of alternative deconvolution approaches that have also been applied to perfusion data.

The Fourier transform (FT) represents a standard method to solve deconvolution problems [62], and it has also been evaluated to analyze perfusion data [57, 67, 68, 69]. Interestingly, the FT-based deconvolution approach is mathematically equivalent to the SVD-based deconvolution approach with a block-circulant matrix $\boldsymbol{A}$, cf. Appendix A [59, 70, 71, 72]. However, results obtained with SVD-based and FT-based deconvolution can be different because the chosen regularization approaches for these two methods are usually not equivalent. The regularization in the context of the FT-based deconvolution approach can be implemented by means of a modified Wiener filter [67], for example. The reader is referred to [72, 73] for a detailed analysis of the equivalence of SVD-based and FT-based regularization approaches.

In contrast to the model-independent deconvolution approaches also model-dependent approaches exist. Model-dependent approaches assume a certain shape of the residue function. For example, in [57, 75] a decaying exponential function was used which makes the deconvolution more stable since it reduces the degrees of freedom of the residue function [57]. However, if the underlying residue function is different from the model the perfusion parameters may not be estimated correctly.

Deconvolution using orthogonal polynomials was investigated in [76]. An iterative deconvolution algorithm based on maximum likelihood expectation maximization (MLEM) algorithm was proposed in [77]. An approach using Gaussian processes was evaluated in [78]. The deconvolution algorithm in [79] uses a nonlinear stochastic regularization method.

A comprehensive comparison of all available deconvolution methods has not been carried out yet. The SVD-based deconvolution approach, which is available in sev-

Algorithm 2.1: TSVD algorithm to compute perfusion parameters.

Input: time-resolved data $\mu(\boldsymbol{x}_i, t_j)$ ($i = 1, \ldots, N_{\text{vox}}$ where N_{vox} is the number of voxels) with sample period Δt,
AIF location $\boldsymbol{x}_{\text{aif}} \equiv \boldsymbol{x}_{i_{\text{aif}}}$ where i_{aif},
number B of baseline frames

Output: CBF parameter map $I_{\text{cbf}}(\boldsymbol{x}_i)$ (unit: ml/100g/min),
CBV parameter map $I_{\text{cbv}}(\boldsymbol{x}_i)$ (unit: ml/100g),
MTT parameter map $I_{\text{mtt}}(\boldsymbol{x}_i)$ (unit: s)

1 `// constants suitable for CT brain perfusion data`
2 $l_{\text{rel}} \leftarrow 0.2$ `// see Section 2.3.4`
3 $\rho_{\text{voi}} \leftarrow 1.04$ g/ml `// typical density of brain tissue [74]`
4 convert $\mu_{\text{art}}(t_j) \equiv \mu(\boldsymbol{x}_{\text{aif}}, t_j)$ to $c_{\text{art}}(t_j)$ according to Equation (2.40)
5 construct $\boldsymbol{A}$ using $c_{\text{art}}(t_j)$ according to Equation (2.30)
6 compute SVD of $\boldsymbol{A}$, cf. Equation (2.33)
7 compute $f_{l,i}^{(\text{tsvd})}$ according to Equation (2.36)
8 **foreach** voxel position $\boldsymbol{x}_i$ **do**
9 convert $\mu(\boldsymbol{x}_i, t_j)$ to $c_{\text{voi}}(t_j) \equiv c(\boldsymbol{x}_i, t_j)$ according to Equation (2.40)
10 construct $\boldsymbol{c}$ using $c_{\text{voi}}(t_j)$ according to Equation (2.30)
11 compute $\boldsymbol{k}_l^{(\text{tsvd})}$ according to Equation (2.35)
12 `// compute perfusion parameters (Table 2.2)`
`numint: numerical integration applied to vector entries`
13 $I_{\text{cbf}}(\boldsymbol{x}_i) \leftarrow 6000 \cdot (1/\rho_{\text{voi}}) \cdot \max_j((\boldsymbol{k}_l^{(\text{tsvd})})_j)$
14 $I_{\text{cbv}}(\boldsymbol{x}_i) \leftarrow 100 \cdot (1/\rho_{\text{voi}}) \cdot \Delta t \cdot \operatorname{numint}_j((\boldsymbol{k}_l^{(\text{tsvd})})_j)$
15 $I_{\text{mtt}}(\boldsymbol{x}_i) \leftarrow 60 \cdot I_{\text{cbv}}(\boldsymbol{x}_i) \,/\, I_{\text{cbf}}(\boldsymbol{x}_i)$
16 **end**

eral software packages [80, 81, 82], is comparably simple to implement and can be considered as the current standard method in perfusion image analysis.

2.3.4 Determination of the Regularization Parameter

Figure 2.10(b) demonstrated that (the maximum of) the solution $\boldsymbol{k}_l^{(\mathrm{tikh})}$ depends on the regularization parameter l_{rel}. Consequently, the computed perfusion values — which can be derived from $\boldsymbol{k}_l^{(\mathrm{tikh})}$ according to Table 2.2 — vary for different l_{rel}. As an example, the CBF value will be underestimated systematically for large l_{rel}.

Therefore, an optimal choice of l_{rel} is crucial. A simple approach is to empirically determine a fixed value l_{rel}. This approach is often used in practice, and a typical value in brain perfusion CT is, for example, $l_{\mathrm{rel}} = 0.2$ [81]. However, there exist more sophisticated approaches as well to determine the values l_{rel} independently for each voxel position [83]. Since the required amount of regularization depends roughly on the signal-to-noise ratio (SNR), these approaches can be more flexible when the SNR is spatially variant.

In [57, 59, 60], an oscillation index (OI) was defined to determine the intensity of oscillations of the flow-scaled residue function. The regularization can then be varied until the OI value falls below a certain threshold.

The L-curve criterion represents a model-independent method to determine l (and l_{rel}) [45, 84, 85]. The L-curve is defined by a double logarithmic plot of the squared Euclidean norm $||\boldsymbol{k}_l||_2^2$ of the solution versus the squared Euclidean norm $||\boldsymbol{A}\boldsymbol{k}_l - \boldsymbol{c}||_2^2$ of the residual for a range of different l values. The optimal regularization parameter l_{opt} can be found at the location of the characteristic corner point of the L-curve.

Another method to determine an appropriate regularization parameter is generalized cross validation as described in [63, 86]. An implementation of the L-curve method and the generalized cross validation can be found in [65].

Furthermore, a parameter estimation method that uses a-priori knowledge of the behavior of the residue function was proposed in [87].

Kudo et al. [81] reported that two manufacturers applied a fixed threshold value l_{rel} in their perfusion analysis software. Unfortunately, the clinical use of methods with adaptive threshold values is rarely described in the current literature.

2.4 Perfusion Data Pre-processing

This section gives an overview of pre-processing techniques that can be applied in order to enhance the quality of the estimated perfusion parameters. Pre-processing occurs prior to the deconvolution step which may be implemented as described in Section 2.3.2.

A simple, yet mandatory pre-processing step consists of the conversion to contrast agent concentration values, see Section 2.4.4. Further pre-processing steps are used to enhance the image quality (e.g., noise reduction) and to correct for artifacts (e.g., motion correction, partial volume correction) and specific properties of the blood (e.g., correction of differences in hematocrit). There are also pre-processing steps that can optimize the analysis of the perfusion value maps (e.g., segmentation of

certain anatomical structures) and the application workflow (e.g., automated AIF estimation).

The order of the pre-processing steps presented in this section can act as a guideline for their practical implementation. However, a different ordering can of course be reasonable as well. Finally, this overview cannot include all details regarding suitable pre-processing steps. The reader is referred to the available literature for in-depth discussions.

2.4.1 Motion Correction

Patient motion (e.g., due to head movement or breathing) can result in a sudden change of the attenuation values at the fixed (stationary) voxel positions. Since this change in the attenuation value is caused by motion and not by contrast agent flow, the computed perfusion values can be severely biased. A practical approach for motion correction is to register all time frames of the reconstructed data set onto the first time frame [88]. A 3-D registration should be used because it can also correct motion that occurs perpendicular to the orientation of the reconstructed slices. For a brain perfusion scan, a rigid registration may be sufficient. Conversely, in abdominal perfusion imaging, a non-rigid registration may be better suited to compensate for the deformations due to breathing.

As an alternative to registration, use of group-wise motion correction based on an optimization of a global cost function has been suggested [89]. There are also several approaches for motion correction in functional magnetic resonance imaging (fMRI) data [90]. These approaches may be used for perfusion MRI data as well since both types of data typically consist of T2*-weighted echo-planar imaging (EPI) data [91]. However, the dynamic signal changes are relatively higher in dynamic susceptibility contrast-MRI (DSC-MRI) data, i.e. MR perfusion imaging with T2* weighting, when compared to fMRI data [91] which must be taken into account when adapting fMRI-based motion correction algorithms to DSC-MRI data.

A related issue is streak artifact in reconstructed perfusion CT images that are caused by patient motion that occurs while the projection data corresponding to a single time frame is acquired. In perfusion MRI images, ghosting artifacts can arise if the patient moves during the data acquisition. These kinds of artifact cannot be corrected by inter-frame motion correction. Instead, dedicated reconstruction algorithms would be required. As a practical alternative, time frames that exhibit severe reconstruction artifacts may simply be removed from the data set (i.e., from the series of successive time frames), which corresponds to the elimination of invalid sampling points of the voxel-specific TCCs.

2.4.2 Noise Reduction

In the course of a perfusion exam, the measured signal in tissue that is caused by the contrast agent flow can be very low. For the case of perfusion CT, for example, tissue enhancements of less than 10 HU are measured. Hence, noise in the reconstructed images can be of a similar order of magnitude as the signal in tissue itself. Conse-

quently, noise reduction should be taken into consideration in order to improve the accuracy of the estimated perfusion parameters.

Noise reduction can be implemented as a spatial smoothing of the data. Using a basic approach, each time frame can be filtered independently of the other time frames, and linear isotropic filters (e.g., based on a Gaussian filter kernel) may be applied. Alternatively, anisotropic filters that preserve edges and avoid blurring of large vessels can also be employed [92].

Both linear and nonlinear filtering in the temporal dimension — i.e., between successive time frames — represent further methods for noise reduction [93]. It should be noted, however, that the regularization during the deconvolution step is equivalent to linear filtering in the temporal domain.

Recently, sophisticated 4-D filtering techniques have been proposed that perform filtering in both the spatial and the temporal dimension and that are optimized for perfusion data [94, 95]. Fitting of the TCCs to a model function such as a gamma-variate function is also a means for noise reduction [88].

2.4.3 Segmentation

A segmentation of certain anatomical structures in the reconstructed data set can optimize the perfusion image analysis [82, 96]. For example, the TCCs could then be analyzed only in regions of interest where blood flow is actually expected [97]. Other regions such as air, bone, cerebrospinal fluid (CSF) and calcifications can be neglected. A segmentation and the subsequent removal of vessels is useful in order to optimize the quantitative analysis of perfusion parameters in tissue. Such a vessel segmentation can be performed prior to the deconvolution step, but it can also be implemented as a post-processing step as described in [98].

2.4.4 Conversion to Contrast Agent Concentration

Neither for the case of CT imaging nor for the case of MR imaging can the TCCs $c_{\text{art}}(t)$ and $c_{\text{voi}}(t)$ be measured directly. Instead, the measurement is a superposition of the signal from the tissue itself and the contrast agent. Since the deconvolution approach presented in Section 2.3.2 expects that the functions $c_{\text{art}}(t_j)$ and $c_{\text{voi}}(t_j)$ only refer to the signal caused by the contrast agent, the tissue signal must be subtracted. Furthermore, the measured signal must be converted to a contrast agent concentration value.

In perfusion CT, it is assumed that the (underlying) contrast agent concentration value is proportional to the (measured) X-ray attenuation value [99, 100]. Since deconvolution is a linear operation, the constant of proportionality does not influence the computed flow-scaled residue function. It can also be seen that the additional perfusion parameters from Section 2.2.4 are independent of this constant. Therefore, this constant is usually set to $K_{\text{ct}} = 1$ g/ml/HU for the sake of simplicity. The baseline value μ_0 can be computed as the mean of $\mu(t_j)$ during the B acquired time frames before the contrast agent bolus arrives in the arterial input function. The

conversion formula from an attenuation value $\mu(t_j)$ (corresponding to a particular voxel) into the respective contrast agent concentration value $c(t_j)$ then reads as

$$c(t_j) = K_{\mathrm{ct}} \cdot (\mu(t_{j+B-1}) - \mu_0) \ , \tag{2.40}$$

$$\mu_0 = \frac{1}{B} \sum_{i=1}^{B} \mu(t_i) \ . \tag{2.41}$$

In perfusion MRI, however, the contrast agent concentration value is not proportional to the received signal $s_{\mathrm{mr}}(t_j)$ (in one voxel). Instead, it can be determined using the following formula:

$$c(t_j) = -\frac{K_{\mathrm{mr}}}{TE} \ln\left(\frac{s_{\mathrm{mr}}(t_{j+B-1})}{s_{\mathrm{mr},0}}\right) \ , \tag{2.42}$$

$$s_{\mathrm{mr},0} = \frac{1}{B} \sum_{i=1}^{B} s_{\mathrm{mr}}(t_i) \ , \tag{2.43}$$

see [34]. Here, K_{mr} is a constant of proportionality which — with a similar argument as for K_{ct} — can have a norm of one and TE is the echo-time of the MR sequence. It must be noted, however, that the constant K_{mr} can be different for blood and tissue due to differences in T2* relaxivities [49, 101]. This complicates absolute quantification of cerebral perfusion as discussed in [102]. Furthermore, studies have shown that fully oxygenated blood, for example, demonstrates a nonlinear relationship between the measured difference in T2* relaxation rate and contrast agent concentration [103].

Note, if only one time frame is considered as the baseline (i.e., if B=1), then $c(0) = 0$, and the matrix $\boldsymbol{A}$ defined by Equations (2.30) and (2.31) will be rank-deficient, cf. Section 2.3.2.

2.4.5 Correction of Hematocrit Differences

Hematocrit (Hct) is a value that describes the proportion of the blood that consists of red blood cells. Hct is higher in arteries than in capillaries. Consequently, the proportion of the plasma in the blood, given by the difference $(1 - \mathrm{Hct})$, has a higher value in capillaries than in arteries. Since the contrast agent is distributed in the plasma only, the amount of plasma has a direct influence on the measured Hounsfield value or MR relaxation rate.

If the Hct difference is not corrected, it may bias the absolute quantification of the contrast agent concentration. A constant dimension-less correction factor κ, derived from the known Hct values in arteries and capillaries (often set to $\kappa = 0.73$) has been proposed [35, 98]. The measured TCCs $c_{\mathrm{voi}}(t)$ is then multiplied with κ to avoid the bias due to different Hct values.

2.4.6 Automated Arterial Input Function Estimation

The total time for the perfusion image analysis can be shortened and the analysis can be made user-independent by an automated estimation of the arterial input function. Several methods have been proposed that detect one global AIF [104, 105, 106].

An interesting alternative approach is to estimate several local AIFs, which would be better suited to the theoretical model that was introduced in Section 2.2 [107, 108, 109]. Since the local arteries are often small, this approach can have several disadvantages [102]. For example, partial volume effects — cf. Section 2.4.7 — can be more severe when compared to choosing one global AIF in a larger vessel. Perfusion analysis using local AIFs was actually investigated in [110] and the authors state that it produced more useful CBF maps.

Besides the arterial input function $c_{\text{art}}(t)$ the venous outflow function $c_{\text{ven}}(t)$ could also be detected automatically. Knowledge about the venous outflow function could be used to automatically correct for partial volume effects which are described next.

2.4.7 Correction of Partial Volume Effects

Due to limited spatial resolution in reconstructed perfusion CT and MR data, the AIF can suffer from partial volume effects [40]. This effect can lead to an underestimation of the AIF and consequently to incorrect perfusion values. To correct for partial volume effects in the AIF, several methods have been proposed [111, 112, 113]. Commonly, the peak concentration value within a larger venous vessel or the area under the curve of a large venous vessel is used to rescale the AIF [45].

Chapter 3

A Model for Filtered Backprojection Reconstruction Artifacts due to Time-varying Attenuation Values

Overview:
In this chapter, a theoretical analysis of a certain kind of image reconstruction artifact that is relevant in C-arm CT perfusion imaging is carried out. Namely, FBP reconstruction artifacts arise if the attenuation values vary, e.g. due to contrast agent flow, during the acquisition of the projection data.

A novel spatio-temporal model based on the concept of derivative-weighted point spread functions is derived. This model leads to a better understanding of this kind of artifacts. For validation, the model is compared to results from numerical simulations and to C-arm CT measurements of a flow phantom. The model can also be applied to systematically investigate artifact reduction strategies. In this chapter, the influence of the angular interval length, which is used for the data acquistion, on these artifacts is investigated.

This chapter is based on "A model for filtered backprojection reconstruction artifacts due to time-varying attenuation values in perfusion C-arm CT", by A. Fieselmann, F. Dennerlein, Y. Deuerling-Zheng, J. Boese, R. Fahrig, and J. Hornegger. *Physics in Medicine and Biology*, 56(12):3701–3717, 2011 [27].

3.1 Introduction

3.1.1 Motivation

Analytical image reconstruction algorithms based on the FBP are usually employed to reconstruct the large-volume data sets acquired with state-of-the-art C-arm CT systems [13]. Using general-purpose computing on graphics processing units (GPGPU), FBP-based algorithms (e.g., Feldkamp-type algorithms [16]) can be implemented such that they are computationally very fast [114]. Thus, they can be used for image reconstruction during interventional procedures such as catheter-guided stroke treatment where time is a critical factor (Sections 1.2.1 and 4.1.1).

There exist also alternative CT image reconstruction approaches such as algebraic and statistical methods [15]. However, currently these approaches are not frequently employed for (C-arm) CT reconstruction [115]. In general, the time that is needed for image reconstruction is longer with these approaches when compared to the FBP.

The FBP reconstruction assumes constant attenuation values of the object during the acquisition of the projection data. Reconstruction artifacts arise if this assumption is violated. As it has been mentioned in Section 1.3.2 already, contrast agent flow in perfusion imaging with C-arm CT systems, which have acquisition times of several seconds per C-arm rotation, can cause this violation (Figure 3.1). For the analysis and optimization of FBP-based reconstruction algorithms, a good understanding of artifacts due to time-varying attenuation values is essential. Note, in CT perfusion imaging the duration of the data acquisition is sufficiently short to assume constant attenuation values.

In this chapter, a novel spatio-temporal model for this kind of artifact will be presented. This model can be applied to estimate the magnitude of artifacts and to optimize reconstruction parameters. It could also be used to develop new FBP-based dynamic reconstruction algorithms that are based on an inversion of this model.

3.1.2 Previous Work

There exists some previous work that concerns FBP reconstruction artifacts due to time-varying attenuation values.

In [116] a mathematical formalism is presented to describe these artifacts in parallel-beam geometry CT scanning and it is validated using computer simulations. But this formalism assumes periodic changes of the contrast agent concentration and is therefore not suitable to describe artifacts in perfusion imaging with time-attenuation curves that are non-periodic.

The work presented in [117] and [118] also show reconstruction results using computer simulation of objects with time-varying attenuation values during the scanning but no mathematical analyses of the artifacts were carried out.

Similar reconstruction problems as mentioned above arise in dynamic single-photon emission computed tomography (SPECT) when the tracer concentration changes during one camera rotation. In [119] and [120] the FBP reconstruction is used for dynamic SPECT and the resulting artifacts were investigated qualitatively and quantitatively but without derivation of a model.

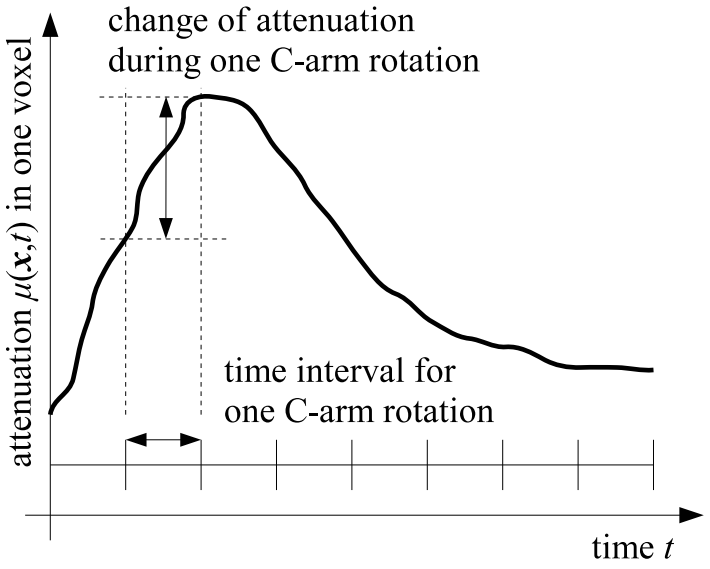

Figure 3.1: Illustration of the change of attenuation value in one voxel during one C-arm rotation.

FBP reconstruction artifacts due to the time-varying opacification of a vessel, when using a C-arm mounted X-ray image intensifier (XRII) for 3-D imaging, are investigated in [121] but no mathematical model was developed.

Artifacts due to time-varying contrast agent concentration in perfusion CT with a slowly rotating CT scanner are investigated in [122]. The reconstruction error of a time-attenuation curve is formulated as a low-pass filtering process. However, it is not studied how artifacts propagate into other reconstructed voxel attenuation values in the image, which is the focus of this chapter.

3.2 Background of FBP Reconstruction

In this section, the notation will be presented with a brief description of the direct 2-D fan-beam FBP reconstruction. A more detailed description of these methods can be found in [14].

The X-ray source rotates with a constant angular velocity ω_s on a circular path of radius R around the origin of the coordinate system (Figure 3.2). The location $\boldsymbol{a}(\lambda(t))$ of the source at time t is given by

$$\boldsymbol{a}(\lambda(t)) = (R\,\cos(\lambda(t)),\, R\,\sin(\lambda(t)))^\mathrm{T} \tag{3.1}$$

$$\lambda(t) = \omega_\mathrm{s}\,t + \lambda_0 \tag{3.2}$$

where $\lambda(t)$ is the view-angle and λ_0 is the starting view-angle at $t = 0$. In this chapter, the variable λ always depends explicitly on t although this is not always indicated for simplicity. The following unit vectors are defined:

$$\boldsymbol{e}_\mathrm{u}(\lambda) = (-\sin(\lambda),\, \cos(\lambda))^\mathrm{T} \tag{3.3}$$

$$\boldsymbol{e}_\mathrm{w}(\lambda) = (\cos(\lambda),\, \sin(\lambda))^\mathrm{T}\,. \tag{3.4}$$

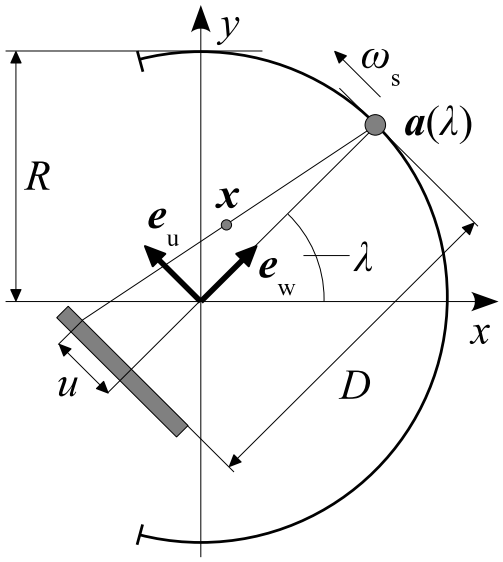

Figure 3.2: Illustration of the (simplified) C-arm CT acquisition geometry.

The function $u^*(\boldsymbol{x}, \lambda)$ gives the coordinate where a ray from source location $\boldsymbol{a}(\lambda)$ passing through $\boldsymbol{x}$ intersects the detector. It can be computed as

$$u^*(\boldsymbol{x}, \lambda) = \frac{D\, \boldsymbol{x}^{\mathrm{T}} \boldsymbol{e}_{\mathrm{u}}(\lambda)}{R - \boldsymbol{x}^{\mathrm{T}} \boldsymbol{e}_{\mathrm{w}}(\lambda)} \tag{3.5}$$

where D is the source-to-detector distance. It is assumed that the attenuation values $\mu(\boldsymbol{x}, \lambda)$ at locations $\boldsymbol{x} = (x, y)^{\mathrm{T}}$ have view-angle-dependent values. Furthermore, it is assumed that no truncation of the projection images occurs and that the attenuation values are zero in the region $x^2 + y^2 \geq R^2$.

The projection $p(\lambda, u)$, which is measured at the detector coordinate u, can be written using the usual definition of the delta function:

$$p(\lambda, u) = \iint \mu(\boldsymbol{x}, \lambda)\, \delta(u^*(\boldsymbol{x}, \lambda) - u)\, \mathrm{d}x\, \mathrm{d}y\ . \tag{3.6}$$

In this chapter, all integrals without explicit integration endpoints should be interpreted as the limit value when the lower and upper endpoints approach $-\infty$ and $+\infty$, respectively. The pixel value $\mu_{\mathrm{rec}}(\boldsymbol{r}, t_{\mathrm{rec}})$ at location $\boldsymbol{r}$ corresponding to the state at time t_{rec} can be reconstructed using the FBP reconstruction with an angular sliding window function $w_\Lambda(\lambda, \gamma)$:

$$\begin{aligned}\mu_{\mathrm{rec}}(\boldsymbol{r}, t_{\mathrm{rec}}) = \int \frac{R\, D}{(R - \boldsymbol{r}^{\mathrm{T}} \boldsymbol{e}_{\mathrm{w}}(\lambda(t)))^2} \int p(\lambda(t), u)\, h_{\mathrm{ramp}}\Big(u^*(\boldsymbol{r}, \lambda(t)) - u\Big) \\ \cdot\, \frac{D}{(u^2 + D^2)^{1/2}}\, w_\Lambda\Big(\lambda(t) - \lambda(t_{\mathrm{rec}}), \arctan(u/D)\Big)\, \mathrm{d}u\, \mathrm{d}t\ .\end{aligned} \tag{3.7}$$

Here $h_{\mathrm{ramp}}(u)$ denotes the usual ramp filter kernel and $\gamma = \arctan(u/D)$ is the fan-angle. This reconstruction formula assumes a consistent data set of projection images,

i.e. there is no change of the attenuation values over time. The function $w_\Lambda(\lambda, \gamma)$ is zero outside an angular interval of size Λ:

$$w_\Lambda(\lambda,\gamma) = \begin{cases} m_\Lambda(\lambda + \Lambda/2, \gamma) & \text{for } -\Lambda/2 \leq \lambda \leq \Lambda/2 \\ 0 & \text{otherwise .} \end{cases} \tag{3.8}$$

The minimum interval for Λ is the short-scan range $\pi + \gamma_\mathrm{m}$ where γ_m is the full fan-angle. The function $m_\Lambda(\lambda, \gamma)$ compensates for redundant data inside the angular interval due to the fan-beam acquisition geometry. An example for $m_\Lambda(\lambda, \gamma)$ is the weighting function proposed in [123],

$$m_\Lambda(\lambda,\gamma) = \begin{cases} \sin^2\left(\frac{\pi}{4}\,\frac{\lambda}{\Gamma/2+\gamma}\right) & \text{for } 0 \leq \lambda < \Gamma + 2\gamma \\ 1 & \text{for } \Gamma + 2\gamma \leq \lambda < \pi + 2\gamma \\ \sin^2\left(\frac{\pi}{4}\,\frac{\pi+\Gamma-\lambda}{\Gamma/2-\gamma}\right) & \text{for } \pi + 2\gamma \leq \lambda < \pi + \Gamma \\ 0 & \text{otherwise .} \end{cases} \tag{3.9}$$

with $\Gamma = \Lambda - \pi$. With the definition of the FBP from Equation (3.7) that uses the window $w_\Lambda(\lambda, \gamma)$, an image corresponding to a certain time point t_rec can be reconstructed. The time point could be flexibly chosen if the C-arm system could perform continuous C-arm rotations. With current C-arm systems the C-arm rotates in alternating directions (Section 1.3.1) therefore the choice for t_rec is restricted to the time point at the center during one short-scan rotation. The artifact model in Section 3.3 is actually applicable to both scenarios, continuous and bi-directional C-arm rotations.

3.3 Spatio-temporal Artifact Model

In this section, a novel artifact model will be derived and interpreted. The key idea of this model is to separate the artifact into two components, one that depends on the dynamic process, i.e. the change of attenuation values, and one that depends on the acquisition geometry and the reconstruction algorithm parameters.

3.3.1 Derivation

The expression from Equation (3.6) is substituted into Equation (3.7) and by changing the order of integration one obtains:

$$\begin{aligned} \mu_\mathrm{rec}(\boldsymbol{r}, t_\mathrm{rec}) = \iiiint & \frac{R\,D^2}{(R - \boldsymbol{r}^\mathrm{T}\boldsymbol{e}_\mathrm{w}(\lambda(t)))^2}\,\mu(\boldsymbol{x}, \lambda(t))\; h_\mathrm{ramp}\Big(u^*(\boldsymbol{r}, \lambda(t)) - u\Big) \\ & \cdot \Big(u^2 + D^2\Big)^{-1/2}\; w_\Lambda\Big(\lambda(t) - \lambda(t_\mathrm{rec}), \arctan(u/D)\Big) \\ & \cdot\; \delta(u^*(\boldsymbol{x}, \lambda(t)) - u)\,\mathrm{d}u\,\mathrm{d}t\,\mathrm{d}x\,\mathrm{d}y\;. \end{aligned} \tag{3.10}$$

The delta function is evaluated and the result is re-arranged into the following two functions (see Appendix B for details):

$$\mu_\mathrm{rec}(\boldsymbol{r}, t_\mathrm{rec}) = \iint \chi(\boldsymbol{r} - \boldsymbol{x}, \boldsymbol{x}, t_\mathrm{rec})\,\mathrm{d}x\,\mathrm{d}y \tag{3.11}$$

$$\begin{aligned}\chi(\boldsymbol{s},\boldsymbol{x},t_{\mathrm{rec}}) = \int \frac{R\,D^2}{(R-(\boldsymbol{s}+\boldsymbol{x})^{\mathrm{T}}\boldsymbol{e}_{\mathrm{w}}(\lambda(t)))^2}\, h_{\mathrm{ramp}}\Big(u^*(\boldsymbol{s}+\boldsymbol{x},\lambda(t)) - u^*(\boldsymbol{x},\lambda(t))\Big) \\ \cdot\ \mu\Big(\boldsymbol{x},\lambda(t)\Big)\left((u^*(\boldsymbol{x},\lambda(t)))^2 + D^2\right)^{-1/2} \\ \cdot\ w_\Lambda\Big(\lambda(t)-\lambda(t_{\mathrm{rec}}), \arctan(u^*(\boldsymbol{x},\lambda(t))/D)\Big)\,\mathrm{d}t\ . \end{aligned} \tag{3.12}$$

The function $\chi(\boldsymbol{s},\boldsymbol{x},t_{\mathrm{rec}})$ can be interpreted as the reconstruction associated with a point object located at $\boldsymbol{x}$ which has time-varying attenuation values $\mu(\boldsymbol{x},\lambda(t))$. The variable $\boldsymbol{s} = (s_x, s_y)^{\mathrm{T}}$ denotes the distance vector from the point object in the reconstructed image and t_{rec} is the temporal center of the sliding window used in the FBP reconstruction. A detailed interpretation of $\chi(\boldsymbol{s},\boldsymbol{x},t_{\mathrm{rec}})$ will be given in Section 3.3.2.

Now the focus will be on the time dependence of $\mu(\boldsymbol{x},\lambda(t))$. It will be assumed that it is a smooth function without discontinuities. If the contrast agent bolus is injected into the antecubital vein, for example, the bolus will pass through the heart and lungs. Thus, when it arrives in the brain it has been low-pass filtered and is a smooth curve. Using this assumption $\mu(\boldsymbol{x},\lambda(t))$ can be represented as a Taylor series around $\lambda(t_{\mathrm{rec}})$:

$$\mu(\boldsymbol{x},\lambda(t)) = \sum_{n=0}^{\infty} \left.\frac{\mathrm{d}^n\mu(\boldsymbol{x},\lambda(t))}{\mathrm{d}\lambda^n}\right|_{\lambda(t)=\lambda(t_{\mathrm{rec}})} \frac{(\lambda(t)-\lambda(t_{\mathrm{rec}}))^n}{n!}\ . \tag{3.13}$$

According to Equation (3.2) the second-order derivative of $\lambda(t)$ is zero. Therefore, the following total derivative exists (the proof is given in Appendix C):

$$\begin{aligned}\left.\frac{\mathrm{d}^n\mu(\boldsymbol{x},\lambda(t))}{\mathrm{d}t^n}\right|_{t=t_{\mathrm{rec}}} &= \left.\frac{\partial^n\mu(\boldsymbol{x},\lambda(t))}{\partial\lambda^n}\right|_{\lambda(t)=\lambda(t_{\mathrm{rec}})} \left(\left.\frac{\mathrm{d}\lambda(t)}{\mathrm{d}t}\right|_{t=t_{\mathrm{rec}}}\right)^n \\ &= \left.\frac{\mathrm{d}^n\mu(\boldsymbol{x},\lambda(t))}{\mathrm{d}\lambda^n}\right|_{\lambda(t)=\lambda(t_{\mathrm{rec}})} \omega_{\mathrm{s}}^n\ . \end{aligned} \tag{3.14}$$

Equation (3.14) and Equation (3.13) are combined and the new expression for $\mu(\boldsymbol{x},\lambda(t))$ is plugged into Equation (3.12). Then the order of summation and integration is changed and the result is split into these two functions

$$\chi(\boldsymbol{s},\boldsymbol{x},t_{\mathrm{rec}}) = \sum_{n=0}^{\infty} \left.\frac{\mathrm{d}^n\mu(\boldsymbol{x},t)}{\mathrm{d}t^n}\right|_{t=t_{\mathrm{rec}}} \omega_{\mathrm{s}}^{-n}\, P_n(\boldsymbol{s},\boldsymbol{x},\lambda(t_{\mathrm{rec}})) \tag{3.15}$$

$$\begin{aligned}P_n(\boldsymbol{s},\boldsymbol{x},\lambda_{\mathrm{rec}}) =& R\,D^2 \int \frac{(\lambda-\lambda_{\mathrm{rec}})^n}{n!}\left(R-(\boldsymbol{s}+\boldsymbol{x})^{\mathrm{T}}\boldsymbol{e}_{\mathrm{w}}(\lambda)\right)^{-2} \\ &\cdot\ h_{\mathrm{ramp}}\Big(u^*(\boldsymbol{s}+\boldsymbol{x},\lambda) - u^*(\boldsymbol{x},\lambda)\Big) \\ &\cdot\ \left((u^*(\boldsymbol{x},\lambda))^2 + D^2\right)^{-1/2} \\ &\cdot\ w_\Lambda\Big(\lambda-\lambda_{\mathrm{rec}}, \arctan((u^*(\boldsymbol{x},\lambda))/D)\Big)\,\mathrm{d}\lambda \end{aligned} \tag{3.16}$$

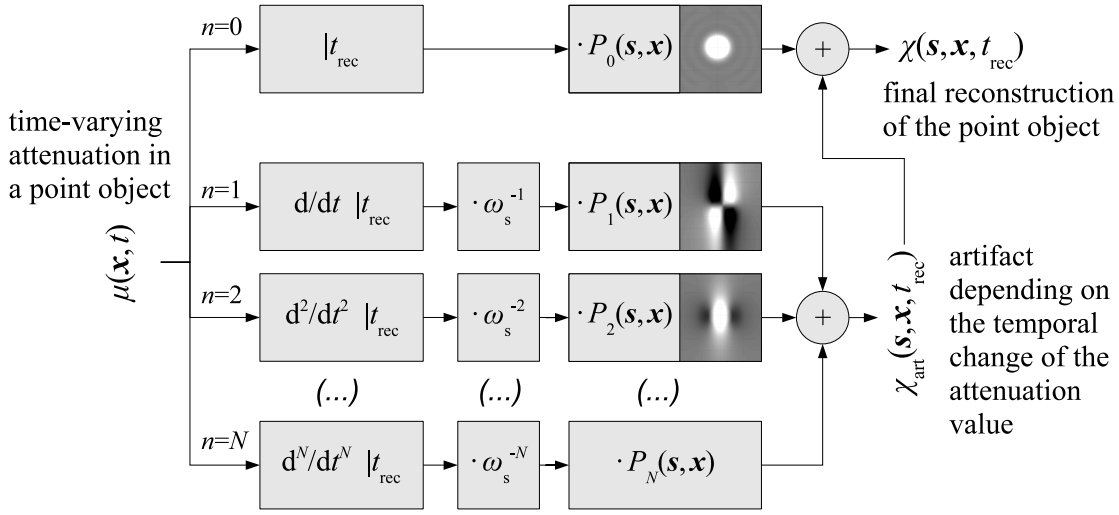

Figure 3.3: Spatio-temporal artifact model: a point object at $\boldsymbol{x}$ with time-varying attenuation value $\mu(\boldsymbol{x}, t)$ creates an artifact around $\boldsymbol{x}$ in the reconstructed image. The artifact is described by $\chi_{\text{art}}(\boldsymbol{s}, \boldsymbol{x}, t_{\text{rec}})$ where $\boldsymbol{s}$ is the distance vector from $\boldsymbol{x}$. This function is the sum of the functions $P_n(\boldsymbol{s}, \boldsymbol{x})$ that are each weighted with the n-th derivative of $\mu(\boldsymbol{x}, t)$, which is evaluated at the central time point t_{rec} of the set of projection data, and a C-arm-angular-velocity-(ω_{s})-dependent factor. The final reconstruction $\chi(\boldsymbol{s}, \boldsymbol{x}, t_{\text{rec}})$ is a superposition of the artifact χ_{art} and the product $\mu(\boldsymbol{x}, t_{\text{rec}})P_0(\boldsymbol{s}, \boldsymbol{x})$ where P_0 denotes the (conventional) point spread function due to the scanning and reconstruction process.

where $\lambda_{\text{rec}} \equiv \lambda(t_{\text{rec}})$. Substituting λ by $\lambda + \lambda_{\text{rec}}$ and using Equation (3.8) to determine the integration interval yields:

$$\begin{aligned} P_n(\boldsymbol{s}, \boldsymbol{x}, \lambda_{\text{rec}}) = & R\, D^2 \int_{-\Lambda/2}^{+\Lambda/2} \frac{\lambda^n}{n!} \Big(R - (\boldsymbol{s} + \boldsymbol{x})^{\mathrm{T}} \boldsymbol{e}_{\text{w}}(\lambda + \lambda_{\text{rec}}) \Big)^{-2} \\ & \cdot\ h_{\text{ramp}}\Big(u^*(\boldsymbol{s} + \boldsymbol{x}, \lambda + \lambda_{\text{rec}}) - u^*(\boldsymbol{x}, \lambda + \lambda_{\text{rec}}) \Big) \\ & \cdot\ \Big((u^*(\boldsymbol{x}, \lambda + \lambda_{\text{rec}}))^2 + D^2 \Big)^{-1/2} \\ & \cdot\ w_\Lambda\Big(\lambda, \arctan((u^*(\boldsymbol{x}, \lambda + \lambda_{\text{rec}}))/D) \Big)\, \mathrm{d}\lambda\ . \end{aligned} \tag{3.17}$$

Equations (3.11), (3.15) and (3.17) constitute the artifact model that will be interpreted in the following section.

3.3.2 Interpretation

According to Equation (3.11) the reconstructed image $\mu_{\text{rec}}(\boldsymbol{r}, t_{\text{rec}})$ is the superposition of the functions $\chi(\boldsymbol{s}, \boldsymbol{x}, t_{\text{rec}})$. In a theoretically exact reconstruction with $\mu_{\text{rec}}(\boldsymbol{r}, t_{\text{rec}}) = \mu(\boldsymbol{r}, t_{\text{rec}})$ this function would be:

$$\chi_{\text{theoretical}}(\boldsymbol{s}, \boldsymbol{x}, t_{\text{rec}}) = \delta(\boldsymbol{s})\, \mu(\boldsymbol{x}, t_{\text{rec}})\ . \tag{3.18}$$

However, in reality due to the finite detector pixel width not all spatial frequencies in the projections can be measured and the ramp filter kernel has to be adapted.

The reconstruction of a point object will then lead to a slightly blurred point object with a smooth edge. The point spread function (PSF) provides a description of the blurring [124]. With the parameter $P_{\text{static}}(\boldsymbol{s}, \boldsymbol{x})$ denoting the PSF that characterizes the scanning and reconstruction process of a static, time-independent point object at $\boldsymbol{x}$, one gets:

$$\chi_{\text{static}}(\boldsymbol{s}, \boldsymbol{x}, t_{\text{rec}}) = P_{\text{static}}(\boldsymbol{s}, \boldsymbol{x})\, \mu(\boldsymbol{x}, t_{\text{rec}}) \; . \tag{3.19}$$

Equation (3.19) and Equation (3.11) can be interpreted as transformations of the true attenuation values μ into the reconstructed attenuation values μ_{rec}. The function $P_{\text{static}}(\boldsymbol{s}, \boldsymbol{x})$ is shift-variant because it depends explicitly on $\boldsymbol{x}$. In the fan-beam FBP this property is evidenced by a non-uniform noise propagation [125], for example.

In Equation (3.15) the variable $\lambda(t_{\text{rec}})$ is a system parameter that is determined by the start and end scan angle. For a time-independent object, i.e. when $\mathrm{d}\mu(\boldsymbol{x}, t)/\mathrm{d}t = 0$, Equation (3.15) reduces to Equation (3.19). However, Equation (3.15) is more general because it has been derived for dynamic, time-dependent objects. In this equation, the function $\chi(\boldsymbol{s}, \boldsymbol{x}, t_{\text{rec}})$ is a superposition of weighted functions which are denoted by $P_n(\boldsymbol{s}, \boldsymbol{x})$. The weights are the n-th order derivative values of $\mu(\boldsymbol{x}, t)$, evaluated at t_{rec}, and the n-th power of $1/\omega_{\text{s}}$. Because the functions P_n with $n \geq 1$ have a similar character as P_0 they will be denoted as n-th order derivative-weighted point spread functions (DWPSF).

The function $\chi(\boldsymbol{s}, \boldsymbol{x}, t_{\text{rec}})$ can be split into a term corresponding to the static case as in Equation (3.19) and into terms that depend on first or higher order derivatives of $\mu(\boldsymbol{x}, t)$:

$$\chi(\boldsymbol{s}, \boldsymbol{x}, t_{\text{rec}}) = \mu(\boldsymbol{x}, t_{\text{rec}})\, P_0(\boldsymbol{s}, \boldsymbol{x}, \lambda(t_{\text{rec}})) + \chi_{\text{art}}(\boldsymbol{s}, \boldsymbol{x}, t_{\text{rec}}) \tag{3.20}$$

$$\chi_{\text{art}}(\boldsymbol{s}, \boldsymbol{x}, t_{\text{rec}}) = \sum_{n=1}^{\infty} \left. \frac{\mathrm{d}^n \mu(\boldsymbol{x}, t)}{\mathrm{d}t^n} \right|_{t=t_{\text{rec}}} \omega_{\text{s}}^{-n}\, P_n(\boldsymbol{s}, \boldsymbol{x}, \lambda(t_{\text{rec}})) \; . \tag{3.21}$$

The artifact function $\chi_{\text{art}}(\boldsymbol{s}, \boldsymbol{x}, t_{\text{rec}})$ results from a time-varying attenuation value $\mu(\boldsymbol{x}, \lambda(t))$ at $\boldsymbol{x}$. The artifact is centered around $\boldsymbol{x}$ and the vector $\boldsymbol{s}$ gives the distance from the center. Figure 3.3 shows an illustration of the artifact model where for simplicity the scan geometry variable λ_{rec} has been omitted. Furthermore, in this illustration the infinite sum is approximated by the finite sum from $n = 1$ to $n = N$.

Each term in the artifact model consists of two components. The first component is the rate-of-change of the time-attenuation curve — given by its temporal derivative value — relative to the C-arm rotation speed. The second component is the function $P_n(\boldsymbol{s}, \boldsymbol{x}, \lambda_{\text{rec}})$ that depends only on the scan geometry $(R, D, \Lambda, \lambda_{\text{rec}})$ and on the reconstruction parameters $(h_{\text{ramp}}(u), m_{\Lambda}(\lambda, \gamma))$. Changing the speed of the time-attenuation curve and the rotation speed of the C-arm by the same factor $a > 1$, i.e.

$$\mu^{\text{fast}}(\boldsymbol{x}, t) = \mu(\boldsymbol{x}, at) \tag{3.22}$$

$$\omega_{\text{s}}^{\text{fast}} = a\, \omega_{\text{s}} \; , \tag{3.23}$$

does not change the artifact function $\chi_{\text{art}}(\boldsymbol{s}, \boldsymbol{x}, t_{\text{rec}})$. However, if only the C-arm rotation speed is increased while the time-attenuation curve remains constant then

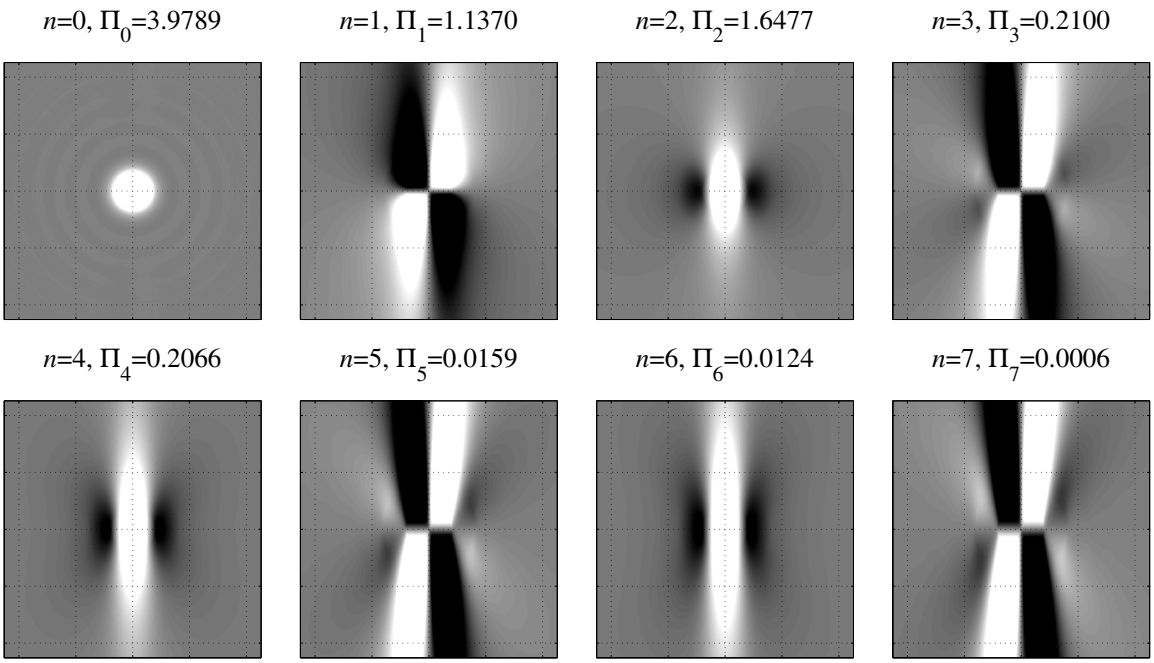

Figure 3.4: Plot of the derivative-weighted point spread functions $P_n(\boldsymbol{s}, (0,0)^{\mathrm{T}}, 0)$ computed from the parameters given in Table 3.1. The variable Π_n is the absolute amplitude of P_n. The images have a windowing from $-\Pi_n/2$ (black) to $+\Pi_n/2$ (white) and their dotted grids have a spacing of 1 mm.

the artifact function changes. The change is non-linear and the weights of the higher-order DWPSFs is less than when compared to the weights of the lower-order DWPSFs. It can also be seen that

$$\lim_{\omega_{\mathrm{s}} \to \infty} \chi_{\mathrm{art}}(\boldsymbol{s}, \boldsymbol{x}, \lambda_{\mathrm{rec}}) = 0 \tag{3.24}$$

which means that the artifact disappears if the acquisition time interval becomes very short. Figure 3.4 shows the n-th order DWPSFs computed for typical scan and reconstruction parameters (Table 3.1). For better visualization, the windowing is set relative to their absolute amplitudes Π_n defined as

$$\Pi_n(\boldsymbol{x}, \lambda_{\mathrm{rec}}) = \max_{\boldsymbol{s}} \left(\left| P_n(\boldsymbol{s}, \boldsymbol{x}, \lambda_{\mathrm{rec}}) \right| \right) \ . \tag{3.25}$$

The 0-th order DWPSF describes the normal blurring of a point object due to the scan and reconstruction process. The integral value over the function P_0 is close to unity whereas the integral values over P_n with odd n are close to zero. Interestingly, the DWPSFs with odd values for n and even values for n have similar patterns, respectively.

The pattern can be explained by investigation of Equation (3.17). In this equation only the factor $\zeta_n(\lambda) \equiv \lambda^n / n!$ depends on n. For $n = 0$ this factor is a constant and all view-angles contribute equally to the integral value. For $n > 0$ the function $\zeta_n(\lambda)$ introduces a non-uniform view-angle-dependent weighting. If n is odd then $\zeta_n(\lambda)$ is an odd function and the values at the integral endpoints have different signs. If n is

Parameter	Symbol	Value
starting view-angle	λ_0	–100°
view-angle increment	$\Delta\lambda$	1°
number of views per rotation	N_{views}	201
angular range per rotation	$\Lambda = (N_{\text{views}} - 1) \cdot \Delta\lambda$	200°
angular velocity of the C-arm	ω_{s}	60 °/s
time per rotation	$T_{\text{rot}} = \Lambda/\omega_{\text{s}}$	3.33 s
source-to-isocenter distance	R	800 mm
source-to-detector distance	D	1200 mm
number of detector pixels	N_{detpix}	600
detector pixel size	Δu	0.6 mm
total detector width	$U = N_{\text{detpix}} \cdot \Delta u$	360 mm
full fan-angle	$\gamma_{\text{m}} = 2\arctan(U/(2\,D))$	17.1°
redundancy weighting function	m_Λ	see Equation (3.9)
ramp filter kernel	h_{ramp}	Shepp-Logan, see [14]
number of reconstructed pixels	—	$301 \cdot 301$
reconstructed pixel size	—	$0.015 \cdot 0.015$ mm^2

Table 3.1: C-arm CT scan and reconstruction parameters used for the numerical examples with the artifact model.

even then the values of $\zeta_n(\lambda)$ are equal at the integral endpoints. These properties cause similar functions $P_n(\boldsymbol{s}, \boldsymbol{x}, \lambda_{\text{rec}})$ for even and odd n, respectively.

Now the variable λ_{rec} will be investigated. If $\boldsymbol{x} = (0,0)^{\text{T}}$ then $P_n(\boldsymbol{s}, \boldsymbol{x}, \lambda_{\text{rec}})$ depends on λ_{rec} only by $\boldsymbol{s}^{\text{T}}\boldsymbol{e}_{\text{u}}(\lambda + \lambda_{\text{rec}})$ and $\boldsymbol{s}^{\text{T}}\boldsymbol{e}_{\text{w}}(\lambda + \lambda_{\text{rec}})$. By expressing $\boldsymbol{s}$ in polar coordinates as $\boldsymbol{s} = (r\cos(\phi),\, r\sin(\phi))^{\text{T}}$ and using common trigonometric identities one gets:

$$\boldsymbol{s}^{\text{T}}\boldsymbol{e}_{\text{u}}(\lambda + \lambda_{\text{rec}}) = r\,\sin(\phi - \lambda - \lambda_{\text{rec}}) \tag{3.26}$$

$$\boldsymbol{s}^{\text{T}}\boldsymbol{e}_{\text{w}}(\lambda + \lambda_{\text{rec}}) = r\,\cos(\phi - \lambda - \lambda_{\text{rec}})\,. \tag{3.27}$$

It can be seen that a change of the variable λ_{rec} by a certain angle can be compensated by a rotation of the coordinate system by the same angle in the opposite direction of rotation. Therefore, changing λ_{rec} results in a rotation of the function $P_n(\boldsymbol{s}, (0,0)^{\text{T}}, \lambda_{\text{rec}})$ around the origin. Generally, i.e. also for $\boldsymbol{x} \neq (0,0)^{\text{T}}$, one can see that $P_n(\boldsymbol{s}, \boldsymbol{x}, \lambda_{\text{rec}})$ is 2π periodic with respect to λ_{rec}.

3.4 Numerical Example

In this section, the artifact model will be used to predict artifacts from typical temporal changes of attenuation values in perfusion imaging. For validation, the predictions from the model will be compared with numerical simulations. Finally, the model will be used for an analysis of different reconstruction parameter values.

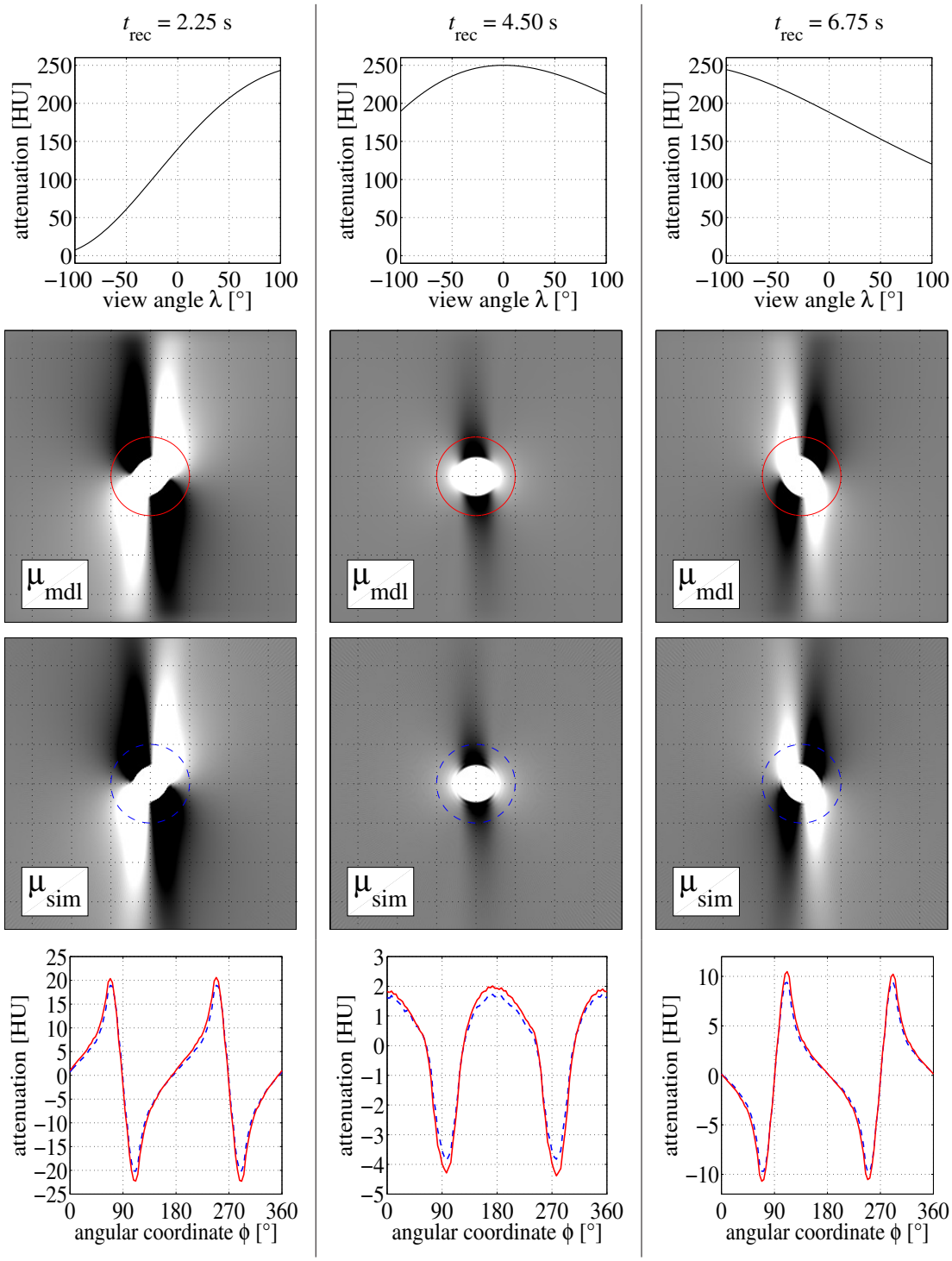

Figure 3.5: Examples for artifacts due to inconsistent data: (1st row) view-angle-dependent attenuation value inside the modeled origin-centered artery with radius 1 mm, (2nd row) predicted reconstruction using the artifact model, (3rd row) reconstruction using numerical simulations, (4th row) plot of attenuation values along the circular paths shown in the above images (μ_{mdl} ——, μ_{sim} - - - -). The images have a windowing from –5 HU (black) to +5 HU (white) and their dotted grids have a spacing of 2.5 mm.

3.4.1 Methods

A mathematical phantom $\mu_{\text{pha}}(\boldsymbol{x}, t)$ is defined to model a large cerebral artery inside the human head. It consists of two circles that are centered in the origin: a smaller circle with radius $r_{\text{pha,art}} = 1$ mm and a larger circle with radius $r_{\text{pha,head}} = 100$ mm. In order to simulate contrast agent flow, the attenuation values inside the smaller circle vary over time t according to a function $\mu_{\text{pha,art}}(t)$ proposed in [57]:

$$\mu_{\text{pha}}(\boldsymbol{x}, t) = \begin{cases} \mu_{\text{w}} + \mu_{\text{pha,art}}(t) & \text{for } x^2 + y^2 \leq r_{\text{pha,art}}^2 \\ \mu_{\text{w}} & \text{for } r_{\text{pha,art}}^2 < x^2 + y^2 \leq r_{\text{pha,head}}^2 \\ 0 & \text{otherwise} \end{cases} \tag{3.28}$$

with

$$\mu_{\text{pha,art}}(t) = \frac{A}{(\alpha\,\beta\,\exp(-1))^{\alpha}}\,\hat{\tau}^{\alpha}\,\exp(-\hat{\tau}/\beta)\,H(\hat{\tau})\;. \tag{3.29}$$

$H(\hat{\tau})$ is the unit step function, $\mu_{\text{w}} = 0.18\,\text{cm}^{-1}$ is the X-ray attenuation of water, $A = 0.25\,\mu_{\text{water}}$ is the maximum enhancement, $\alpha = 3.0$ and $\beta = 1.5$ are shape parameters and $\hat{\tau} = t/\text{s}$ is a dimensionless quantity where s denotes seconds.

The image $\mu_{\text{mdl}}(\boldsymbol{x}, t_{\text{rec}})$ is computed using the artifact model. According to Equation (3.11) the final 2-D reconstruction μ_{rec} is a superposition of the 2-D functions χ which can be thought of as individual reconstructions of (theoretical) point objects. To apply the artifact model, the point objects are first approximated by discrete pixels. Then χ is computed for each pixel and μ_{rec} is determined using a discretized version of Equation (3.11), see Algorithm 3.1.

In order to compute χ, only the first four functions P_n $(n = 0, \ldots, 3)$ are considered assuming 4-th and higher order derivative values can be neglected due to the smoothness of $\mu_{\text{pha,art}}(t)$. The parameters for the model are taken from Table 3.1. The reconstruction time points t_{rec} are 2.25 s, 4.50 s and 6.75 s. These time points were chosen to investigate the reconstruction from data acquired during the inflow, plateau and outflow phase of the time curve (see first row in Figure 3.5). It was assumed that the data was acquired from three individual C-arm rotations which all started at the same starting angle to allow for better comparison.

For the numerical simulation the scan parameters from Table 3.1 are used to simulate C-arm CT scanning of the central slice of the phantom during the time interval $t \in [t_{\text{rec}} - T_{\text{rot}}/2,\, t_{\text{rec}} + T_{\text{rot}}/2]$. The reconstruction time points t_{rec} are the same as for the artifact model. A FBP reconstruction $\mu_{\text{sim}}(\boldsymbol{x}, t_{\text{rec}})$ is generated from the simulated projections by applying the reconstruction parameters from Table 3.1.

3.4.2 Results and Discussion

In Figure 3.5 each column corresponds to a different time t_{rec}. The first row shows a plot of the view-angle-dependent attenuation value inside the artery. The second and third rows show the images μ_{mdl} and μ_{sim} respectively. The last row shows values of μ_{mdl} and μ_{sim} evaluated along a circular path (radius 2.5 mm) around the origin of the coordinate system. This path is also depicted in the images in the second and third row. The windowing of the images was chosen from –5 HU to +5 HU. Because the contrast agent enhancement in tissue is about 5 to 10 HU — given an arterial

Algorithm 3.1: Algorithm to model a FBP reconstruction from data with time-varying attenuation values. Note, for simplicity all variables are denoted as continuous variables whereas in a practical implementation the variables can take discrete values only.

Input: time-varying (true) attenuation values $\mu(\boldsymbol{x}, t)$,
time point t_{rec} (central time point of the C-arm rotation),
scan and reconstruction parameters $(R, h_{\text{ramp}}, \ldots)$
Output: modeled FBP reconstruction $\mu_{\text{rec}}(\boldsymbol{r})$

$\mu_{\text{rec}}(\boldsymbol{r}) \leftarrow 0 \quad \forall\, \boldsymbol{r}$
foreach $\boldsymbol{x}$ **do**
  // $\tilde{\chi}(\boldsymbol{s})$ describes the artifact that arises from a point object at $\boldsymbol{x}$ with time-varying attenuation values $\mu(\boldsymbol{x}, t)$
  $\tilde{\chi}(\boldsymbol{s}) \leftarrow 0 \quad \forall\, \boldsymbol{s}$
  // consider N DWPSFs (e.g., $N = 4$)
  for $n = 0$ **to**$N - 1$ **do**
    compute $\tilde{P}_n(\boldsymbol{s}) \equiv P_n(\boldsymbol{s}, \boldsymbol{x}, \lambda(t_{\text{rec}}))$ according to Equation (3.17)
    compute $\tilde{d}_n \equiv \frac{\mathrm{d}^n \mu(\boldsymbol{x}, \lambda(t))}{\mathrm{d}t^n}|_{t=t_{\text{rec}}}$
    $\tilde{\chi}(\boldsymbol{s}) \leftarrow \tilde{\chi}(\boldsymbol{s}) + \tilde{d}_n \cdot \omega_{\text{s}}^{-n} \cdot \tilde{P}_n(\boldsymbol{s})$ // cf. Equation (3.15)
  end
  // add artifact caused by this point object to the modeled reconstruction (see Equation (3.11))
  foreach $\boldsymbol{r}$ **do**
    $\mu_{\text{rec}}(\boldsymbol{r}) \leftarrow \mu_{\text{rec}}(\boldsymbol{r}) + \tilde{\chi}(\boldsymbol{r} - \boldsymbol{x})$
  end
end

enhancement of 250 HU and a blood volume fraction in cerebral tissue of 2% to 4% — this windowing is useful to estimate the areas where the artifact values have the same magnitude as the peaks of the tissue time-attenuation curves.

The results from the model (μ_{mdl}) and the simulation (μ_{sim}) show excellent agreement. The curves in the last row of Figure 3.5 have root mean square deviations of 1.1 HU ($t_{\text{rec}} = 2.25$ s), 0.3 HU ($t_{\text{rec}} = 4.50$ s) and 0.5 HU ($t_{\text{rec}} = 6.75$ s). From the results one can see that only a small number of DWPSFs of the model must be considered in order to predict the artifacts from typical perfusion time-attenuation curves. The small differences between model and simulation are primarily due to discretization effects.

3.4.3 Analysis of Reconstruction Parameters

The model can be used to systematically analyze the effect of different scan and reconstruction parameters on the artifacts from inconsistent data. Parameters that

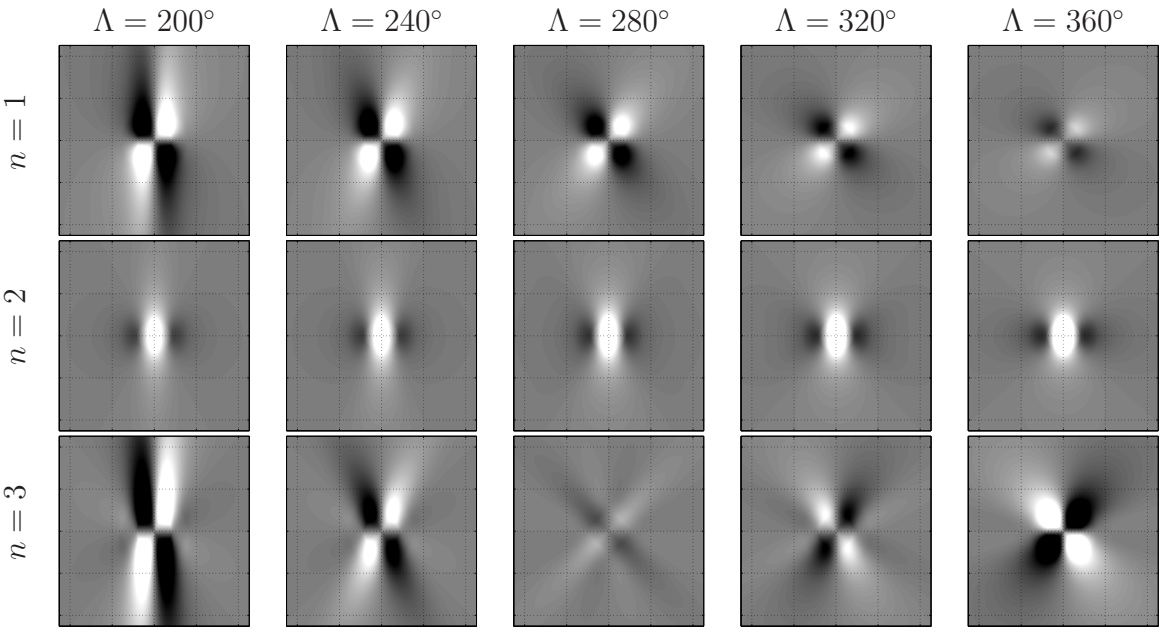

Figure 3.6: Derivative-weighted point spread functions P_n of the artifact model computed for different sliding window lengths Λ. The window center is 0 and the window widths are constant for each n (see Section 3.4.3 for details). The color map range is from black to white. The dotted grid has a spacing of 1 mm.

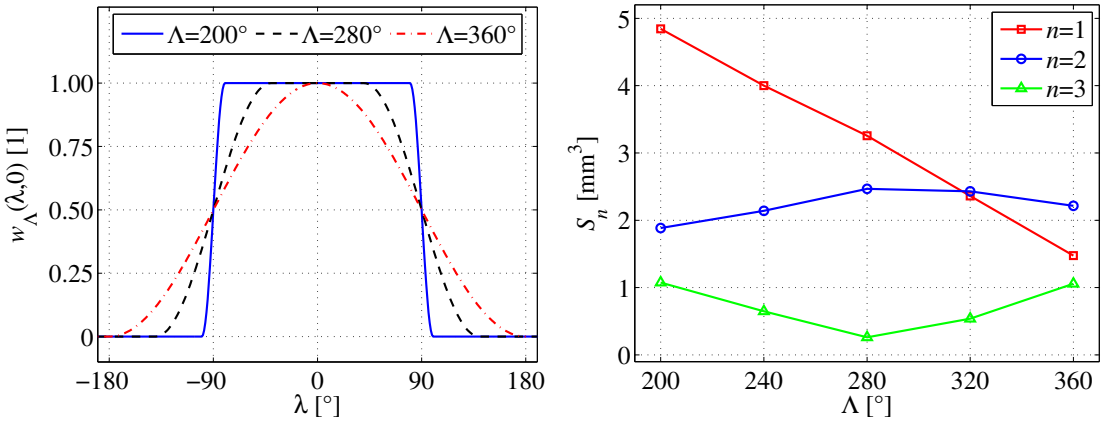

(a) sliding window function $w_\Lambda(\lambda, 0)$

(b) weighted spatial spread S_n of P_n

Figure 3.7: (a) Sliding windowing function $w_\Lambda(\lambda, 0)$ corresponding to the central ray for different Λ. (b) Weighted spatial spread S_n of P_n depending on Λ.

could be investigated include, for example, the filter kernel $h_{\text{ramp}}(u)$, the type of the redundancy weighting function $m_\Lambda(\lambda, \gamma)$ and the sliding window length Λ.

As an example, the DWPSFs computed for different sliding window lengths Λ are presented. The parameters from Table 3.1 are used, the value for N_{views} is changed and Λ is adapted accordingly. The windowing function $w_\Lambda(\lambda, 0)$ for different Λ is shown in Figure 3.7(a) and Figure 3.6 shows P_n $(n = 1, 2, 3)$ computed for different Λ. The window width is constant for each n for better comparison of the change due to different Λ. The window widths are set to the maximum absolute amplitude values Π_n computed for $\Lambda = 200°$ as shown in Figure 3.4.

For quantitative evaluation the weighted spatial spread S_n of P_n is introduced which is defined as

$$S_n(\boldsymbol{x}, \lambda_{\text{rec}}) = \iint |P_n(\boldsymbol{s}, \boldsymbol{x}, \lambda_{\text{rec}})| \; (s_x^2 + s_y^2)^{1/2} \, \mathrm{d}s_x \, \mathrm{d}s_y \; . \tag{3.30}$$

This heuristic definition takes into account both the absolute HU value of the artifact and its distance from the center of the point object and can be used for relative comparison of different Λ values. The absolute value of P_n is computed in order to avoid the possibility that positive and negative contributions of P_n cancel each other out. Because artifacts which propagate farther into the tissue area can have a more negative impact on the clinical interpretation of the perfusion maps a distance weighting has been included as well.

Figure 3.7(b) shows that increasing the sliding window length reduces S_1 from 4.84 mm^3 $(\Lambda = 200°)$ to 1.48 mm^3 $(\Lambda = 360°)$. Interestingly, S_3 increases from 0.26 mm^3 $(\Lambda = 280°)$ to 1.06 mm^3 $(\Lambda = 360°)$. The behavior of the functions P_n with respect to Λ and other reconstruction parameters could be explained by further investigation of Equation (3.17).

The artifact model can be used to optimize reconstruction parameters for the expected temporal variation of the attenuation values. The spatial spread of the linear component of the time-attenuation curve, defined by S_1, decreases by about 70% when using $\Lambda = 360°$ compared to $\Lambda = 200°$. Typically, one can find an approximately linear change of attenuation values inside an arterial vessel during the inflow phase.

Therefore, with respect to the spatial spread of the FBP artifacts the parameter value $\Lambda = 360°$ is more optimal than $\Lambda = 200°$ if the dynamic changes of the attenuation values are approximately piecewise linear. On the other hand, for temporal dynamics that are not expected to be piecewise linear, different Λ values may be more optimal. Note, a larger window length would not increase the total X-ray dose during the exam if continuously rotating C-arm CT systems could be used.

Higher Λ values lead to a lower temporal resolution of the reconstructed time-attenuation curves. Although the full width at half maximum (FWHM) is the same for all windows $w_\Lambda(\lambda, 0)$, see Figure 3.7(a), the full width at quarter maximum, for example, increases for higher Λ. Finally, it should be noted that there is a trade-off between the reduction of the spatial spread of the artifacts and the temporal resolution of the reconstructed time curves.

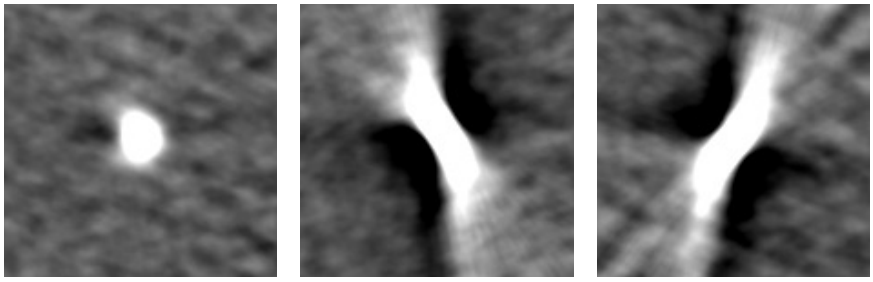

(a) reference (b) forward rotation (c) backward rotation

Figure 3.8: Reconstructions of a flow phantom: (a) reference reconstruction of data with constant attenuation values and (b-c) reconstructions of data acquired during a forward and backward C-arm rotation while the attenuation values inside the plastic tube were linearly increasing. The windowing is from –250 HU (black) to +250 HU (white).

3.5 Experimental Data from a Clinical C-arm CT

In this section, reconstruction results of a flow phantom will be presented. The phantom has time-varying attenuation values and was scanned using a clinical C-arm CT system.

3.5.1 Methods

In order to investigate reconstruction artifacts due to time-varying attenuation values under realistic conditions a simple flow phantom was built. A small plastic tube (inner diameter 2.0 mm) was placed into a water-filled container (volume of water about $22{\cdot}8{\cdot}25$ cm^3) that was placed on the patient table of a clinical C-arm CT system (Artis *d*TA with syngo DynaCT, Siemens AG, Healthcare Sector, Forchheim, Germany). The tube was connected to a double head contrast agent injector (Accutron HP-D, Medtron AG, Saarbrücken, Germany) that had the syringes filled with water and contrast agent (Oxilan 300, Guerbet Group, Villepinte, France), respectively. During injection into the tube (injection rate 10 ml/s) the mixing ratio of the two syringes was linearly changed from 0% to 50% contrast agent using an increase of 12.5% contrast agent per second.

A total of 191 projections was acquired with a view-angle increment of 1.0°, a detector pixel spacing of $0.616 \cdot 0.616$ mm^2 after $4 \cdot 4$ binning and a C-arm rotation time of 4.3 s. The phantom was scanned using a forward and a backward C-arm rotation and one 3-D volume was reconstructed for each rotation with the standard reconstruction filter kernel. For reference, the phantom filled with a constant amount (about 15%) of contrast agent was also scanned and reconstructed.

3.5.2 Results and Discussion

Figure 3.8 shows the reference reconstruction of the static phantom data and the two reconstructions of the dynamic phantom data from the forward and backward C-arm rotation, respectively. The axial images were reconstructed using $150 \cdot 150$

pixels with 0.1 mm pixel spacing. Thus, the side length of each image is 15 mm. The reconstructions show a similar pattern when compared with the reconstruction of the numerical phantom during the inflow or outflow phase (Figure 3.5, left and right columns) which also resulted from an approximately linear change of attenuation values during the data acquisition.

Using the artifact model, the reconstruction results in Figure 3.8(b)–(c) can be interpreted as the superposition of the weighted DWPSFs of zeroth (P_0) and first (P_1) order. It is assumed that second and higher order DWPSFs receive zero weights due to the approximately linear change of attenuation values. The different signs of the streaks in Figure 3.8(b)–(c), which are contributions of P_1, are well explained by the different directions of the C-arm rotation, i.e. different signs of ω_s. Note, the weight of P_0 is independent of ω_s, see Equation (3.15).

This experiment provides a qualitative evaluation and interpretation of the reconstruction artifacts of the flow phantom. A more detailed, quantitative analysis could be carried out in the future. For example, different angular sliding window lengths up to 360° could be investigated. With potential future C-arm CT systems that could perform continuous C-arm rotations this investigation would be of high interest in order to validate the predictions from the numerical example in Section 3.4.3.

3.6 Discussion and Summary

The aim of this chapter was to derive and interpret a model for FBP reconstruction artifacts due to time-varying attenuation values. The FBP algorithm was analyzed because it is computationally very fast and can be applied to reconstruct large-volume data sets in C-arm CT perfusion imaging during stroke treatment.

The novel spatio-temporal model describes the variation of attenuation values by their temporal derivative values. To model the spatial spread of the artifacts time-derivative-weighted point spread functions were introduced which are computed from the scan and reconstruction parameters. With this formalism the reconstruction artifacts can be separated into a component that depends on the dynamic process and a component that purely depends on system parameters. The model is optimized for contrast agent flow in perfusion imaging where the dynamic process can be approximated by a few temporal derivative values.

This model gives a detailed understanding of these FBP reconstruction artifacts. It can be used to predict the magnitude of artifacts for different temporal dynamics if the scan and reconstruction parameters are known. The model can also be applied to further investigate different reconstruction parameters in a systematic way. As an example, a comparison of different reconstruction sliding window lengths Λ has been conducted. It could be shown that the optimal value for Λ depends on the expected temporal dynamics of the attenuation values.

A limitation of the model is that artifacts due to sudden changes of the local attenuation values, caused for example by patient motion cannot be well described. These artifacts, which are most prominent at regions that have a high spatial gradient of attenuation values, can degrade the image quality in a similar manner as the artifacts due to contrast agent flow. In order to model these artifacts a higher number of DWPSFs would be required to consider more terms of the Taylor series, which

would, however, not be practical. Alternatively, if the artifact model was adapted such that it would use a parameterization of the time-attenuation curves which allows sudden changes of the attenuation values it may be possible to adequately describe these artifacts as well.

Noise in projection images was not considered in the artifact model. It can be treated by separating the noise from the signal and then making a normal FBP reconstruction of the noise. The artifact model is applied to the signal only. The final result of the model is the sum of the prediction from the noise-free signal and the reconstruction of the noise.

In this chapter, the model has been derived for the direct 2-D fan-beam FBP. To derive it for reconstruction algorithms that use 3-D cone-beam data, like the Feldkamp-Davis-Kress (FDK) algorithm [16], the equations in Section 3.2 must be extended to the 3-D geometry and the equations in Section 3.3 must be derived in a similar approach using this new geometry.

All terms in the artifact model are linear and this model could be written as a matrix equation if Equations (3.11), (3.15) and (3.17) were discretized and the derivatives were approximated by discrete derivative operators. Hence, a numerical inversion of this model could used to reduce the artifacts in the reconstructed images. Considering only those terms corresponding to $n = 1$ and $n = 2$ would make the inversion approach robust against noise while still including the most relevant terms.

To summarize, the novel model provides a comprehensive method to describe FBP artifacts from time-varying attenuation values in perfusion imaging. It is a mathematically exact analysis of the FBP reconstruction algorithm. This model can lead to enhanced reconstruction approaches in interventional perfusion imaging, such as sliding-window reconstruction approaches for continuously rotating C-arm CT systems, in order to optimize patient treatment during stroke therapy procedures.

Chapter 4

C-arm CT Perfusion Imaging Using Interleaved Scanning and Partial Reconstruction Interpolation

Overview:
In this chapter, a novel combined scanning and reconstruction approach for C-arm CT perfusion imaging is presented. This approach increases temporal sampling of the reconstructed data by using several interleaved scan sequences. It also provides a mean to reduce the reconstruction artifacts that are described in Chapter 3 by using an interpolation-based reconstruction technique. The approach is described in detail and it is evaluated using numerical simulations and *in vivo* data.

This chapter actually presents the main practical contribution of this thesis and it has several links to the previous chapters. The image analysis methods from Chapter 2 are applied to the simulated data and the *in vivo* data and the theoretical model from Chapter 3 is considered for explanations of the artifacts. The following chapters will also have links to this chapter. In Chapter 5, an injection protocol that is optimized for the interleaved scanning approach will be investigated. Furthermore, in Chapter 6.2 a software program will be described which processes data acquired using this approach.

This chapter is based on "Interventional 4-D C-arm CT perfusion imaging using interleaved scanning and partial reconstruction interpolation", by A. Fieselmann, A. Ganguly, Y. Deuerling-Zheng, M. Zellerhoff, C. Rohkohl, J. Boese, J. Hornegger, and R. Fahrig. *IEEE Transactions on Medical Imaging* (in press).

4.1 Introduction

In this section, first two major requirements for image reconstruction algorithms concerning perfusion imaging using C-arm CT will be presented. Then an overview of previous work in this field will be given.

4.1.1 Requirements Concerning Image Reconstruction

Image reconstruction algorithms concerning perfusion imaging in the interventional suite must fulfill certain clinical and technical requirements. Two major requirements that have been identified are described next.

1. **Short image reconstruction time:** Since time is a critical factor for the success of stroke treatment (Section 1.2.1) a short image reconstruction time is an important clinical requirement. Therefore, a computationally fast image reconstruction algorithm is needed to process the large-volume data sets which are acquired with C-arm CT. For example, reconstructing a volume with $512 \cdot 512 \cdot 200$ voxels at 40 different time points using 2 bytes for storing each voxel value will result in 4000 MB of reconstructed image data. In [126] it is estimated that about 10 minutes are the upper limit for the reconstruction time that is clinically acceptable for diagnostic flat-detector perfusion CT imaging in an acute stroke setting[3]. If perfusion imaging is used during the intervention, e.g. for monitoring the treatment success (Section 1.2.2), then even shorter reconstruction times are expected to be necessary.

2. **Reconstruction of tissue TACs which have a low CNR:** In perfusion (C-arm) CT imaging the TACs measured in tissue are generally characterized by a lower CNR when compared to TACs measured in arteries, for example (Figure 2.6). It is a technical requirement that an image reconstruction algorithm should not only process dynamic data with a high CNR correctly but it must also process the dynamic data with a low CNR correctly.

4.1.2 Previous Work

There exists some previous work that concerns image reconstruction for dynamic perfusion imaging using slowly rotating (C-arm) CT systems. This work can be classified and summarized as follows.

1. **Iterative model-based reconstruction:** An iterative model-based reconstruction algorithm is presented in [127]. The authors used a parameterization of the TACs based on Gaussian or gamma-variate basis functions. The model parameters were estimated in an iterative manner by using forward projection and backprojection operations. However, the high dimensionality of the proposed optimization leads to very long reconstruction times and therefore it is

[3]Note, in a typical ischemic stroke event, on average, 19 million neurons will die during these 10 minutes (Section 1.2.1) [5]. Therefore, the reconstruction time has a direct impact on the health of the patient: every minute of reconstruction time that can be saved will, on average, rescue 1.9 million neurons.

currently not possible to use this approach with real data during interventional stroke therapy (Section 4.1.1).

2. **Iterative limited-angle-based reconstruction:** In order to increase the temporal sampling frequency and the temporal resolution, a method is presented in [128] that uses a limited view-angle interval and a prior image for image reconstruction. However, since this is also an iterative reconstruction approach, longer reconstruction times — which would make this approach currently not applicable for use during interventional stroke treatment — when compared to an analytical approach are to be expected. Furthermore, it has not been investigated how this method would perform with realistic tissue TACs that have a low CNR (Section 4.1.1).

3. **Analytical interpolation-based reconstruction:** In [122] a method for perfusion imaging using a slower continuously rotating CT scanner based on a dynamic Feldkamp-type reconstruction algorithm has been presented. The actual motivation for this method was to reduce X-ray dose by operating the CT scanner at a slow rotation speed. Unknown projection data at certain time points is interpolated by using polynomial splines. To increase computational speed, it was suggested to perform the interpolation using partially backprojected volumes. Note, this algorithm is based on the Feldkamp algorithm [16] which can be implemented such that it is computationally very fast when using modern graphics hardware, for example [114]. However, this algorithm would require a continuous uni-directional C-arm rotation which is currently not possible (Section 1.3.1).

   A straightforward extension of this algorithm which works with data acquired using bi-directional C-arm rotations is presented in [129]. Instead of using polynomial splines it is suggested to interpolate the missing projection data individually for each view angle by least-squares curve fitting with Fourier basis functions. The interpolation accuracy is, however, limited by the low number of sample points that are acquired with one single bi-directional C-arm CT scanning sequence (e.g., 5 samples points distributed non-uniformly over a 30 s interval [129]).

Due to the limitations of the current approaches in terms of their practical applicability and performance, a novel approach will be presented in this chapter. In contrast to the previous work listed above, it will be evaluated using simulated data and *in vivo* data acquired using a real C-arm CT system.

4.2 Specialized Scanning Protocol and Reconstruction Method

In this section, first the technical challenges will be explained that have been identified when CT-perfusion-like imaging is to be implemented using C-arm CT. This explanation is more detailed than the previous explanation given in Section 1.3.2. Then two

approaches will be presented: a specialized scanning protocol and an interpolation-based 4-D reconstruction method, which are the technical solutions that have been developed as part of this thesis project.

4.2.1 Challenges in C-arm-CT-based Perfusion Imaging

This section starts with a description of 4-D imaging using C-arm CT. In order to obtain N_{rot} reconstructed 3-D volumes the C-arm has to be rotated N_{rot} times, each time through approximately 200°, in a bi-directional manner. Note, current C-arm CT systems are not capable of continuous, uni-directional C-arm rotations (Section 1.3.1). During each rotation 2-D projection data are acquired. The time period for one rotation (typically 3–5 s) will be denoted T_{rot}. A short waiting time T_{w} (typically 1 s) is required between two rotations. Figure 4.1(a)(top) shows the view angle $\lambda(t) \in [0, \Lambda]$ of such a multi-rotational scan sequence plotted against time t. A multi-rotational scan sequence is also used in cardiac C-arm CT with retrospective electrocardiogram (ECG)-gating, for example [17].

Low Temporal Sampling Frequency

In perfusion CT the sample period is typically 1 s but it may be increased to up to 3 s and similar diagnostic quality of the computed perfusion parameter maps may still be provided [130, 131]. However, in perfusion imaging with a C-arm CT the temporal sample period, given by $T_{\text{rot}} + T_{\text{w}}$, obtained with such a 4-D scan protocol, is typically longer than 3 s and may not be sufficient for adequate sampling of the reconstructed time-attenuation curve. The temporal sampling frequency is defined as the inverse value of the temporal sample period and, in this case, it is less than 1/3 reconstructed images per second. In particular, arterial time-attenuation curves, which are used for normalization of the perfusion values (Section 2.2), have relatively fast contrast agent dynamics and may be undersampled [131].

Inconsistent Projection Data

The acquired projection data is inconsistent due to the (intentional) time-varying contrast agent concentration in the region of interest during one C-arm rotation. *Two* kinds of FBP reconstruction artifacts will be described that can occur. In order to explain these artifacts one single point object with time-varying attenuation values will be considered that is approximated by a discrete voxel. Note, due to the linearity of the FBP the explanations can be easily generalized to an arbitrary number of voxels with time-varying attenuation values.

First, the reconstructed time-attenuation curve measured at this voxel position is not a sampled version of the true time-attenuation curve. In fact, the relatively long acquisition process leads to a low-pass filtering of the true curve. By investigation of the FBP algorithm it can be shown that this process can be approximated by a convolution of the true curve with a rectangular function of temporal width T_{rot} before it is sampled [122]. Due to the low-pass filtering the peak value of a reconstructed time-attenuation curve will be underestimated even if the sample time point, i.e. the

central time of the C-arm rotation, coincides with the time of the peak value of the curve.

Second, streak artifact in the reconstructed 3-D volumes can appear around the voxel with time-varying attenuation values. A detailed description of this kind of artifact is actually provided in Chapter 3. The magnitude of this kind of artifact depends on the slope of the time-attenuation curve during the C-arm rotation. Therefore, this artifact will be most prominent around arterial vessels in which the attenuation values change rapidly and thus the time-attenuation curve has a high slope.

4.2.2 Interleaved Scanning (IS)

In order to improve the low temporal sampling (Section 4.2.1) an interleaved scanning protocol with N_{seq} different multi-rotational sequences is proposed. Each of the N_{seq} multi-rotational sequences consists of N_{rot} C-arm rotations, each of which provides a full set of projection data. In total $N_{\text{seq}} \cdot N_{\text{rot}}$ datasets are acquired. The interleaved scanning protocol has two important features. First, a new bolus with identical injection parameters will be injected before each multi-rotational sequence. Second, for each multi-rotational sequence there will be a different delay time between the start of the bolus injection and the start of the scanning.

This interleaved scanning approach increases the sampling density of the projection data space and consequently the sampling density of the reconstructed time-attenuation curves extracted from each voxel. Figure 4.1(b) shows an example with two multi-rotational sequences.

One can determine the temporal delay τ_n between the start of the injection and start of the n-th multi-rotational sequence ($n = 0, \ldots, N_{\text{seq}} - 1$) by

$$\tau_n = (T_{\text{rot}} + T_{\text{w}}) \cdot \frac{n}{N_{\text{seq}}} + t_{\text{c}} \tag{4.1}$$

where t_{c} is a constant temporal offset. This definition of τ_n leads to a regular sampling of the central view angle $\Lambda/2$. Other definitions of τ_n with non-uniform sampling periods are also possible. For $t_{\text{c}} \leq -T_{\text{rot}}$ one or several baseline volumes without contrast agent are acquired before the acquisition of the contrast-agent-enhanced volumes. In perfusion imaging at least one baseline volume is needed which will then be subtracted from the following contrast-agent-enhanced volumes (Section 2.4.4). Thus, a practical choice would be $t_{\text{c}} = -T_{\text{rot}}$.

A method that is similar to this interleaved scanning approach was recently applied to lung perfusion imaging in rodents using a micro-CT [132]. The authors used several consecutive small volume injections of iodinated contrast agent, performed at a series of different starting view angles, in order to increase the temporal sampling density.

4.2.3 Partial Reconstruction Interpolation (PRI)

With interleaved scanning as described in Section 4.2.2 the temporal sampling density of the perfusion time-attenuation curves can be increased. Nevertheless, the projection data for each reconstructed 3-D volume is acquired over a time interval

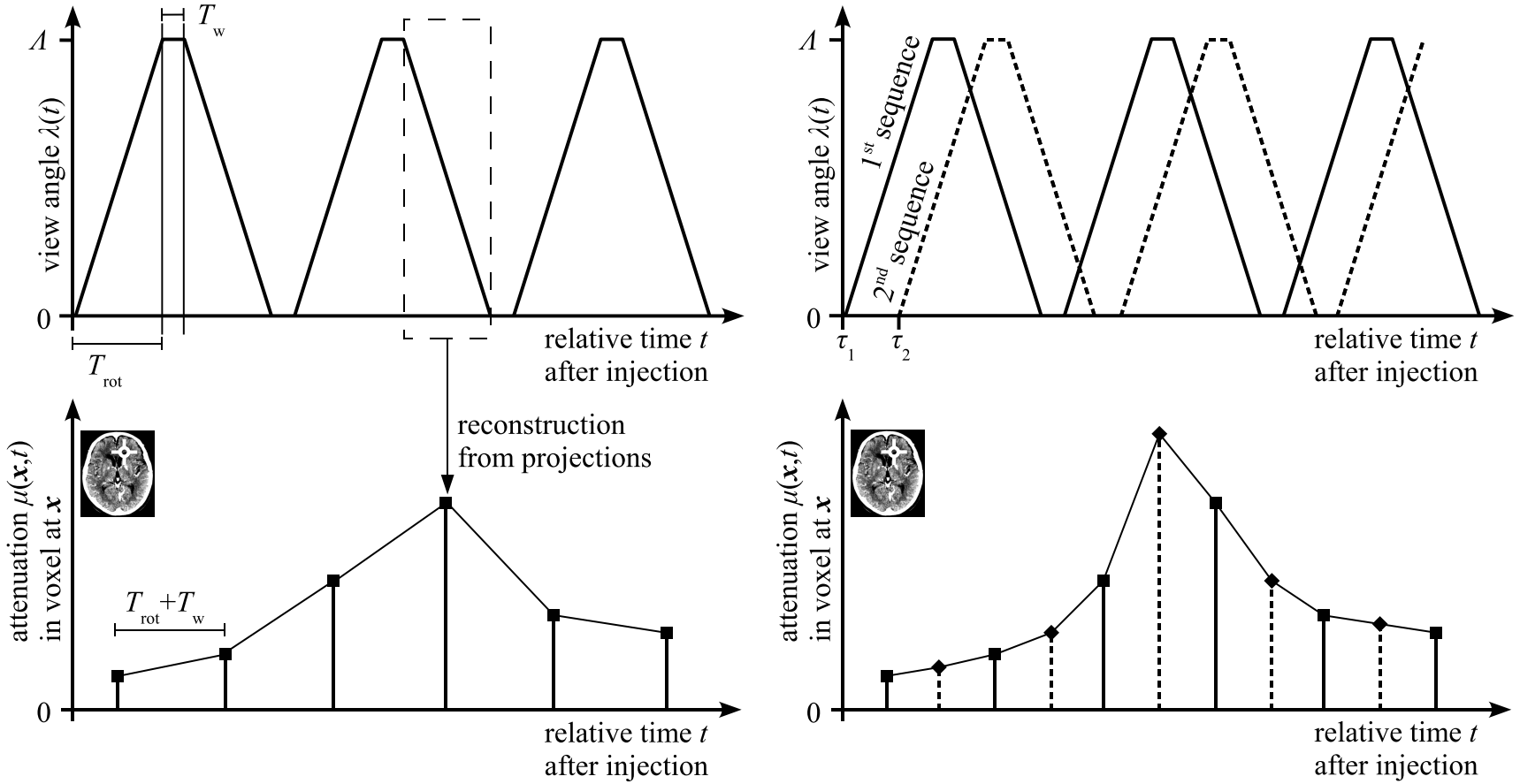

(a) one scan sequence ($N_{\text{seq}} = 1$)

(b) two interleaved scan sequences ($N_{\text{seq}} = 2$)

Figure 4.1: The X-ray source of the C-arm CT system rotates in a bi-directional manner (top row). One volume is reconstructed from the data of each rotation and for each voxel a time series can be measured (bottom row). The right figure shows the principle of interleaved scanning where the two sequences have different delay times τ_1 and τ_2 relative to the time of injection.

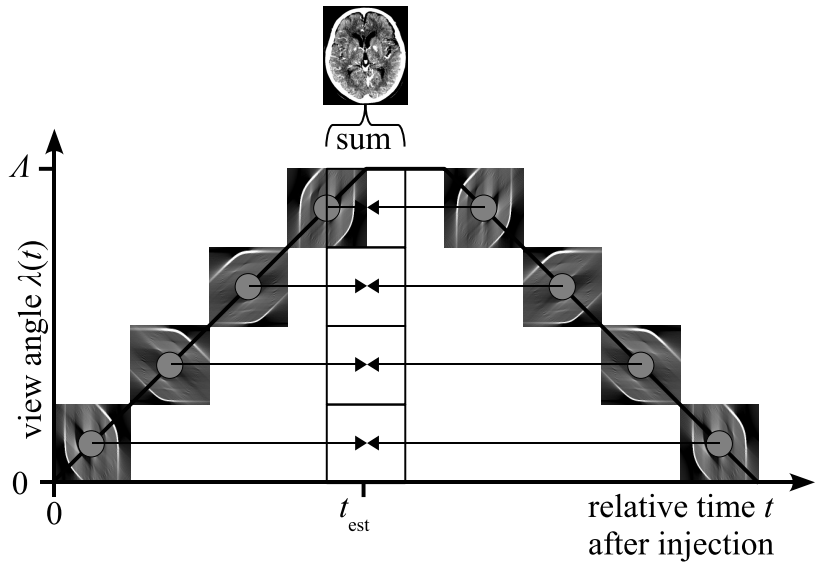

(a) one scan sequence ($N_{\text{seq}} = 1$)

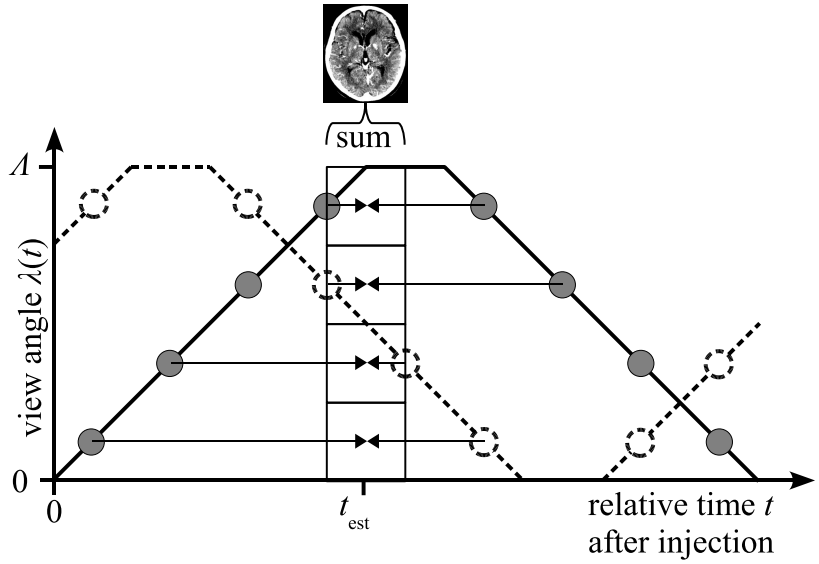

(b) two interleaved scan sequences ($N_{\text{seq}} = 2$)

Figure 4.2: Partial reconstruction interpolation with $M = 4$ angular interpolation intervals to create a reconstructed volume at $t = t_{\text{est}}$. In (b) the data from two interleaved scans is actually combined to yield better interpolation results.

T_{rot}. In order to compensate for the inconsistent projection data, and to reduce the two kinds of artifacts that were described in Section 4.2.1, an interpolation-based 4-D reconstruction approach is proposed. It is motivated by a method that was previously investigated using a slowly rotating CT scanner (Section 4.1.2) [122]. This method has been adapted to the C-arm CT scanning approach which, in contrast to the method in [122], uses several interleaved sequences each having alternating directions of C-arm rotations. In order to describe this reconstruction approach, at first only one multi-rotational scan sequence, i.e. $N_{\text{seq}} = 1$, will be considered. Thereafter, the case with multiple scan sequences will be described.

During one C-arm rotation there are N_{views} different view angles, starting at λ_0, with angular intervals $\Delta\lambda$. For each individual view angle λ_l,

$$\lambda_l = \lambda_0 + l \cdot \Delta\lambda \quad (l = 0, \ldots, N_{\text{views}} - 1) \,, \tag{4.2}$$

a discrete sequence of cone-beam projections $p_{l,k}(u, v)$ is acquired, where u and v are the usual coordinates on the flat-panel detector, at time points $t_{l,k}$ $(0 \leq k \leq N_{\text{rot}} - 1)$ that refer to the time when the projection under the angle λ_l was acquired during the k-th rotation.

In order to estimate an unknown projection value $\tilde{p}_{l,t_{\text{est}}}(u, v)$ at a certain time point t_{est} with $t_{l,0} \leq t_{\text{est}} \leq t_{l,N_{\text{rot}}-1}$ one can apply temporal interpolation using the known projection values:

$$\tilde{p}_{l,t_{\text{est}}}(u, v) = \sum_{k=0}^{N_{\text{rot}}-1} p_{l,k}(u, v)\, \varphi_{l,k}\left(t_{\text{est}} - t_{l,k}\right) \,. \tag{4.3}$$

Possible interpolation functions $\varphi_{l,k} : \mathbb{R} \mapsto \mathbb{R}$ for non-uniformly sampled projection data, caused by the alternating directions of C-arm rotations, will be discussed in Section 4.2.4. In order to approximate a consistent data set this interpolation can be applied to estimate projections for all necessary combinations of l, u and v at a certain time point t_{est}.

However, during C-arm CT scanning the projections may not be acquired at exactly the same angular position in forward and backward rotations due to limited accuracy of the mechanical C-arm motion. This would negatively impact the projection-based interpolation. To take this into account and to increase the computational speed, the interpolation can also be applied using partially backprojected volumes. In order to describe this concept the projection data of the k-th C-arm rotation will be denoted as

$$\begin{aligned} \mathcal{P}_k = \{&p_{0,k}(u_{\min}, v_{\min}), \ldots, p_{0,k}(u_{\max}, v_{\max}), \ldots, \\ &p_{N_{\text{views}}-1,k}(u_{\min}, v_{\min}), \ldots, p_{N_{\text{views}}-1,k}(u_{\max}, v_{\max})\} \end{aligned} \tag{4.4}$$

where the subscripts min and max indicate the minimum and maximum detector coordinate, respectively.

The operator $\text{PFBP}_{l_1}^{l_2}(\boldsymbol{x})\,\{\mathcal{P}_k\}$ for partial filtered backprojection is introduced in order to partially reconstruct an attenuation value at position $\boldsymbol{x}$ using only the projections from $\mathcal{P}_k$ with $l \in [l_1, l_2]$. This operator includes all steps of a normal FBP reconstruction including the fan-beam redundancy weighting, for example, but backprojects the data over a limited angular interval only.

The PFBP operator can be implemented using a Feldkamp-type algorithm [16] as

$$\mathrm{PFBP}_{l_1}^{l_2}(\boldsymbol{x})\,\{\mathcal{P}_k\} = \sum_{l=l_1}^{l_2} \frac{m_\Lambda(\lambda_l, u^*_{\lambda_l}(\boldsymbol{x}))}{\hat{w}_{\lambda_l}(\boldsymbol{x})^2} \cdot \hat{p}_{l,k}(u^*_{\lambda_l}(\boldsymbol{x}), v^*_{\lambda_l}(\boldsymbol{x}))\ . \tag{4.5}$$

Here, the functions $u^*_{\lambda_l}(\boldsymbol{x})$ and $v^*_{\lambda_l}(\boldsymbol{x})$ give the detector coordinates where a beam from the view angle λ_l passing through $\boldsymbol{x}$ intersects the detector, $m_\Lambda(\lambda_l, u)$ is a fan-beam redundancy weighting function [123] (cf. Equation (3.9) where it is defined for γ instead of u) and $\hat{w}_{\lambda_l}(\boldsymbol{x})$ is a distance weighting function, see [114] for details. The function $\hat{p}_{l,k}(u, v)$ is a bi-linear interpolation of the pre-processed (e.g., ramp-filtered) projection $p_{l,k}(u, v)$.

Illustrations for these partial backprojections are shown in Figure 4.2(a). An important property of the PFBP operator is that a normal reconstruction of the value $\mu_{\mathrm{rec}}(\boldsymbol{x}, k)$ at $\boldsymbol{x}$ during the k-th C-arm rotation, here assuming a time-independent object, is given by the sum of all partial filtered backprojections, i.e.

$$\mu_{\mathrm{rec}}(\boldsymbol{x}, k) = \sum_{j=0}^{M-1} \mathrm{PFBP}_{jL}^{(j+1)L-1}(\boldsymbol{x})\,\{\mathcal{P}_k\}\ , \tag{4.6}$$

where $L = N_{\mathrm{views}}/M$ and M is the number of angular interpolation intervals. In general, the number L of view angles per partial backprojection could also be non-uniform and angular windowing functions could be applied. For simplicity, it is assumed that L is an integer value. Note, the partial reconstruction interpolation approach is generic and can also be based on reconstruction algorithms other than the FDK algorithm as long as these algorithms fulfill the condition in Equation (4.6).

One can now apply the interpolation to the partial backprojections in order to reconstruct a value $\tilde{\mu}_{\mathrm{rec}}(\boldsymbol{x}, t_{\mathrm{est}})$ corresponding to the time point t_{est}:

$$\begin{aligned}\tilde{\mu}_{\mathrm{rec}}(\boldsymbol{x}, t_{\mathrm{est}}) = \sum_{j=0}^{M-1} \sum_{k=0}^{N_{\mathrm{rot}}-1} & \mathrm{PFBP}_{jL}^{(j+1)L-1}(\boldsymbol{x})\,\{\mathcal{P}_k\} \\ & \cdot\ \varphi_{(j+0.5)L,k}\left(t_{\mathrm{est}} - t_{(j+0.5)L,k}\right)\ .\end{aligned} \tag{4.7}$$

Next, the use of this approach with data from an interleaved scanning protocol, i.e. $N_{\mathrm{rot}} \geq 2$, will be described. In order to optimize the accuracy of the interpolation the data from different multi-rotational sequences can be combined. Mathematically, one changes the summation endpoint of the inner sum in Equation (4.7) from $N_{\mathrm{rot}} - 1$ to $N_{\mathrm{rot}} \cdot N_{\mathrm{seq}} - 1$ and interprets k as an index that can refer to C-arm rotations from different multi-rotational sequences. This combined interleaved scanning (IS) and partial reconstruction interpolation (PRI) approach is also illustrated in Figure 4.2(b) and summarized in Algorithm 4.1. The combination of both methods (IS-PRI) increases the temporal sampling density and can yield better approximations for consistent projection data sets.

In the IS-PRI approach the change of contrast agent concentration in an projection interval with L view angles is assumed to be negligible. Furthermore, the contrast-agent-induced temporal enhancement function is assumed to be sufficiently smooth between two data time points in order to obtain accurate interpolation results.

Algorithm 4.1: Algorithm for partial reconstruction interpolation with interleaved scanning data.

Input: projection data of $N_{\text{seq}} \cdot N_{\text{rot}}$ C-arm rotations,
number M of angular interpolation intervals,
interpolation time points $t_{\text{est},i}$ $(i = 0, \ldots, N_{\text{tp}} - 1)$

Output: reconstructed data $\tilde{\mu}_{\text{rec}}$

```
// step 1: generation of PFBP data
for q2 = 0 to N_seq − 1 do
    for q1 = 0 to N_rot − 1 do
        k ← q1 + q2 · N_rot
        let P_k denote the set of projetion data of the q1-th C-arm rotation
        in the q2-th interleaved sequence (cf. Equation (4.4))
        for j = 0 to M − 1 do
            compute X(j, x, k) ≡ PFBP_{jL}^{(j+1)L−1}(x) {P_k} according to
            Equation (4.5) for all (pre-defined) voxel positions x and store
            this data to the memory or file system
        end
    end
end
// step 2: interpolation of PFBP data
foreach voxel position x do
    μ̃_rec(x, t_est,i) ← 0   ∀ i
    for j = 0 to M − 1 do
        X̂(k) ≡ X(j, x, k) // intermediate variable
        sort X̂(k) such that the corresponding acquisition time points
        t_{(j+0.5)L,k} are in ascending temporal order
        for i = 0 to N_tp − 1 do
            μ̃_rec(x, t_est,i) ← μ̃_rec(x, t_est,i) + interpolated value of X̂(k) at t_est,i
        end
    end
end
```

4.2.4 Interpolation of Non-uniformly Sampled Data

Due to the alternating directions of C-arm rotations the projection data is sampled using non-uniform time intervals. This has to be considered when choosing suitable interpolation functions $\varphi_{l,k}$ in Equation (4.7). There are various interpolation methods for non-uniformly sampled data and an overview of 5 different methods will be provided next.

Nearest neighbor (NN) and linear (LIN) interpolation are robust against noisy data and they preserve the monotonicity of the data that is being interpolated. I.e. the interpolated values between two adjacent sample points are either strictly increasing or strictly decreasing. Cubic spline (CS) interpolation generates smooth curves which can be non-monotonic but it can lead to unintended overshoots or undershoots when interpolating noisy data [62]. Another class of interpolation methods are piecewise cubic Hermite interpolating polynomials (HIP) [133]. They also preserve the monotonicity of the data but they generate smoother curves when compared to linear interpolation. Radial basis function (RBF) interpolation computes an interpolated value by using a distance-dependent weighting of the known sample values [134]. For example, in [17] a Gaussian function has been used as weighting function.

4.2.5 Complexity Analysis

In this section, the computational complexity of the IS-PRI algorithm is investigated. This algorithm is composed of two main steps, cf. Algorithm 4.1. The first step consists of the generation of the PFBP data (Equation (4.5)). The second step involves the interpolation of this data in order to obtain the time-attenuation curves (Equation (4.7)).

The PFBP data is generated using the FDK algorithm [16]. The backprojection step, which represents the most time-consuming part of this algorithm, has a complexity of $\mathcal{O}(N_{\text{views}}\, n^3)$, cf. [135], where n denotes the side length of the reconstructed volume and N_{views} denotes the number of projections used for the reconstruction of one volume.

The complexity of the PFBP generation is independent of the number M of angular interpolation intervals. However, the memory that is required to store the PFBP data scales linearly with M. The computational complexity to generate the PFBP data from all $N_{\text{seq}} \cdot N_{\text{rot}}$ C-arm rotations is therefore

$$\mathcal{O}(N_{\text{seq}}\, N_{\text{rot}}\, N_{\text{views}}\, n^3)\ . \tag{4.8}$$

Before the interpolation can be performed the data from the interleaved scanning protocol must be arranged in ascending temporal order. The sorting has to be done for all M angular intervals individually and the typical complexity of each sorting step is $\mathcal{O}(N_{\text{seq}}\, N_{\text{rot}}\, \log(N_{\text{seq}}\, N_{\text{rot}}))$.

The interpolation is conducted for the time series at each voxel position and at each angular interpolation interval; thus, a number of $M \cdot n^3$ time series to be interpolated exist. Therefore, the interpolation step has a complexity of

$$\mathcal{O}(M\, N_{\text{tp}}\, n^3) \tag{4.9}$$

Parameter	Symbol	Value, set 1 (simulations)	Value, set 2 (*in vivo* study)
view-angle increment	$\Delta\lambda$	0.5°	1°
number of views per rotation	N_{views}	401	191
angular range per rotation	Λ	200°	190°
time per rotation	T_{rot}	4.30 s	4.30 s
time between rotations	T_{w}	1.25 s	1.25 s
number of rotations	N_{rot}	9	6
total scanning time	—	48.7 s	32.05 s
source-to-isocenter distance	R	800 mm	785 mm
source-to-detector distance	D	1200 mm	1198 mm
area of quadratic detector pixel	$(\Delta u)^2$	$0.6 \cdot 0.6$ mm^2	$0.616 \cdot 0.616$ mm^2
number of detector pixels	N_{detpix}	$800 \cdot 1$ (no binning)	$616 \cdot 480$ (after $4 \cdot 4$ binning)
total detector size	—	$480 \cdot 0.6$ mm^2	$\approx 380 \cdot 296$ mm^2

Table 4.1: Scan parameters for the numerical simulations and the *in vivo* study. The angular range per rotation is computed as $\Lambda = (N_{\text{views}} - 1) \cdot \Delta\lambda$. The total scanning time is computed as $N_{\text{rot}} \cdot T_{\text{rot}} + (N_{\text{rot}} - 1) \cdot T_{\text{w}}$. The total detector size is computed as $N_{\text{detpix}} \cdot (\Delta u)^2$.

where N_{tp} is the number of interpolation time points. Assuming that

$$M\, N_{\text{tp}} \leq N_{\text{seq}}\, N_{\text{rot}}\, N_{\text{views}}\ , \tag{4.10}$$

the complexity of the complete algorithm is finally given by

$$\mathcal{O}(N_{\text{seq}}\, N_{\text{rot}}\, N_{\text{views}}\, n^3)\ . \tag{4.11}$$

Thus, the interpolation step can be neglected in this asymptotic analysis and the computational complexity of the whole IS-PRI algorithm is approximately that of individual FDK reconstructions of each C-arm rotation. A similar result was obtained for the interpolation-based algorithm that is presented in [136], which is designed for a continuously rotating CT scanner without interleaved scanning.

4.3 Numerical Simulations

In this section, numerical simulations were performed to investigate the properties of the acquisition and reconstruction scheme described in Section 4.2.

4.3.1 Phantom Description

Three different time-attenuation curves were generated to model the flow of contrast agent through a large artery, a region of normally-perfused tissue and a region

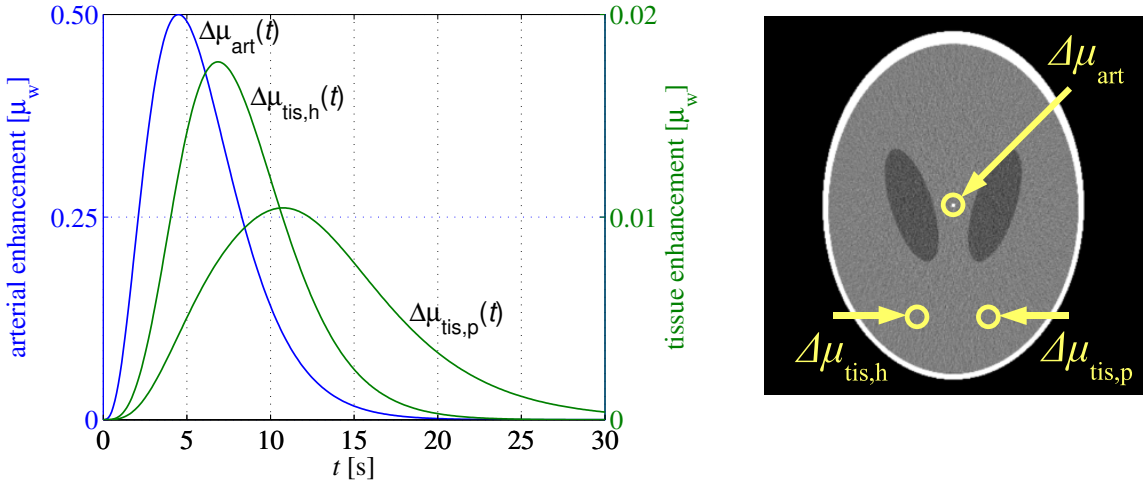

(a) time-attenuation curves (b) dynamic head phantom

Figure 4.3: (a) Synthetic time-attenuation curves, here without noise, corresponding to a large artery ($\Delta\mu_{\mathrm{art}}(t)$, left scale), to healthy, normally-perfused tissue ($\Delta\mu_{\mathrm{tis,h}}(t)$, right scale) and to pathological, hypoperfused tissue ($\Delta\mu_{\mathrm{tis,p}}(t)$, right scale). The plots show the dynamic enhancement (above the static baseline value) relative to the attenuation μ_{w} of water. (b) Locations of the artery and the tissue regions in the dynamic head phantom.

of hypoperfused tissue. The arterial enhancement $\Delta\mu_{\mathrm{art}}(t)$ was modeled using the following gamma-variate function (cf. Section 3.4.1) [57]:

$$\Delta\mu_{\mathrm{art}}(t) = \frac{A}{(\alpha\,\beta\,\exp(-1))^{\alpha}}\,\hat{\tau}^{\alpha}\,\exp(-\hat{\tau}/\beta)\,H(\hat{\tau})\;. \tag{4.12}$$

Here, $H(\hat{\tau})$ is the unit step function, $A = 0.5\,\mu_{\mathrm{w}}$ is the maximum dynamic enhancement (above the static baseline value), $\mu_{\mathrm{w}} = 0.18\,\mathrm{cm}^{-1}$ is the X-ray attenuation of water and $\alpha = 3.0$ and $\beta = 1.5$ are shape parameters that were also suggested in [57]. The dimensionless quantity $\hat{\tau} = (t - t_0)/\eta$ depends on the bolus arrival time t_0 and the time scaling factor η which are both measured in s. The factor η controls the FWHM of the curve. The initial values were $t_0 = 0$ and $\eta = 1$ but as will be explained in Section 4.3.2 in more detail these values were varied to obtain several different curves.

Using these parameter values, arterial time curves were generated that were representative of the curves that were actually measured in the *in vivo* perfusion studies (Section 4.4). Note, in the studies a bolus injection at the aortic arch was used which resulted in a higher enhancement A when compared to a conventional intravenous bolus injection into the antecubital vein which is typically $0.25 - 0.30\,\mu_{\mathrm{w}}$. The

time-attenuation curves $\Delta\mu_{\text{tis}}(t)$ in tissue were computed using the indicator-dilution theory (cf. Equation (2.15)),

$$\Delta\mu_{\text{tis}}(t) = \text{CBF}\ \rho_{\text{voi}} \int_0^t \Delta\mu_{\text{art}}(\tau)\, r(t-\tau)\, \mathrm{d}\tau \tag{4.13}$$

$$r(t) = \begin{cases} 1, & \text{for } t < T_0 \\ \exp\left(\frac{-(t-T_0)}{\text{MTT}-T_0}\right), & \text{for } t \geq T_0\ , \end{cases} \tag{4.14}$$

with $\rho_{\text{voi}} = 1.04\,\text{g/ml}$. The shape of the residue function $r(t)$ and the value $T_0 = 0.632 \cdot \text{MTT}$ were chosen as suggested in [137]. According to Equation (2.25), MTT can be computed as

$$\text{MTT} = \text{CBV}/\text{CBF}\ . \tag{4.15}$$

The values CBF = 60 ml/100g/min and CBV = 4 ml/100g were chosen to generate a time-attenuation curve $\Delta\mu_{\text{tis,h}}(t)$ for healthy, normally-perfused tissue and CBF = 20 ml/100g/min and CBV = 4 ml/100g were chosen to generate a time-attenuation curve $\Delta\mu_{\text{tis,p}}(t)$ for pathological, hypoperfused tissue. A plot of all three time-attenuation curves is shown in Figure 4.3(a).

A dynamic Shepp-Logan-type head phantom [138] $\mu_{\text{pha}}(\boldsymbol{x}, t)$ was created that contained three circular regions of interest (ROI) with varying attenuation values, see Figure 4.3(b). The first ROI (radius 1 mm) modeled an artery with attenuation values $\mu_{\text{w}} + \Delta\mu_{\text{art}}(t)$. The second and third ROIs (radius 2 mm each) modeled tissue regions with attenuation values $\mu_{\text{w}} + \Delta\mu_{\text{tis,h}}(t)$ and $\mu_{\text{w}} + \Delta\mu_{\text{tis,p}}(t)$, respectively.

The constant attenuation values of the elliptical skull (outer radii 62 mm and 92 mm) and the brain tissue were $2\,\mu_{\text{w}}$ and μ_{w}, respectively. The constant attenuation values of the two inner ellipses were chosen to be $0.95\,\mu_{\text{w}}$. In order to improve the reproducibility of the results, a more detailed description of this phantom along with relevant source code is available online [139].

4.3.2 Investigations

C-arm CT scanning of the 2-D phantom was simulated with a linear detector array using the scan parameters from set 1 in Table 4.1. Poisson-distributed noise was added to the projection values of $\mu_{\text{pha}}(\boldsymbol{x}, t)$ assuming an emitted X-ray flux density of $2.1 \cdot 10^6$ photons per mm^2 at the source-to-detector distance as in [127].

Different numbers $N_{\text{seq}} \in \{1, 2, 3, 4\}$ of scan sequences and different numbers $M = \{1, 2, 3, 4, 5, 6, 12, 18\}$ of angular interpolation intervals were used. The five interpolation functions from Section 4.2.4 were applied and the interpolation time step was set to 0.5 s. These 160 different combinations of IS-PRI parameters were used to simulate scanning of the phantom $\mu_{\text{pha}}(\boldsymbol{x}, t)$. For each instance the scanning was repeated ten times each time having a different noise realization and different values for t_0 and η. These values were uniformly distributed in the intervals $t_0 \in [0,\ (T_{\text{rot}} + T_{\text{w}})[$ and $\eta \in [0.85,\ 1.15]$, respectively. This was done in order to take into account variations due to different, relative shifts between start of the scanning and the bolus arrival and also variations due to different shapes of the curves. The thickness of the reconstructed slices was 9.6 mm which is a typical value for neuro perfusion CT data. The reconstruction of thick slices was realized by averaging 16

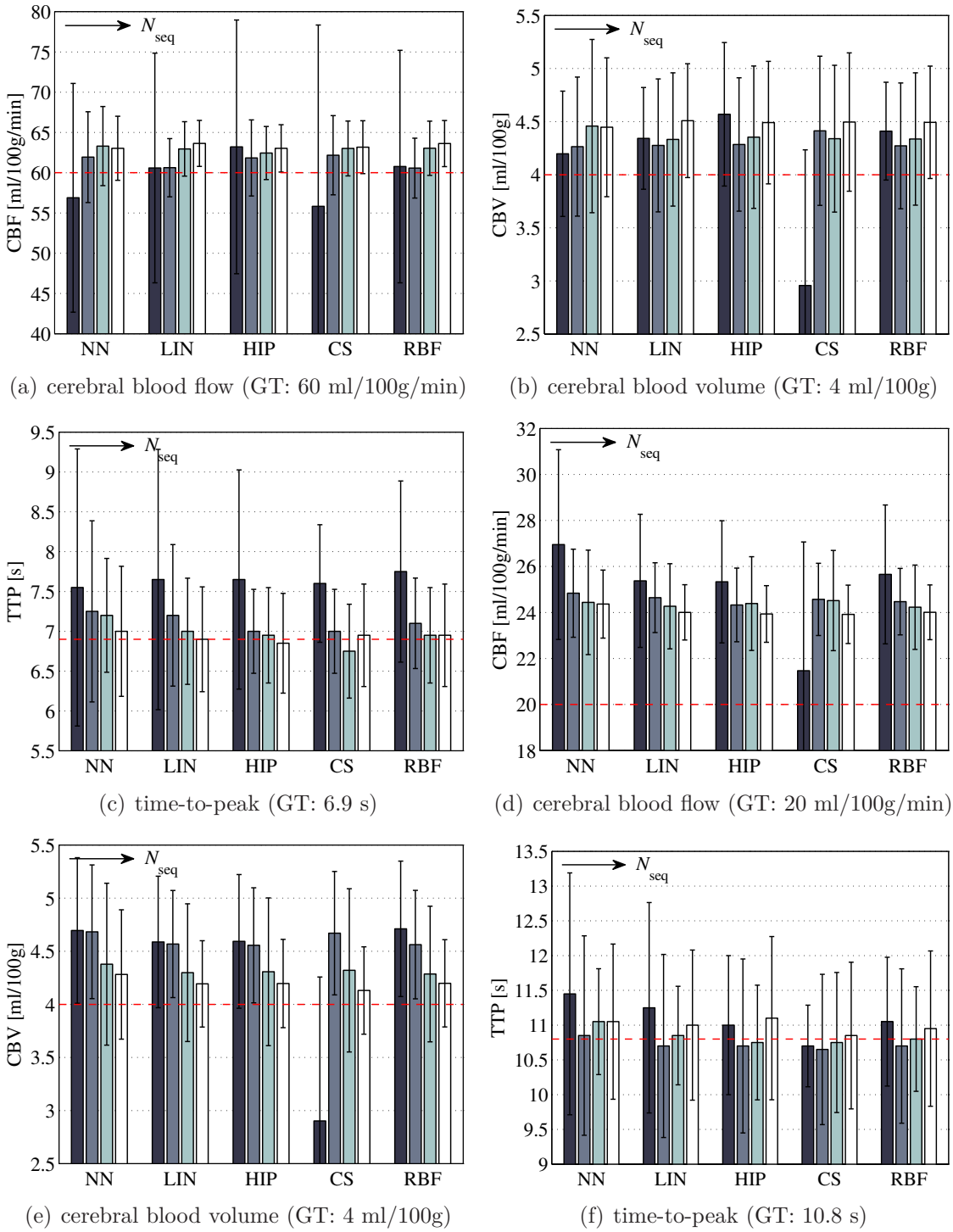

(a) cerebral blood flow (GT: 60 ml/100g/min)

(b) cerebral blood volume (GT: 4 ml/100g)

(c) time-to-peak (GT: 6.9 s)

(d) cerebral blood flow (GT: 20 ml/100g/min)

(e) cerebral blood volume (GT: 4 ml/100g)

(f) time-to-peak (GT: 10.8 s)

Figure 4.4: Simulation with noisy, synthetic data corresponding to (a–c) healthy and (d–f) pathological tissue. The graphs show mean and standard deviation of different measures with known ground truth (GT; dashed line) for different interpolation methods (abbreviations explained in Section 4.2.4) and numbers $N_{\text{seq}} \in \{1, 2, 3, 4\}$ of interleaved sequences. The different colors of the bars correspond to values from $N_{\text{seq}} = 1$ (dark) to $N_{\text{seq}} = 4$ (bright).

noisy projections, i.e. the slice thickness divided by the detector pixel size, for each view angle. The in-plane voxel spacing was 0.2 mm.

In order to analyze the reconstructed data, the focus was put on the following two aspects. First, the accuracy of measured perfusion values (CBF, CBV, MTT, TTP) was investigated for the healthy and pathological tissue. Second, the reconstruction artifacts due to inconsistent data around the simulated artery were investigated, cf. Section 4.2.1.

The perfusion parameters CBF, CBV and MTT were computed using the TSVD algorithm (Algorithm 2.1) with a fixed threshold value of 20% of the maximum singular value. Recall that in this algorithm the arterial time curve $\mu_{\text{art}}(t)$ and the tissue time curve μ_{tis} are deconvolved and the peak value and the integral of this deconvolved function give the CBF and the CBV, respectively, whereas MTT is the ratio of both (Equation (4.15)). TTP was determined directly from the tissue time curves.

The reconstruction artifact around the artery was quantified by measuring the average absolute deviation from the ground truth value in an annular region around the artery. The following expression defines the pixel positions $\boldsymbol{x}_i$ $(i = 0, \ldots, N_{\text{i}} - 1)$ that lie within this annular region:

$$r_{\text{art}}^2 \leq x_i^2 + y_i^2 \leq (3\, r_{\text{art}})^2 \ . \tag{4.16}$$

The outer radius was set to $3\, r_{\text{art}}$ after initial evaluation of different radii in order to have the majority of the artifact within the annulus ring. The measure $\bar{\chi}_{\text{art}}$ of the mean reconstruction artifact for a given time point t_{est} is defined as

$$\bar{\chi}_{\text{art}}(t_{\text{est}}) = \frac{1}{N_{\text{i}}} \sum_{i=0}^{N_{\text{i}}-1} \left| \tilde{\mu}_{\text{rec}}\left(\boldsymbol{x}_i, t_{\text{est}}\right) - \mu_{\text{pha}}\left(\boldsymbol{x}_i, t_{\text{est}}\right) \right| \ . \tag{4.17}$$

4.3.3 Results

Figure 4.4 shows the mean and standard deviation of the computed perfusion parameters CBF, CBV and TTP from reconstructions with a constant number $M = 6$ of angular interpolation intervals and different interpolation methods. Results with different numbers M will be discussed later. According to the central volume theorem, see Equation (4.15), only two of the three parameters CBF, CBV and MTT are independent and, for brevity, the MTT plots which show similar qualitative results as the CBF and CBV plots were omitted.

Generally, the standard deviation of the computed parameter values, which is a measure for the variability, decreases when the number N_{seq} of interleaved sequences increases. Especially the standard deviation of CBF and TTP (healthy tissue) decreases significantly when N_{seq} is increased from 1 to 2. For example, with linear interpolation the standard deviation of CBF in healthy tissue decreases from 14.3 ml/100g/min to 3.6 ml/100g/min when two interleaved sequences instead of one sequence are used. For pathological tissue these values are 2.9 ml/100g/min and 1.5 ml/100g/min.

The mean TTP values get closer to the ground truth value for increasing N_{seq} and the mean CBF and mean CBV values tend to get overestimated, especially for pathological tissue.

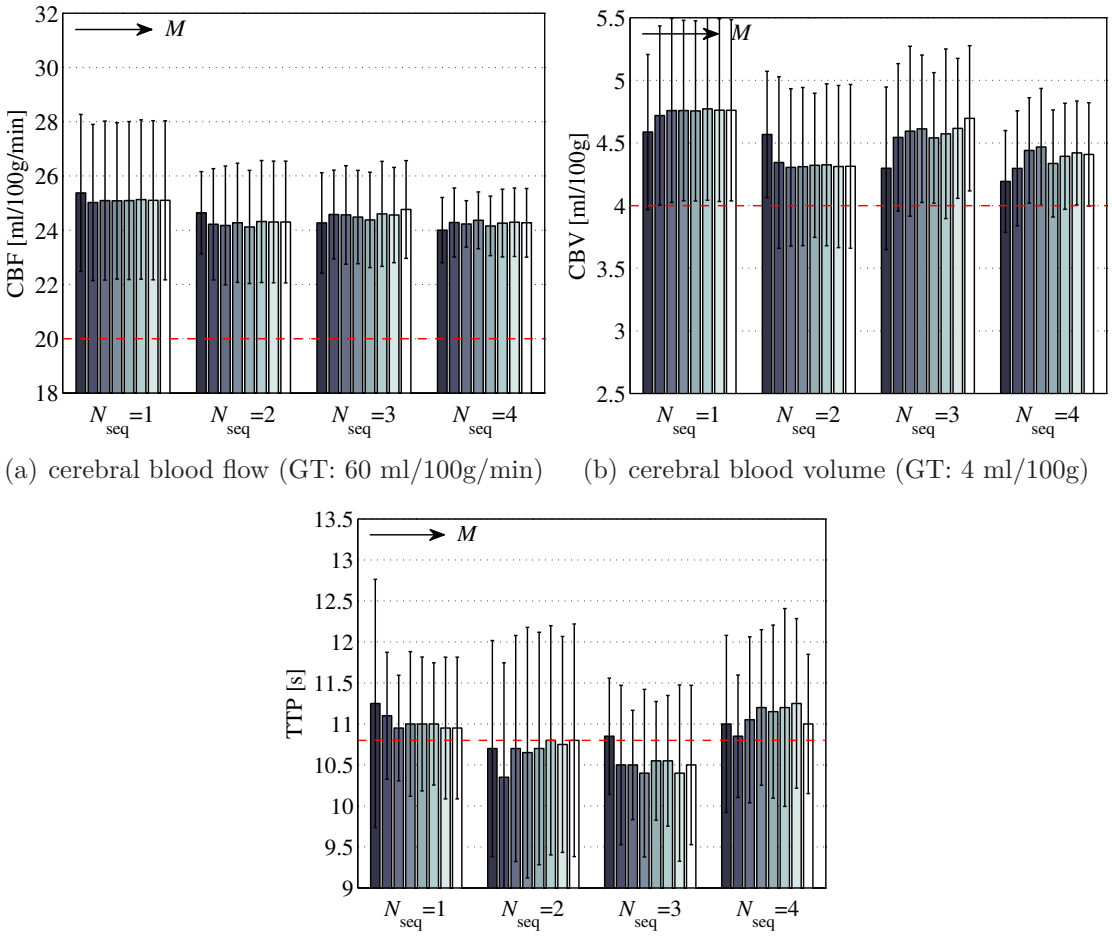

(a) cerebral blood flow (GT: 60 ml/100g/min) (b) cerebral blood volume (GT: 4 ml/100g)

(c) time-to-peak (GT: 6.9 s)

Figure 4.5: Simulation with noisy, synthetic data: Mean and standard deviation of estimated CBF, CBV and TTP with known ground truth (GT; dashed line) depending on different number N_{seq} of interleaved sequences and different numbers $M \in \{1, 2, 3, 4, 5, 6, 12, 18\}$ of angular interpolation intervals (the bars are ordered in increasing numbers of M) investigated using pathological tissue and applying linear interpolation as interpolation method.

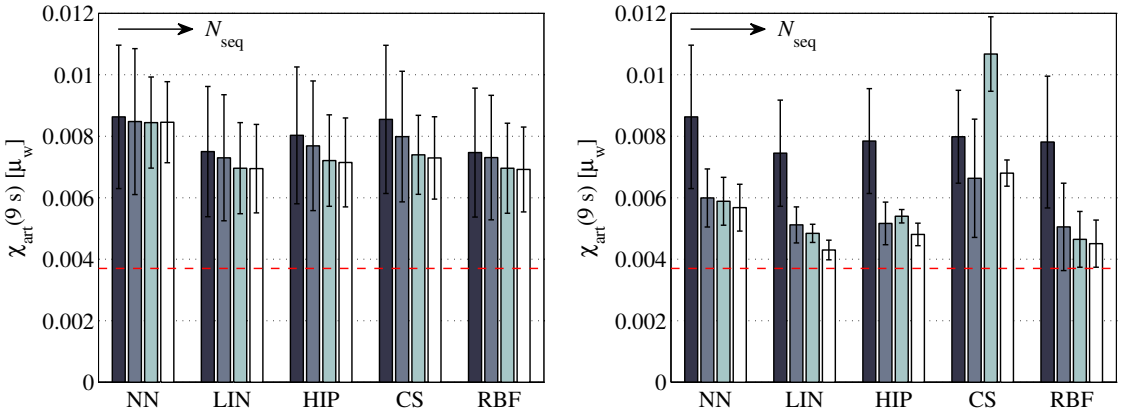

(a) $M = 1$, $N_{\text{seq}} = 3$, fixed time: $t = 9\,\text{s}$

(b) $M = 6$, $N_{\text{seq}} = 3$, fixed time: $t = 9\,\text{s}$

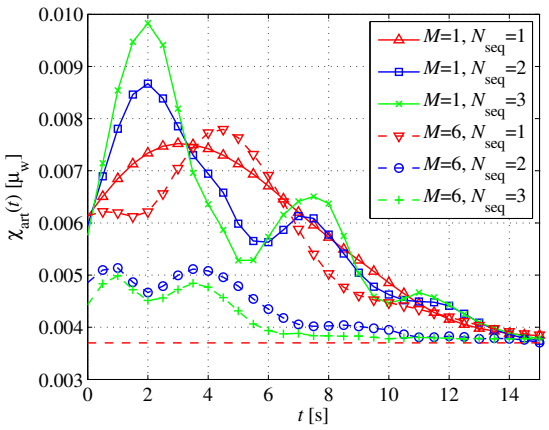

(c) $\bar{\chi}_{\text{art}}(t)$ as a function of time, LIN interpolation

Figure 4.6: Simulation with noisy, synthetic data: (a–b) Mean and standard deviation of the reconstruction artifact $\bar{\chi}_{\text{art}}(t)$ around the simulated arterial vessel at time point $t = 9\,\text{s}$ for different numbers $N_{\text{seq}} \in \{1, 2, 3, 4\}$ of interleaved sequences (the bars are ordered in increasing numbers of N_{seq}) and interpolation methods (abbreviations explained in Section 4.2.4). μ_{w} is the X-ray attenuation of water. (c) Plot of $\bar{\chi}_{\text{art}}(t)$ computed with linear interpolation (LIN) as a function of time. The dashed lines indicate the value for the component of $\bar{\chi}_{\text{art}}$ that is purely due to noise. Optimal results should be close to the value of this dashed line.

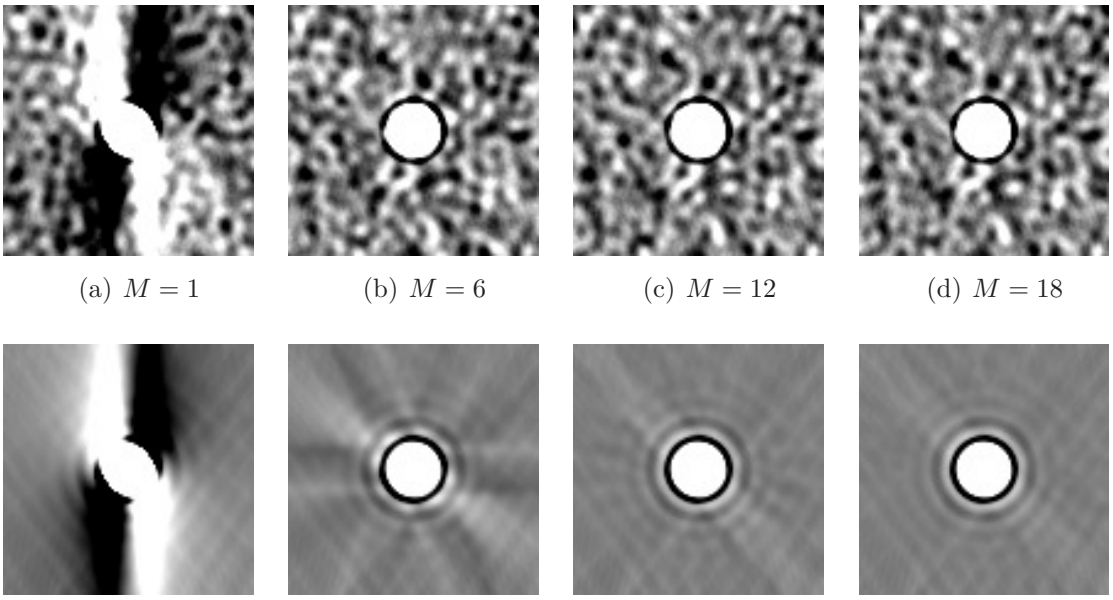

(a) $M = 1$ (b) $M = 6$ (c) $M = 12$ (d) $M = 18$

(e) $M = 1$ (f) $M = 6$ (g) $M = 12$ (h) $M = 18$

Figure 4.7: Reconstruction of a simulated arterial vessel with time-varying attenuation values from (a–d) noisy and (e–h) noise-free input data using $N_{\text{seq}} = 3$ interleaved sequences. M is the number of angular interpolation intervals. The windowing is from –10 HU (black) to +10 HU (white).

Figure 4.5 shows the CBF, CBV and TTP of the simulated pathological tissue as a function of different number M of interpolation intervals when using linear interpolation. For $N_{\text{seq}} \in \{3, 4\}$ the mean of the estimations of CBV and TTP varies with increasing M values while the CBF estimation is nearly unaffected by different M values. It can be observed that the results with $M \in \{12, 18\}$ are similar to the results with $M = 6$. Generally, the estimation of the perfusion parameters does not improve significantly when increasing M for neither the pathological tissue (Figure 4.5) nor for the healthy tissue (data omitted for brevity).

Results for the reconstruction artifact around the simulated artery are shown in Figure 4.6. Figure 4.6(c) shows $\bar{\chi}_{\text{art}}(t)$ for different time points t when using the linear interpolation method. If $N_{\text{seq}} > 1$ then the value of $\bar{\chi}_{\text{art}}(t)$ decreases for $M = 6$ when compared to $M = 1$. For comparison of different interpolation methods, in Figure 4.6(a)–(b) the mean and standard deviation is plotted for a reconstruction time point during the arterial outflow phase ($t_{\text{est}} = 9\,\text{s}$, see Figure 4.3(a)). The value of $\bar{\chi}_{\text{art}}(9\,\text{s})$ from a reconstruction without any simulated contrast agent flow is indicated with a dashed line, this value is purely due to the noise in the projection images and thus also the reconstructed images, cf. definition of $\bar{\chi}_{\text{art}}$ in Equation (4.17).

As a visual example Figure 4.7 shows reconstructions of the simulated arterial vessel at the time point $t_{\text{est}} = 9\,\text{s}$ for different numbers M, here with an in-plane voxel spacing of 0.1 mm. Additionally, also the results obtained from noise-free input data are presented in this figure.

4.3.4 Discussion

The results show that perfusion parameters can be measured with less variability, i.e. lower standard deviation, when several ($N_{\text{seq}} > 1$) interleaved sequences are used. A few exceptions exist that could be explained due to the specific sampling pattern, see Equation (4.1) and the shape of the synthetic curves which could be optimal for specific values of N_{seq}. The mean value estimation of the perfusion parameters is not generally improved with an increased number N_{seq} of interleaved sequences.

In brain perfusion imaging the relative comparison of perfusion values in the healthy and diseased hemispheres is more significant than absolute perfusion values [3]. Therefore, the variability of the measurements is a more important aspect than the mean values.

For $N_{\text{seq}} \geq 2$ the performance of the different interpolation methods is comparable. Linear and nearest neighbor interpolation may be favored in practice because they can be implemented such that they are computationally very fast. Of these two methods, linear interpolation shows slightly better results (e.g., lower variability of CBF, CBV and TTP measurements for $N_{\text{seq}} = 2$). With two interleaved sequences the variability for the measured perfusion parameters may already be low enough for application in brain perfusion imaging.

For $N_{\text{seq}} > 1$, the variability of the parameters CBF and CBV does not decrease for increasing M. This effect can be explained by the deconvolution-based perfusion analysis. If $M = 1$ then the reconstructed time curves have been low-pass filtered before sampling and interpolation. The low-pass filtering can be approximated by a convolution with a rectangular function of temporal width T_{rot} (Section 4.2.1). Note, both the arterial and the tissue curves are low-pass filtered with a similar filter kernel. Mathematically, the deconvolution operation of two functions is invariant to a preceding convolution of each function with the same filter kernel.

It should be noted that other measures of the tissue time curves which do not depend on the normalization with the arterial time curve, such as peak value, can improve for increasing M as has been shown in [22]. However, the investigation of clinically relevant parameters such as CBF is more significant.

The major advantage of using $M > 1$ can be seen in Figures 4.6 and 4.7. When using the PRI approach it is possible to approximate a consistent data set of projection values and to reduce the reconstruction artifacts due to data inconsistencies. It can be seen that for $t = 9\,\text{s}$, for example, the artifact is reduced almost completely if $N_{\text{seq}} \geq 2$. This can be explained by the linear slope of the arterial time-attenuation curve at this time point which enables accurate estimation of the unknown data by means of linear interpolation. Choosing higher numbers M of angular interpolation intervals than $M = 6$ does not significantly improve the results, although small changes can be seen in the noise-free data of Figure 4.7. Therefore, it is suggested setting M to 6 in order to reduce the computational complexity.

4.4 In Vivo Study

In order to show the clinical feasibility of the novel IS-PRI approach and to validate it under realistic conditions, an *in vivo* brain perfusion study with 5 healthy pigs has been conducted where perfusion CT was used as reference for the validation.

4.4.1 Material and Methods

The following procedure was performed under institutional review board approval for each of the 5 perfusion-normal pigs (mean weight $54 \pm 4.7\,\mathrm{kg}$). The pig was sedated and placed on a respirator. A 5-French diffusion catheter (Vanguard, Medrad Inc, Idianola, PA, USA) was placed at the root of the aortic arch under fluoroscopic guidance. During the study iodinated contrast agent (Omnipaque, 350 mg iodine/ml, Nycomed, Princeton, NJ, USA) was injected — which was diluted with an equal amount of saline — using a programmable dual head power injector (Accutron HP-D, Medtron AG, Saarbrücken, Germany). Using this injector, delay times could be programmed with 0.1 s precision. Each bolus was injected at a rate of 6 ml/s for 8 s, resulting in 24 ml of pure contrast agent per injection.

A number $N_{\mathrm{seq}} = 6$ interleaved sequences were acquired with a clinical C-arm CT system (Axiom Artis *d*TA with syngo DynaCT, Siemens AG, Healthcare Sector, Forchheim, Germany) using the C-arm CT scan parameters from set 2 of Table 4.1. Retrospectively, three additional subsets of sequences with $N_{\mathrm{seq}} = 1$ (1^{st} sequence of the superset), $N_{\mathrm{seq}} = 2$ (1^{st} and 4^{th} sequence of the superset) and $N_{\mathrm{seq}} = 3$ (1^{st}, 3^{rd} and 5^{th} sequence of the superset) were created. The size of each reconstructed volume was $256 \cdot 256 \cdot 256$ isotropic voxels with a voxel side length of 0.5 mm and the interpolation sampling interval was 1 s. Based on the experience from the simulations the number M of interpolation intervals was set to 6 and linear interpolation was used.

For validation, a perfusion CT (first 2 animals: Somatom Sensation 64, Siemens AG, Healthcare Sector, Erlangen, Germany; last 3 animals: LightSpeed 16, GE Healthcare, Milwaukee, WI, USA) was acquired for each of the 5 animals with the same injection parameters as for the C-arm CT scans. The data from the perfusion CT exam was reconstructed with a pixel size of $0.39 \cdot 0.39\ \mathrm{mm}^2$, a slice thickness of 9.6–10.0 mm and a temporal sampling interval of 0.5–1.0 s. For the C-arm CT data reconstructions were created which had with similar slice thicknesses by applying a moving average filter (kernel size 9.5–10.0 mm) perpendicular to the orientation of the reconstructed slices.

After reconstruction of the 4-D C-arm CT data set the time-attenuation curves in an arterial and a venous vessel and in a tissue region were evaluated qualitatively. A quantitative evaluation was carried using the computed perfusion parameter maps.

For this evaluation, at first the 3-D C-arm CT perfusion maps were registered onto the 2-D perfusion maps (2–3 slices per animal) obtained with CT. A rectangular grid with a line spacing of 10 pixels was used to subdivide the whole brain area into square ROIs. For each ROI the mean perfusion values (CBF, CBV, MTT) were computed using software based on the TSVD algorithm (Algorithm 2.1).

The linear correlation r_{corr} [62] between the perfusion CT map and the (registered) perfusion C-arm CT map was determined by using the data from all ROIs. In order

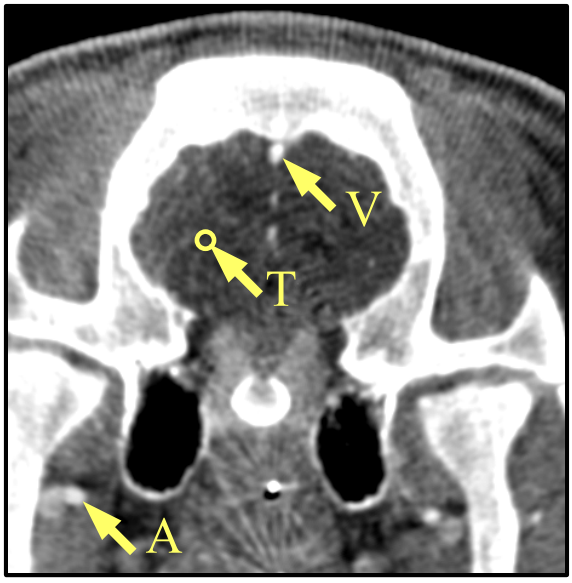

Figure 4.8: Transversal C-arm CT image of a pig head that shows the locations of the extra-cranial arterial (A) and intra-cranial venous (V) vessels and the tissue (T) region that were selected for plotting of the time-attenuation curves shown in Figure 4.9. The windowing range is from –75 HU to +375 HU.

to decrease the influence of large vessels a vascular pixel elimination (VPE) was additionally applied; similar to the method described in [98]. If the mean CBV value from perfusion CT in a certain square ROI was above the threshold value of 8 ml/100g (this value was suggested in [98] for human data and it was assumed that it also applies to the data from the *in vivo* pig studies because of the similarities of the human brain and the pig brain [140]) then the data from this ROI was not used for the correlation analysis.

An alternative evaluation method would be to manually select ROIs in different gray and white matter regions as done in [25]. The evaluation conducted in this chapter does not require manual selection of ROIs and is therefore user-independent.

4.4.2 Results

Figure 4.8 shows the locations of the arterial and venous vessels and the tissue regions that were selected for investigation of the time-attenuation curves. The time-attenuation curves from one animal are shown in Figure 4.9. With increasing N_{seq} the FWHM of the reconstructed curves decreases and gets closer to the value from the reference CT. The curves obtained with IS-PRI are generally smoother than the curves from CT. The smoothest curves are obtained with $N_{\text{seq}} = 1$. These qualitative findings also hold for the results of the other 4 animals of the study.

A representative 3-D CBF data set of one animal is given in Figure 4.10 by displaying 3 orthogonal planes through the volume. No severe asymmetry can be seen in the transversal and coronal planes as would be expected from a healthy animal. Figure 4.11 shows a comparison of the CBF maps of one animal obtained with perfusion CT and with perfusion C-arm CT using IS-PRI ($N_{\text{seq}} = 2$, $M = 6$).

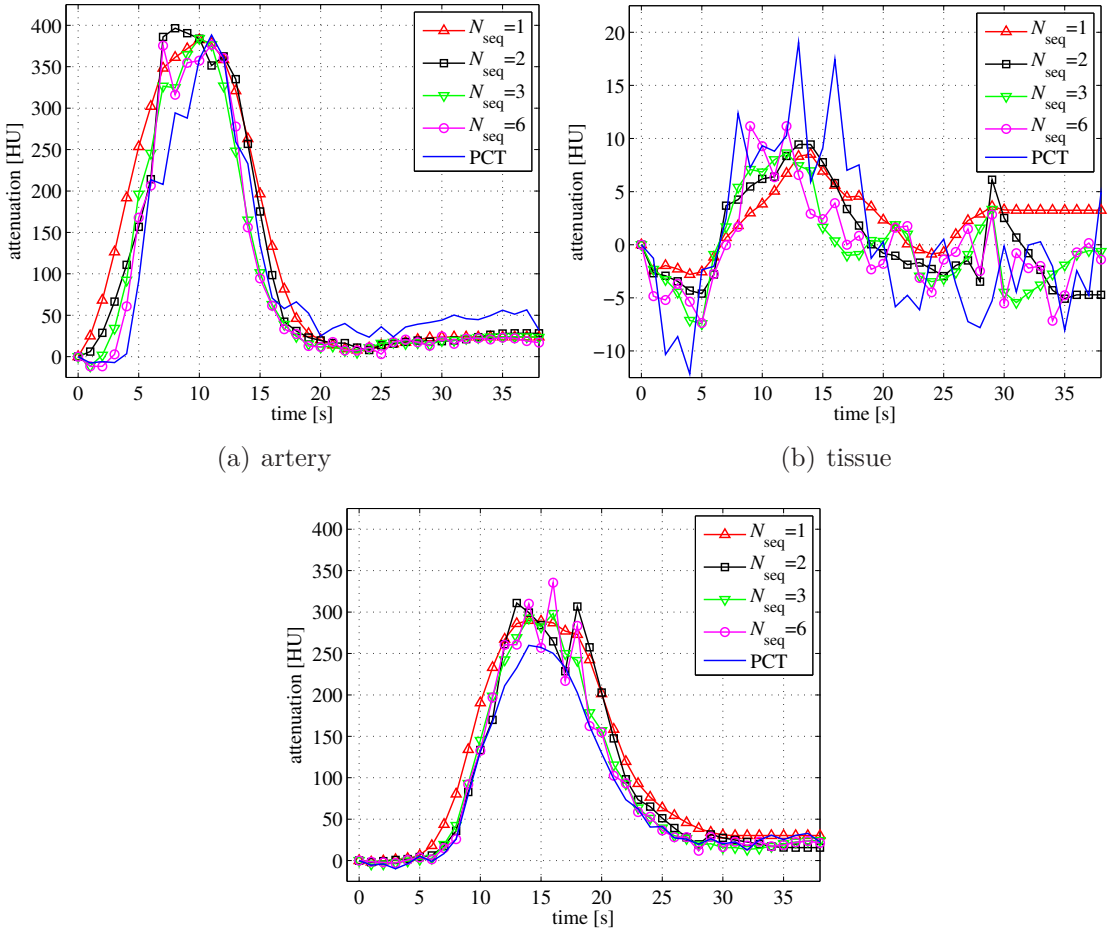

(a) artery

(b) tissue

(c) vein

Figure 4.9: Reconstructed time-attenuation curves obtained from one pig in the *in vivo* studies using different numbers $N_{\text{seq}} \in \{1, 2, 3, 4\}$ of interleaved sequences and $M = 6$ angular interpolation intervals. The data from a perfusion CT (PCT) exam is given as reference. For each curve the first sample point value was subtracted to allow for better comparison.

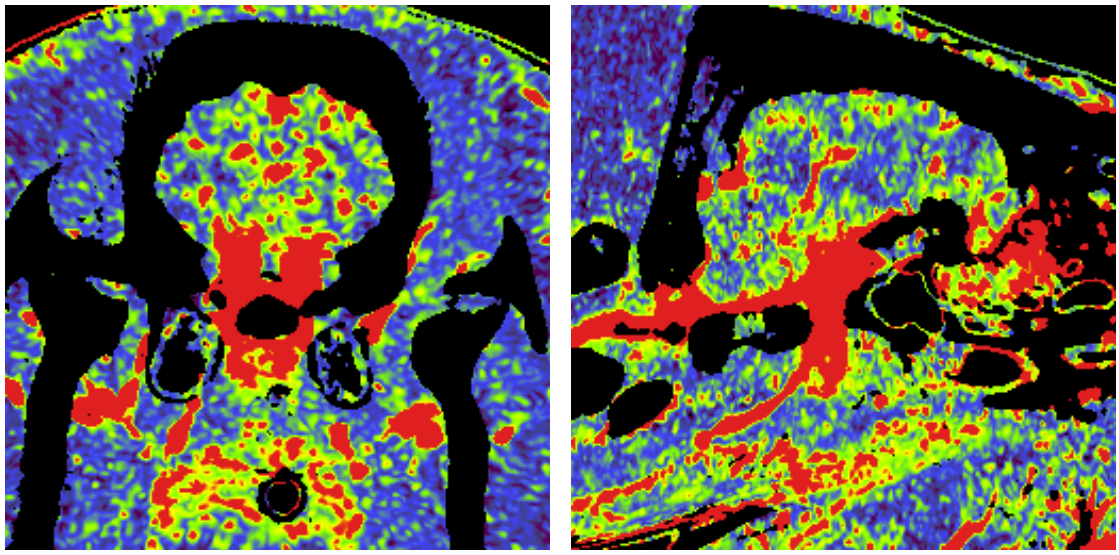

(a) coronal (b) sagittal

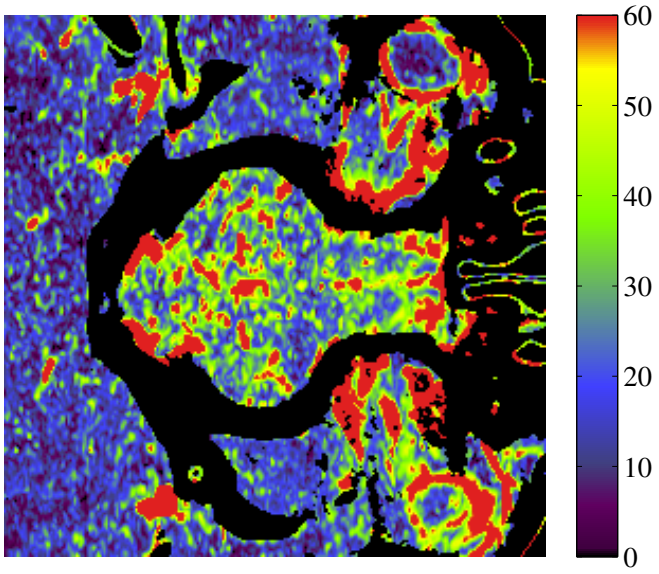

(c) transversal

Figure 4.10: 3-D CBF data (unit: ml/100g/min) of a perfusion-normal pig computed from 4-D data acquired using the IS-PRI approach. The color bar applies to all three images.

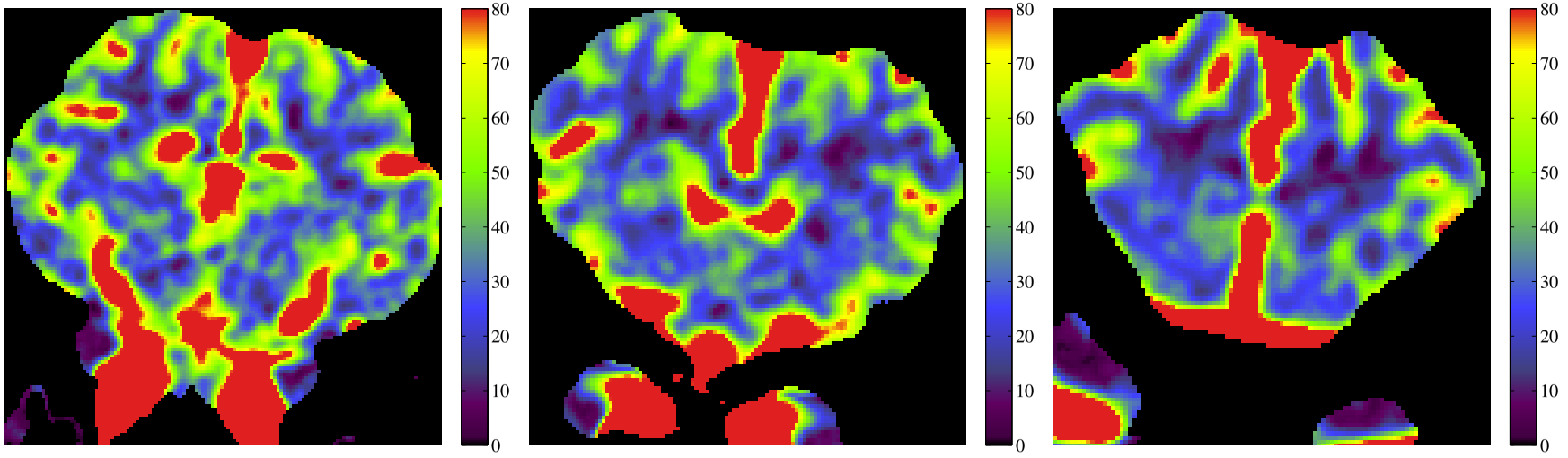

(a) PCT, slice 1 (b) PCT, slice 2 (c) PCT, slice 3

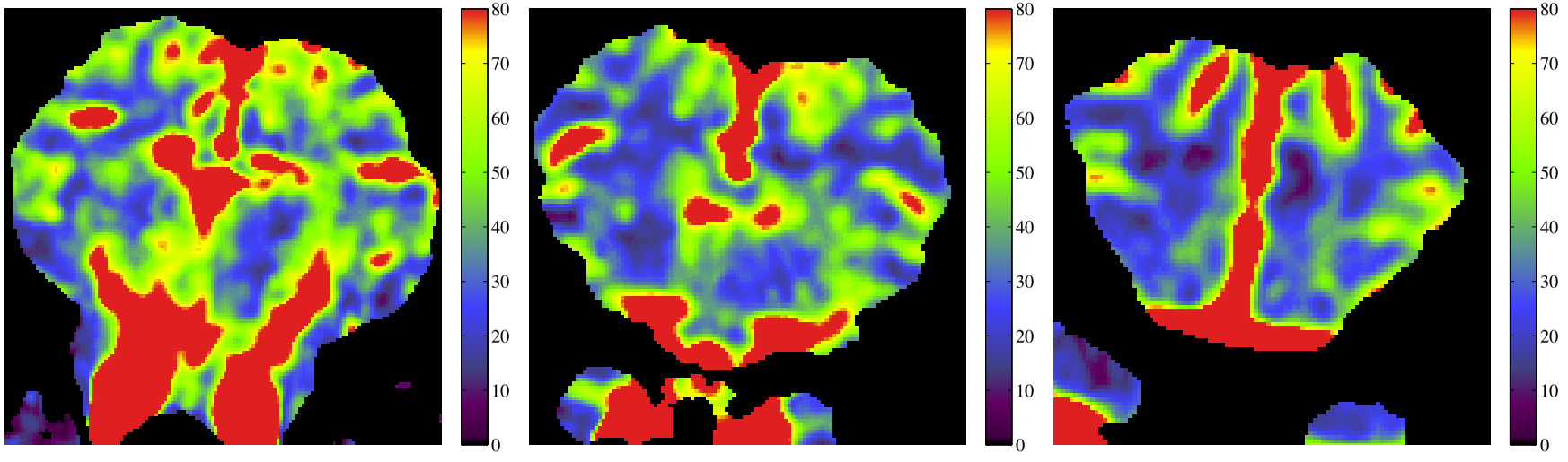

(d) IS-PRI, slice 1 (e) IS-PRI, slice 2 (f) IS-PRI, slice 3

Figure 4.11: CBF maps (units: ml/100g/min) of a perfusion-normal pig obtained with (a–c) perfusion CT (PCT) and (d–f) perfusion C-arm CT using the IS-PRI approach. The 3-D volume CBF data from IS-PRI was registered onto the 2-D maps from perfusion CT.

Parameter	VPE	N_{seq}	A	B	C	D	E	Mean ± SD
CBF [ml/100g/min]	no	1	0.97	0.92	0.91	0.87	0.95	0.92 ± 0.04
CBF [ml/100g/min]	yes	1	0.79	0.80	0.58	0.54	0.62	0.67 ± 0.12
CBV [ml/100g]	no	1	0.98	0.96	0.92	0.87	0.96	0.94 ± 0.05
CBV [ml/100g]	yes	1	0.75	0.73	0.52	0.42	0.49	0.58 ± 0.15
CBF [ml/100g/min]	no	2	0.97	0.95	0.93	0.88	0.94	0.94 ± 0.03
CBF [ml/100g/min]	yes	2	0.79	0.82	0.74	0.55	0.63	0.71 ± 0.11
CBV [ml/100g]	no	2	0.98	0.96	0.93	0.89	0.96	0.94 ± 0.04
CBV [ml/100g]	yes	2	0.78	0.77	0.59	0.46	0.53	0.63 ± 0.14
CBF [ml/100g/min]	no	3	0.93	0.95	0.94	0.89	0.93	0.93 ± 0.02
CBF [ml/100g/min]	yes	3	0.80	0.83	0.78	0.59	0.65	0.73 ± 0.10
CBV [ml/100g]	no	3	0.98	0.96	0.94	0.91	0.95	0.95 ± 0.03
CBV [ml/100g]	yes	3	0.77	0.76	0.71	0.51	0.61	0.67 ± 0.11

Table 4.2: Linear correlation coefficient r_{corr} between perfusion parameters that were measured with CT and C-arm CT in 5 healthy pigs (labeled from A to E). VPE: vascular pixel elimination, SD: standard deviation.

Table 4.2 shows the linear correlation coefficients r_{corr} between perfusion CT and perfusion C-arm CT parameters for the results with and without VPE. For brevity, the detailed results for MTT have been omitted. The mean correlations for MTT were generally lower ($r_{\text{corr}} = 0.12$ with VPE, $r_{\text{corr}} = 0.35$ without VPE for $N_{\text{seq}} = 2$) but also showed an increase for increasing N_{seq} ($r_{\text{corr}} = 0.31$ with VPE, $r_{\text{corr}} = 0.51$ without VPE for $N_{\text{seq}} = 3$).

4.4.3 Discussion

The results from Figure 4.9 show that the time-attenuation curves measured with the IS-PRI approach are comparable to those measured with CT. The smoothness of the curves with IS-PRI could be explained by the potential undersampling, especially at low numbers N_{seq}, and the interpolation, both of which act as a low-pass filtering.

Compared to conventional multi-slice perfusion CT it is possible to measure volumetric perfusion with the IS-PRI approach (Figure 4.10). A detailed discussion of the advantages of volumetric perfusion measurement for stroke diagnosis is provided in [141].

The mean correlation of the computed C-arm CT perfusion values with perfusion CT increases for increasing N_{seq} regardless of whether vascular pixels are kept or eliminated. While the mean correlation is highest when vascular pixels are included in the analysis, it is also very high if the vascular pixels are removed. In that case the improvement when using increasing numbers N_{seq} is most prominent. The standard deviation of the mean correlation decreases for increasing N_{seq}. The evaluation with VPE may be clinically more significant, in order to evaluate tissue perfusion, than the

evaluation without VPE. Nevertheless, the results without VPE show the correlation between perfusion CT and perfusion C-arm CT values on a broader range of values.

Higher numbers M of angular interpolation intervals were not evaluated as the results from the simulations did not show a significant improvement for $M > 6$. The simulations showed that reconstruction artifacts could be reduced with $M = 6$ compared to $M = 1$. With *in vivo* data these reconstruction artifacts were difficult to evaluate due to the lack of ground truth data.

In order to increase the CNR of the measured tissue time-attenuation curves a contrast agent bolus injection at the aortic arch was used (Chapter 5). With this injection, which is feasible during stroke therapy procedures in the interventional suite, the fraction of contrast agent that actually reaches the brain is increased compared to an intra-venous contrast agent bolus injection (Section 5.1).

The interleaved scanning with multiple contrast agent bolus injections is based on the assumption that similar contrast agent flow patterns can be generated in the patient's brain for each bolus injection. With contrast agent bolus injections at the aortic arch the bolus travel time to the brain is very short which improves the reproducibility of the contrast agent flow pattern. ECG-triggered contrast agent bolus injections, which were not performed in this study due to hardware constraints, could reduce the influence of the cardiac cycle [132] which could further increase the reproducibility.

The necessity for two separate injections could be relaxed if a biplane C-arm angiography system was used where both planes could acquire projections simultaneously during the C-arm rotation. In that case two interleaved sequences could be acquired with only one contrast agent bolus injection.

The study was not optimized for X-ray dose reduction. When used in clinical practice the applied dose of a protocol with two interleaved scan sequences may be similar to the applied dose of current volume perfusion CT protocols [142].

A more detailed analysis of the clinical data focusing on clinical aspects such as different injection protocols and a differentiation of gray and white matter was carried out in [25]. In [25] the correlation between perfusion CT and perfusion C-arm CT was computed using manually selected circular ROIs and a linear correlation of $r_{\text{corr}} = 0.88$ was obtained with two interleaved sequences. Also with the automatic, user-independent ROI selection approach as carried out in this chapter the correlation of CBF and CBV is very high (ranging from $r_{\text{corr}} = 0.63$ to $r_{\text{corr}} = 0.94$ for $N_{\text{seq}} = 2$).

4.5 Summary and Conclusion

A novel combined scanning and reconstruction approach was presented in this chapter that allows for tissue perfusion measurement in the interventional suite. Emphasis was put on computational speed of the methods, e.g. by using a modified FDK-based reconstruction algorithm, so that this technique could be used for intra-operative imaging during stroke therapy procedures (Section 4.1.1).

Using numerical simulations it has been shown that with two interleaved sequences the variability of estimated perfusion values is sufficiently low such that this method could be used for clinical decision making. These simulations were carried out with C-arm CT scan parameters that are representative of current systems (Table 4.1).

The results are expected to improve with faster C-arm rotation speeds accompanied by faster detector readout rates and shorter waiting times between rotations, e.g. realized with robotic C-arm CT systems such as the Artis zeego (Siemens AG, Healthcare Sector, Forchheim, Germany). Furthermore, with new biplane C-arm angiography systems the two interleaved sequences could be acquired using a single contrast agent bolus injection only.

The *in vivo* studies were based on a healthy pig model and the perfusion parameter maps computed from data acquired with the novel IS-PRI approach showed promising correlations with those from a reference perfusion CT. Further validation in stroke cases and human patient studies is necessary and should be carried out in the future.

Chapter 5

Evaluation of Contrast Agent Bolus Injection at the Aortic Arch: Automatic Measurement of Bolus Distribution

Overview:
In this chapter, a novel algorithm for time-resolved 2-D DSA image data is presented. It is used to evaluate a contrast agent injection protocol that applies an injection at the aortic arch for C-arm CT perfusion imaging. The algorithm performs an automatic segmentation of both common carotid arteries (CCA) based on dedicated spatio-temporal weighting functions. Then it computes the relative distribution of the contrast agent bolus between the CCAs. A uniform distribution of the contrast agent is actually desirable for comparison of perfusion between the left and right hemispheres. The algorithm can be used for retrospective evaluation of the bolus distribution to assess new injection protocols or for intra-procedural optimization of the injection catheter location.

This chapter is based on "Automatic Measurement of Contrast Bolus Distribution in Carotid Arteries Using a C-arm Angiography System to Support Interventional Perfusion Imaging", by A. Fieselmann, A. Ganguly, Y. Deuerling-Zheng, J. Boese, J. Hornegger, and R. Fahrig. In *Proc. SPIE Medical Imaging 2011: Visualization, Image-Guided Procedures, and Modeling*, volume 7964, pages 79641W1–6, Lake Buena Vista, USA, 2011 [30].

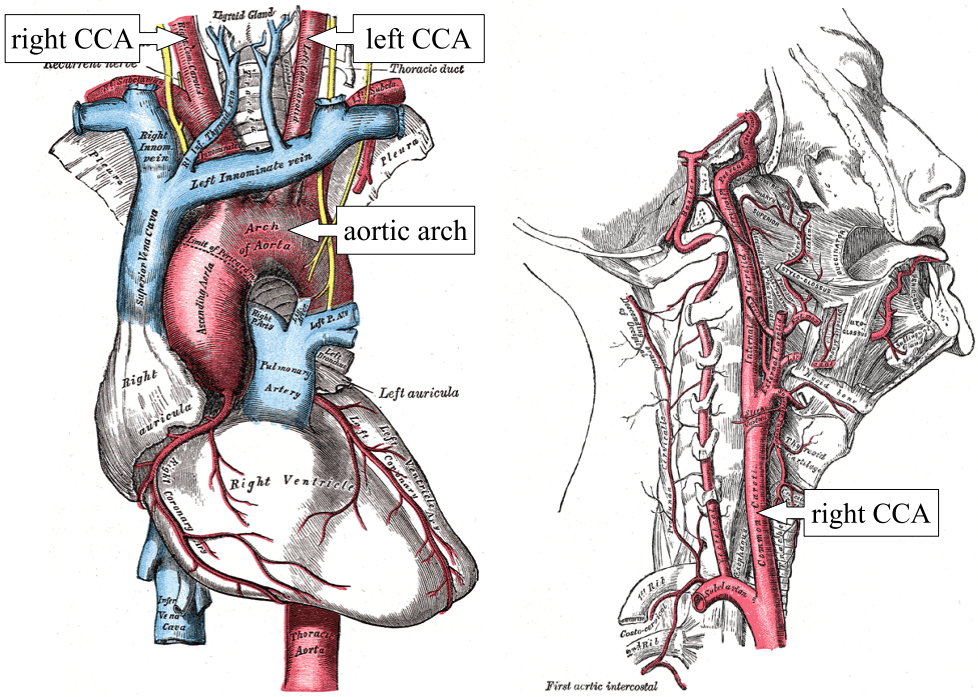

(a) aortic arch and CCAs (b) right CCA

Figure 5.1: (a) Anteroposterior view onto the heart with labeled aortic arch and right and left common carotid artery (CCA). (b) View onto the right CCA. Original images taken from [146].

5.1 Introduction

In CT and MR brain perfusion imaging the contrast agent bolus is injected intravenously. Usually a large vein of the arm (antecubital vein) is chosen [143, 144]. After an IV injection the bolus travels through the heart and the lung and it is well-mixed with the blood when it arrives in the brain. This type of contrast agent bolus injection can also be used in perfusion C-arm CT imaging. However, for this application, also alternative contrast agent bolus injection strategies would be possible since the patient is located in the interventional suite and already catheterized for vascular therapy (Section 1.2).

For example, the contrast agent bolus could be injected directly into an artery using an injection catheter. A selective injection into one of the two common carotid arteries (CCA, Figure 5.1) would be possible. This approach is already applied for the acquisition of DSA data [9, 145], for example. However, when using this kind of injection approach, the bolus would flow into one of the hemispheres of the brain only. Therefore, no comparison of the perfusion between the left and right hemispheres could be carried out which is actually desirable in perfusion imaging.

A different approach would be to inject the contrast agent bolus at the root of the aortic arch (Figure 5.1(a)). This would allow the bolus to flow into both CCAs. This kind of bolus injection has two potential advantages.

1. The fraction of the contrast agent that actually reaches the brain is expected to be higher when compared to an IV injection. Note, after an IV injection a significant fraction of the contrast agent bolus will flow directly to the trunk and lower extremities after leaving the heart. A higher fraction of the contrast agent bolus that reaches the brain results in a higher SNR of the measured TACs, which is desirable for the subsequent image analysis. Alternatively, instead of increasing the SNR, the amount of injected contrast agent could be reduced while providing a similar SNR when compared to an IV injection.

2. Because the traveling time from the aortic arch to the brain is relatively short, physiological variations (e.g., heart rate) during the traveling time will have a smaller influence when compared to an IV injection. This can lead to more reproducible contrast bolus injections which are required for the interleaved scanning approach presented in Chapter 4.

In order to compare perfusion values between the left and right hemispheres, equal amounts of contrast agent are required to flow into both CCAs. However, the exact location of the injection catheter at the aortic arch and potentially also further injection parameters can influence the distribution of the contrast agent bolus in the CCAs.

In this chapter, an automatic algorithm will be presented to quantify the contrast agent bolus distribution in the CCAs based on time-resolved 2-D DSA data. The algorithm will be applied to data acquired as part of a C-arm CT perfusion study (Section 4). The aim is to investigate if a uniform contrast agent distribution is possible when using an injection at the aortic arch. The algorithm could also be used during the intervention in order to optimize the injection catheter position by providing additional quantitative information.

5.2 Description of the Algorithm

Figure 5.2 and Algorithm 5.1 depict an overview of the algorithm. After pre-processing of the raw data (step 1), the CCAs are segmented fully automatically (step 2). Then the end of the contrast agent wash-in phase is determined from the time-intensity curves of the CCAs (step 3). This information is necessary to compute the so-called contrast agent volume map (step 4). Finally, the contrast agent volume map and the segmentation result of the CCAs are used to compute the carotid contrast agent distribution ratio (CCDR) parameter (step 5).

5.2.1 Pre-processing

The first step of the algorithm is the pre-processing of the measured data. The variable $p_{\text{sub}}(u, v, t)$ is introduced in order to denote the baseline-subtracted projection values at the detector coordinates (u, v) and at time t. In this chapter, all variables are denoted as continuous variables for simplicity. In a practical implementation they can only take discrete values, of course. The baseline subtraction is accomplished by subtraction of the projection value before contrast agent enters the field of view.

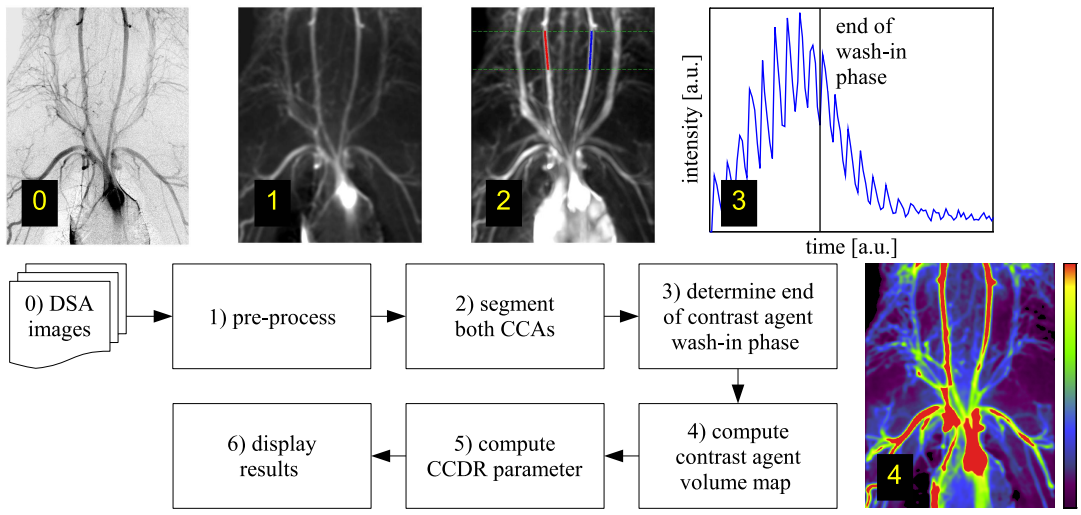

Figure 5.2: Overview of the algorithm to measure the contrast agent bolus distribution (CCDR) in the common carotid arteries (CCA).

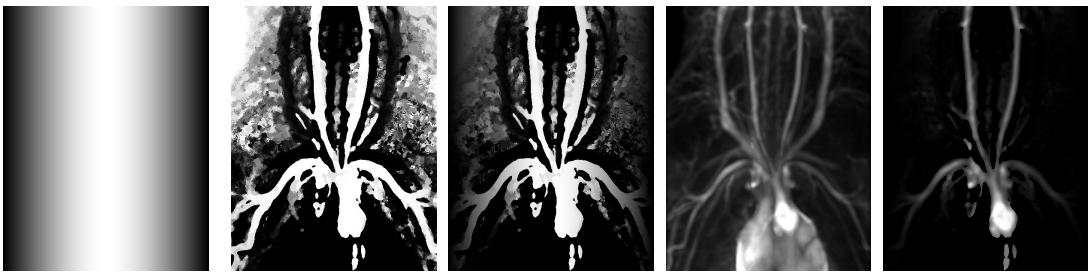

(a) w_{spt} (b) w_{tmp} (c) w_{cmb} (d) p_{tMIP} (e) $p^{\mathrm{w}}_{\mathrm{tMIP}}$

Figure 5.3: (a–c) Spatial (w_{spt}), temporal (w_{tmp}) and combined (w_{cmb}) weighting functions. The windowing is from 0 (black) to 1 (white). (d–e) Unweighted tMIP (p_{tMIP}) and tMIP weighted with w_{cmb} ($p^{\mathrm{w}}_{\mathrm{tMIP}}$). Both tMIPs have the same windowing from 0 (black) to the half maximum of the image data corresponding to (d) (white).

Note, to convert the measured photon flux density into line integrals of attenuation values, i.e. projection values, a logarithmic transform and a change of sign must be applied first. To reduce noise, a 2-D spatial Gaussian filter with standard deviation of 2.5 mm is applied to all time instances of $p_{\mathrm{sub}}(u, v, t)$.

5.2.2 Segmentation of Carotid Arteries

The common carotid arteries are segmented from a temporal maximum intensity projection (tMIP) of $p_{\mathrm{sub}}(u, v, t)$ which will be denoted as $p_{\mathrm{tMIP}}(u, v)$. First, a spatio-temporal weighting of $p_{\mathrm{tMIP}}(u, v)$ is applied in order to increase the intensity of the CCAs relative to other structures. The combined weighting function $w_{\mathrm{cmb}} \in [0, 1]$ has a factor $w_{\mathrm{spt}} \in [0, 1]$ that uses prior knowledge of the spatial position of the CCAs

and a factor $w_{\text{tmp}} \in [0,1]$ that uses prior knowledge of the expected temporal contrast agent dynamics. The weighted tMIP, denoted by $p^{\text{w}}_{\text{tMIP}}(u,v)$, is then given by

$$\begin{aligned} p^{\text{w}}_{\text{tMIP}}(u,v) &= w_{\text{cmb}}(u,v) \cdot p_{\text{tMIP}}(u,v) \\ &= w_{\text{spt}}(u) \cdot w_{\text{tmp}}(u,v) \cdot p_{\text{tMIP}}(u,v) \ . \end{aligned} \tag{5.1}$$

The weighting functions $w_{\text{spt}}(u)$ and $w_{\text{tmp}}(u,v)$ will be described next. The spatial weighting assumes that the CCAs can be found near the center of the image. To mathematically define $w_{\text{spt}}(u)$, the 1-D Gaussian-type function $G_f(x)$ is introduced as

$$G_f(x) = \varsigma_1 \cdot \frac{1}{(2\pi\,\varsigma_2^2)^{0.5}} \cdot \exp\left(-\frac{x^2}{2\,\varsigma_2^2}\right) = \exp\left(-\left(\frac{2\,(\ln(2))^{0.5}}{f}x\right)^2\right) \ . \tag{5.2}$$

It has the amplitude scaling factor ς_1 and the standard deviation ς_2,

$$\varsigma_1 = (2\pi\,\varsigma_2^2)^{0.5} \tag{5.3}$$

$$\varsigma_2 = (8\,\ln(2))^{-0.5} \cdot f \ , \tag{5.4}$$

and the parameter f which controls the FWHM. Then, $w_{\text{spt}}(u)$ is defined as

$$w_{\text{spt}}(u) = 2\,G_U(u - u_0)\ - 1 \ . \tag{5.5}$$

Here, U is the total width of the detector and u_0 is the center coordinate of the detector, both with respect to the u-coordinate. See Figure 5.3(a) for an example of $w_{\text{spt}}(u)$. Different smooth weighting functions would of course also be possible.

The temporal weighting assumes that the contrast agent arrives earlier in the arteries than in the draining veins. The expected time-to-peak value of the time-intensity curve measured in the CCAs is denoted by $t_{\text{max,e}}$. This value can be chosen relative to the duration T_{inj} of the contrast agent injection. For example, it can be set to $t_{\text{max,e}} = 1.2\,T_{\text{inj}}$. The temporal weighting function $w_{\text{tmp}}(u,v)$ is then defined as

$$w_{\text{tmp}}(u,v) = \begin{cases} 1 & \text{, for } t_{\max}(u,v) < t_{\text{max,e}} \\ G_{t_{\text{max,e}}}(t_{\max}(u,v) - t_{\text{max,e}}) & \text{, for } t_{\max}(u,v) \geq t_{\text{max,e}} \end{cases} \tag{5.6}$$

$$t_{\max}(u,v) = \arg\max_t(p_{\text{sub}}(u,v,t)) \ , \tag{5.7}$$

where $t_{\max}$ is the time-to-peak at position (u,v). An example for $w_{\text{tmp}}(u,v)$ is shown in Figure 5.3(b).

For the following analysis of the bolus distribution, a complete segmentation of the CCAs is not required. Thus, the CCAs are only segmented in a ROI where $v \in [v_{\text{c}} - v_{\text{w}}/2, v_{\text{c}} + v_{\text{w}}/2]$. The parameters $v_{\text{w}} = 60$ mm and $v_{\text{c}} = v_{\text{max,cran}} - v_{\text{w}}$ are used where $v_{\text{max,cran}}$ is the v-coordinate at the cranial end of the image. These parameters have been chosen empirically and work well for typical DSA data sets acquired at the aortic arch. In the future, a more adaptive ROI selection may be used. See Figure 5.4 for a graphical visualization of the boundaries of the ROI.

Next, the centerlines of the two CCAs can be segmented in the ROI of the image $p^{\text{w}}_{\text{tMIP}}(u,v)$. To this end, a simple technique is used that looks for the 2 highest

intensity values, separated by a minimum distance of 5 mm, along the line in the u-direction for a given v-coordinate. Two paths are created by connecting the coordinates of these maxima starting from a maximum at the left and right side respectively (Algorithm 5.1). One may introduce further prior knowledge by requiring that the centerlines are allowed to have a certain maximum curvature only. Figure 5.4 shows an example of the segmentation. Note, different 2-D vessel centerline segmentation methods exist as well and are described in [147, 148], for example.

5.2.3 Computation of Contrast Agent Volume Map

The contrast agent volume map (CVM) is introduced as a relative measure to estimate the amount of contrast agent that has flowed through a certain region. In particular, the CVM is used to compute the carotid contrast agent distribution ratio (CCDR) in Section 5.2.4. Due to the linearity of the iodinated contrast agent and the X-ray attenuation value (Section 6.1), the measured baseline-subtracted projection value $p_{\text{sub}}(u, v, t)$ is proportional to the total mass of contrast at time t that is intersected by the X-rays from the source to the pixel centered at (u,v) [99].

First, the duration $T_{\text{wash,in}}$ of the contrast agent wash-in phase is determined relative to the average time-to-peak $t_{\text{max,cca}}$ measured inside the (segmented) CCAs. For example, it can be set to $T_{\text{wash,in}} = t_{\text{max,cca}} + 1$ s where s denotes seconds. Then, the CVM, denoted by $p_{\text{cvm}}(u, v)$, is computed as

$$p_{\text{cvm}}(u, v) = \int_0^{T_{\text{wash,in}}} p_{\text{sub}}(u, v, t)\, \mathrm{d}t \; . \tag{5.8}$$

The integration interval is limited to the wash-in phase to fulfill the condition that the measured data $p_{\text{sub}}(u, v, t)$ has only contributions from a single vessel. The CVM can be displayed for a visual assessment of relative contrast agent bolus distribution. A quantitative evaluation of the CVM is done by computing the CCDR, as described in Section 5.2.4.

5.2.4 Computation of Bolus Distribution

The carotid contrast agent distribution ratio (CCDR) is computed using the segmented centerlines of the CCAs and the contrast agent volume map (CVM). For each v-coordinate in the ROI, $v \in [v_{\text{c}} - v_{\text{w}}/2, v_{\text{c}} + v_{\text{w}}/2]$, there is a u-coordinate for the segmented centerline of the left CCA (u_{left}) and the right CCA (u_{right}). For a given v-coordinate, the v-specific CCDR can be approximated as

$$\text{CCDR}_v \approx p_{\text{cvm}}(u_{\text{left}}(v), v) \;/\; p_{\text{cvm}}(u_{\text{right}}(v), v) \; . \tag{5.9}$$

The final CCDR value is computed by averaging over the values obtained using the different v-coordinates.

Algorithm 5.1: Algorithm to compute the carotid contrast agent distribution ratio (CCDR) from a 2-D DSA sequence.

Input: pre-processed projection data $p_{\mathrm{sub}}(u, v, t)$ (see Section 5.2.1)
Output: CCDR value

$p_{\mathrm{tMIP}}(u, v) \leftarrow \max_t(p_{\mathrm{sub}}(u, v, t)) \quad \forall\, u, v$
compute $p^{\mathrm{w}}_{\mathrm{tMIP}}(u, v)$ according to Equations (5.1), (5.5) and (5.6)
`// extract centerlines of left and right CCA`
forall the $v \in [v_{\mathrm{c}} - v_{\mathrm{w}}/2, v_{\mathrm{c}} + v_{\mathrm{w}}/2]$ (see Section 5.2.2) **do**
  $\zeta(u) \leftarrow p^{\mathrm{w}}_{\mathrm{tMIP}}(u, v) \quad \forall\, u$ `// intermediate variable`
  `// get location of first maximum`
  $u_{\mathrm{left}}(v) \leftarrow \arg\max_u(\zeta(u))$
  $\zeta(u_{\mathrm{left}}(v)) \leftarrow 0$
  `// get location of second maximum`
  repeat
    $u_{\mathrm{right}}(v) \leftarrow \arg\max_u(\zeta(u))$
    $\zeta(u_{\mathrm{right}}(v)) \leftarrow 0$
  until $|\zeta(u_{\mathrm{left}}) - \zeta(u_{\mathrm{right}})| \geq 5$ mm
  `// by convention, the` u`-coordinate of right CCA must be lower than the` u`-coordinate of left CCA`
  if $u_{\mathrm{right}}(v) \geq u_{\mathrm{left}}(v)$ **then**
    swap values between $u_{\mathrm{left}}(v)$ and $u_{\mathrm{right}}(v)$
  end
end
compute $p_{\mathrm{cvm}}(u, v)$ according to Equation (5.8)
compute v-specific CCDR value (CCDR_v) according to Equation (5.9)
compute final CCDR value by averaging CCDR_v over all v-coordinates

5.3 Experimental Evaluation

5.3.1 Material and Methods

The algorithm was tested using DSA sequences from 5 anesthetized healthy pigs. The data was acquired as part of the perfusion studies which are described in Chapter 4. The DSA sequences, acquired at 7.5 frames per second, were analyzed retrospectively to compute quantitative parameters. For future patient studies only slight adaptations of the algorithm to the human anatomy are expected [140].

A contrast agent bolus (Iohexol, 350 mg iodine per ml) was delivered intra-arterially at the root of the aortic arch using a 5-French diffusion catheter at different injection rates (3, 6, 9 ml/s). Contrast agent concentrations (33%–100%) were adjusted for each injection rate to provide a similar total contrast agent volume. Furthermore, different catheter positions were investigated for one injection rate (3 ml/s).

5.3.2 Results

The centerline segmentation of the CCAs succeeded in all data sets as determined by visual assessment. Hence, quantitative information about the contrast agent distribution could be computed in all data sets.

For different injection rates (IR), the mean and standard deviation of the CCDR values were 0.99 ± 0.14 (3 ml/s IR), 1.10 ± 0.13 (6 ml/s IR) and 1.06 ± 0.10 (9 ml/s IR). When the catheter was pulled backward by 5–10 mm from its original position, it was 0.26 ± 0.10 (3 ml/s IR). Catheter positions that were rated optimal during the perfusion studies (Chapter 4) had, in this retrospective analysis, CCDR values closer to one.

Figure 5.4 shows segmentations of the CCA and extracted time-intensity curves from one pig with different injection catheter locations. Quantitative results for this example were CCDR = 1.03 (top row) and CCDR = 0.36 (bottom row). While the catheter position in the upper image provides uniform contrast agent bolus distribution, the catheter position in the bottom image results in a non-uniform bolus distribution.

5.4 Discussion and Conclusion

A novel algorithm has been presented for automatic quantitative evaluation of contrast agent distribution in the CCAs after a test bolus injection using time-resolved 2-D DSA images. This algorithm includes an automatic segmentation of the CCAs and an automatic image analysis to compute relevant parameters of the contrast agent volume distribution. The results of this study show that the contrast agent is uniformly distributed (mean relative difference $\leq 10\%$) into the CCAs if the injection location is selected properly. Additional evaluations that will contribute to a larger sample size may be necessary to further validate this hypothesis.

Therefore, IA injections at the root of the aortic arch can be considered as a potential injection approach in perfusion C-arm CT imaging. It can provide higher

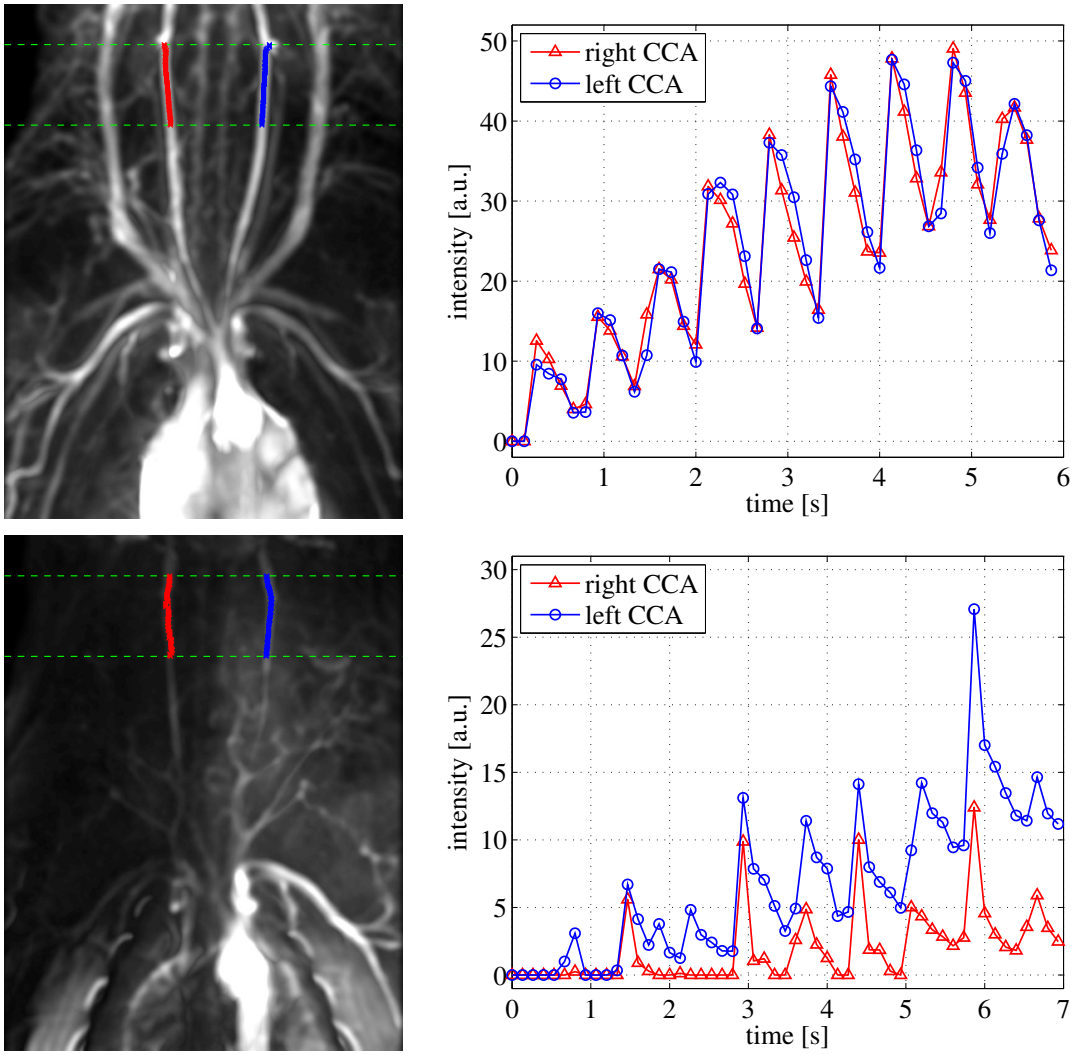

Figure 5.4: Segmentation of the two common carotid arteries (CCA) and plot of the time-intensity curve extracted from the CCAs. The segmentation is overlayed on a temporal maximum intensity projection of the 2-D DSA data set. The top images correspond to an optimal injection catheter position whereas the bottom images correspond to a non-optimal position.

contrast agent enhancement levels in the brain, thus a higher SNR of the measured TACs, compared to an IV injection. Alternatively, the amount of injected contrast agent can be reduced while providing a similar SNR as an IV injection.

Beside a retrospective evaluation, this novel method could also help to optimize the catheter placement for arterial injections in perfusion C-arm CT imaging *during* stroke therapy by providing additional quantitative parameters. In fact, the method is robust, fast, user-independent and would not require extra X-ray or iodine dose compared to the current protocols which already use a test bolus injection with a pure visual assessment of the contrast agent flow.

Chapter 6

Practical Aspects Regarding C-arm CT Perfusion Imaging

Overview:
This chapter covers two aspects that have been identified to be practically relevant when CT-like perfusion imaging is to be implemented using C-arm CT. The first part of this chapter addresses fundamental C-arm CT image quality measurements. In order to investigate the feasibility of C-arm CT for perfusion imaging, the linearity of contrast agent concentration and measured X-ray attenuation was verified. The measurements were performed using the same C-arm CT system as for acquiring the *in vivo* data in Chapter 4. As part of the work on this thesis, a software program was developed to implement a complete perfusion imaging workflow with C-arm CT. In the second part of this chapter, this program is described and an overview of the corresponding workflow is given. The program implements the algorithms from Chapters 2 and 4.

Section 6.1 of this chapter is based on "Using a C-arm CT for interventional perfusion imaging: a phantom study to measure linearity between iodine concentration and Hounsfield values", by A. Fieselmann, A. Ganguly, Y. Deuerling-Zheng, J. Boese, R. Fahrig, and J. Hornegger. In *Proc. Annual Meeting DGMP 2010*, Freiburg i. Br., Germany, 2010. [31].

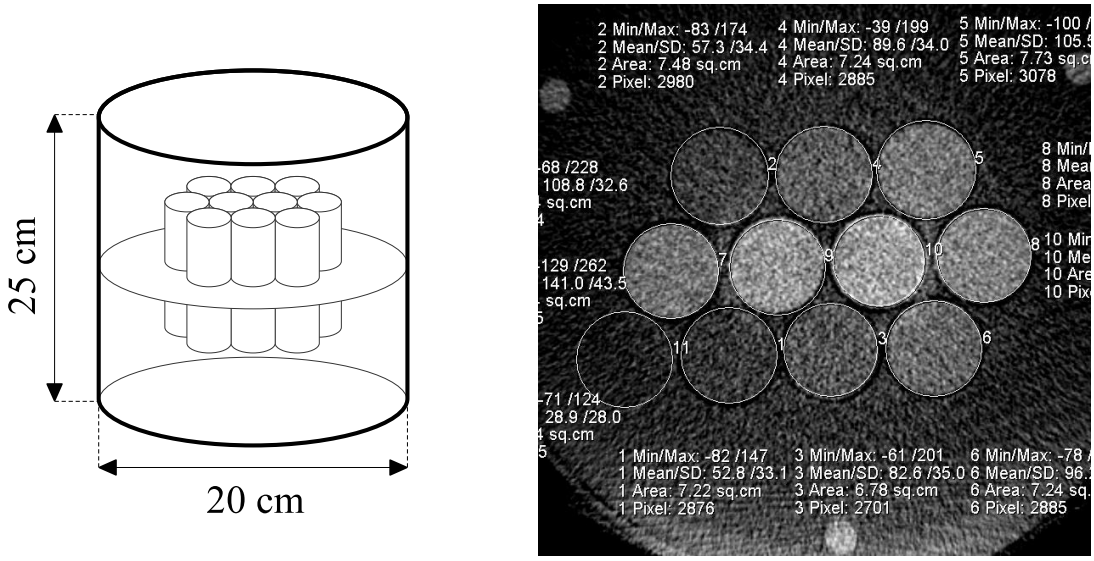

(a) drawing of the phantom

(b) C-arm CT scan of the phantom

Figure 6.1: (a) Drawing of the phantom used for the measurements. (b) Axial C-arm CT scan of the phantom with circular ROIs drawn around the contrast-filled containers (the bottom left ROI is a reference ROI in water).

6.1 Quantification of Iodine Concentration Using C-arm CT

6.1.1 Introduction

This chapter is concerned with fundamental C-arm CT image quality measurements regarding the image-based quantification of iodine concentration. As it has been explained in Section 2.4.4, a linear relationship between the underlying iodine concentration and the measured X-ray attenuation value is assumed for CT perfusion imaging. This linearity has been verified for conventional MSCT scanner [99]. In this chapter, investigations were carried out in order to verify this linearity for a clinical C-arm CT system; the linearity is a necessary pre-condition for C-arm-CT-based perfusion imaging with the standard image analysis methods.

6.1.2 Material and Methods

A cylindrical phantom was built using perspex which contained smaller cylindrical containers of about 3 cm diameter (Figure 6.1(a)). It was similar to a phantom previously described in [100] that was used for image quality measurements using CT. The diameter of the phantom was about 20 cm and its height was about 25 cm. The containers were filled with different dilutions of deionized water and contrast agent (350 mg iodine per ml). Water was filled into the phantom body such that all containers were submerged.

In order to study the relationship of HU values and iodine concentrations in the low concentration range, ten containers were filled with dilutions containing 0.1%

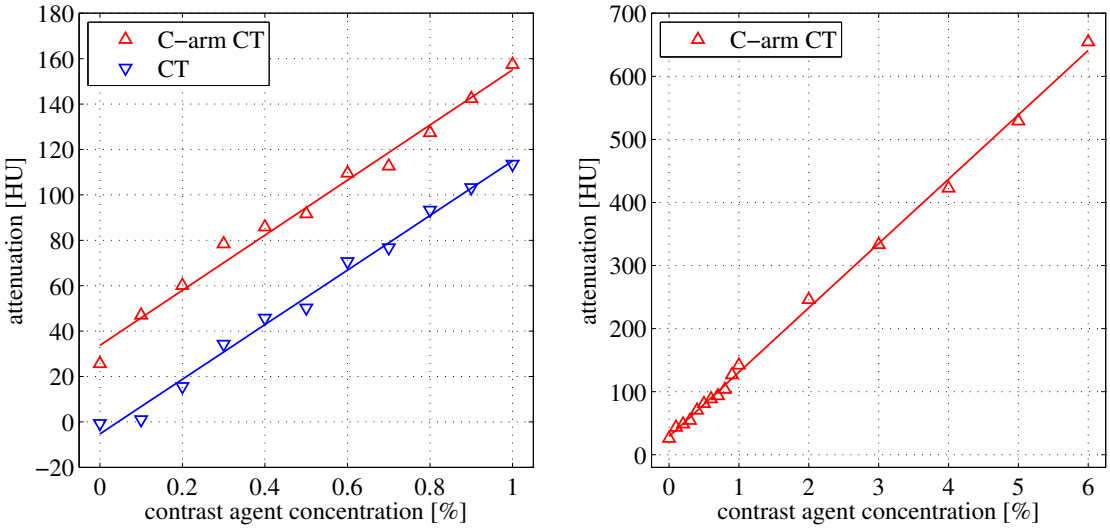

(a) low concentration range

(b) low and high concentration range

Figure 6.2: Plot of the measured attenuation value in the ROI as a function of the contrast agent concentration.

to 1.0% (in steps of 0.1%) of contrast agent using milliliter syringes. The phantom was scanned in four different orientations, obtained by rotation of the phantom by 90° around its longitudinal axis, using a clinical C-arm CT system (Artis *d*TA with syngo DynaCT, Siemens AG, Healthcare Sector, Forchheim, Germany). This was the same system which was also used for the investigations in Chapter 4. Note, it had undergone routine calibration before conducting the measurements. A protocol with a fast C-arm rotation speed (4.3 seconds per 190°) was chosen which was also used for experimental perfusion studies, see again Chapter 4. This protocol acquired 191 projection images using a X-ray tube voltage of 83 kV.

Mean HU values were determined inside circular ROIs that were drawn around the containers in a central slice of the reconstructed volume (Figure 6.1(b)). Finally, the mean HU values were averaged over the measurements from the four different orientations. The C-arm CT phantom measurement were compared with measurements using a clinical CT scanner (Somatom Definition, Siemens AG, Healthcare Sector, Forchheim, Germany).

To study the relationship of HU values and iodine concentrations in the high concentration range the ten original containers were replaced with six containers that were filled with dilutions containing 1.0% to 6.0% (in steps of 1.0%) of contrast agent. The measurements with the six containers were repeated as described above.

6.1.3 Results

The results from the C-arm CT and CT measurements of the low concentration range are shown in Figure 6.2(a). There is a very high linear correlation (C-arm CT: $r_{\text{corr}} = 0.993$, $p < 0.001$; CT: $r_{\text{corr}} = 0.996$, $p < 0.001$) between the contrast concentration and the measured attenuation values. The slopes of the regression lines are very similar (121 HU/% in C-arm CT and 120 HU/% in CT). The regression line

of the C-arm CT data has an initial offset of 39 HU with respect to the regression line of the CT data. Figure 6.2(b) shows the measurements of the low and high concentration range using C-arm CT. The linear correlation between the contrast agent concentration and the measured attenuation value is again very high ($r_{\text{corr}} = 0.999$, $p < 0.001$).

6.1.4 Discussion and Conclusion

The measured data show very high linear correlation. For comparison, similar measurements were carried out in [149] using a micro-CT system and a correlation value of $r_{\text{corr}} = 0.9998$ has been obtained. This linear relationship is a pre-requisite when using the standard mathematical models to compute perfusion parameters (Chapter 2). The actual slope and the offset of the concentration-attenuation curve do not influence the computed perfusion values due to the normalization of the tissue time curves with the arterial time curve and the subtraction of baseline time frames (Section 2.4.4).

Generally, the results shown in this chapter may also be of interest for other potential applications of contrast-enhanced imaging with a C-arm CT system. For example, various CT applications in tumor diagnosis based on measurement of iodine concentrations have been described [100]. An application of C-arm CT to measure iodine concentration in the liver was suggested in [150].

To conclude, the results for the given clinical C-arm CT system show that the assumption of linearity between iodine concentration and measured attenuation values holds. Thus, no pre-correction of the measured data is necessary and standard mathematical models can be used to compute tissue perfusion parameters from the reconstructed C-arm CT data.

6.2 Description of a Software Program for C-arm CT Perfusion Imaging

In this section, a software program will be described that was developed as part of the work on this thesis. This program was designed for two tasks.

1. It should be used for experimental evaluation of the algorithms from Chapters 2 and 4 with real C-arm CT data. For example, different reconstruction and post-processing strategies can be implemented and evaluated by a technical expert user.

2. This program should also be used for evaluation of C-arm CT perfusion imaging in a realistic clinical environment, where it will be used by biomedical researchers or physicians.

6.2.1 Workflow

The two aforementioned tasks lead to different requirements for this software program. For experimental evaluations, the program is required to be designed such that

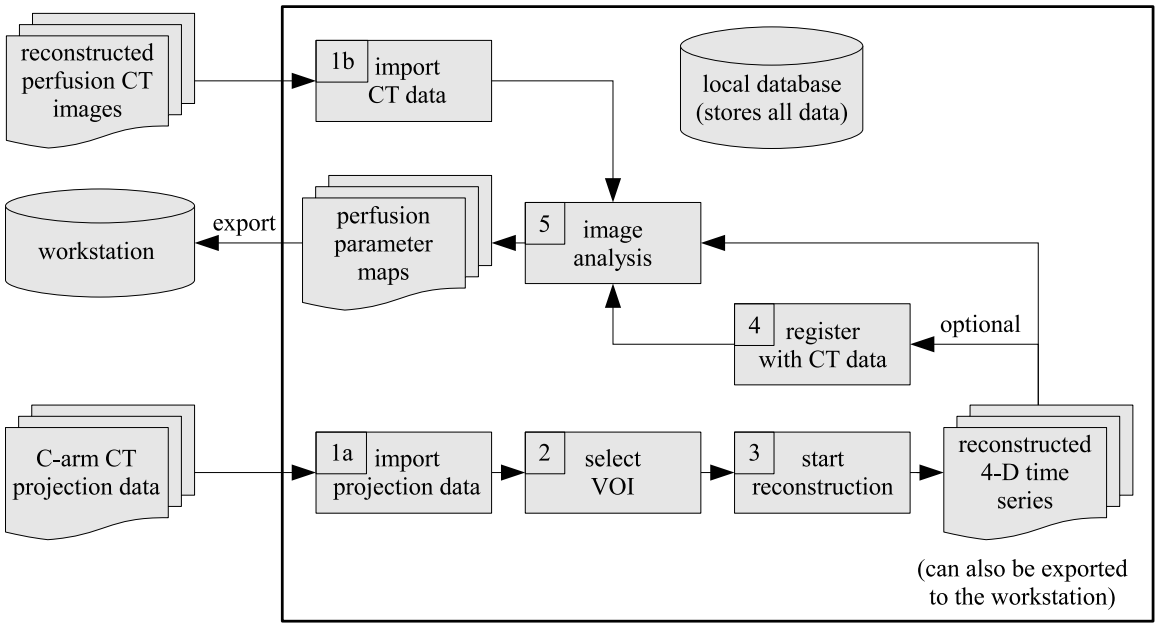

Figure 6.3: Workflow for processing the perfusion C-arm CT data.

it is flexible and user-configurable. On the other hand, for its evaluation in a realistic clinical environment — during the work on this thesis, *in vivo* animal studies were performed but patient studies are expected to be conducted in the future — a minimal amount of user interaction is desirable [151]. In order to fulfill both requirements, the program has been designed such that almost each step of the workflow (Figure 6.3) can be automated but, nevertheless, user interaction to change various parameters is also possible. The program runs on a dedicated workstation (syngo X-Workplace, Siemens AG, Healthcare Sector, Forchheim, Germany) for post-processing of medical imaging data. For processing the data, the C-arm CT projection data from an interleaved scanning protocol must be transfered to the workstation first. This data is stored in the DICOM (digital imaging and communications in medicine) file format. These files can be sent directly from the C-arm CT system to the workstation. The workflow for processing the perfusion C-arm CT data is described next.

Step 1a: Import of projection data

The program automatically scans a pre-defined import directory for C-arm CT projection data files. Using the DICOM information, it can identify the order of the data within the IS scanning protocol. Currently, the scanning delay τ_n of the n-th interleaved sequence (Equation (4.1)) is not stored in these files and it must be entered manually using a graphical user interface (GUI). However, in the future this information could be stored in the DICOM file as well; thus, no user interaction would be necessary. The imported projection data are stored in a local database of the software program.

Step 2: Selection of a VOI for reconstruction

In this step, the user may define a VOI (number of voxels, voxel spacing, center of VOI) for the image reconstruction. To this end, two multi-planar reconstruction (MPR) views of an initial reconstruction of one volume at a low spatial resolution are displayed where the VOI can be placed interactively. The selection of a smaller VOI can reduce the processing time while focusing on the actual volume of interest. If no user interaction is desired, default values for the VOI can be used.

Step 3: Image reconstruction

The user can select various reconstruction parameters (e.g., number M of angular interpolation intervals) before starting the reconstruction. In order to examine reconstructions from different sets of parameters, several reconstruction tasks can be defined before these tasks are executed as a batch process. If no user interaction is desired, a set of default parameters can be used.

Step 4: Registration with CT data

This step is optional. The software program offers the possibility to register the reconstructed C-arm CT data to a CT data set. This allows for better comparison of the perfusion C-arm CT parameter maps with those from a perfusion CT scan which was acquired before the intervention or study. In order to conduct the registration, the CT data must be imported into the program first (step 1b in Figure 6.3) using a graphical user interface.

Step 5: Image Analysis

In this step, the user can inspect the reconstructed time-attenuation curves using a dedicated GUI (Figure 6.4(b)). Both, the reconstructed perfusion C-arm CT data and the perfusion CT data, can be analyzed. For comparison of perfusion C-arm CT parameter maps with those from perfusion CT scan, it is actually desirable to use the same processing software for the image analysis [81]. When moving the mouse cursor inside the image area (left side of the GUI), then the time-attenuation curve at the corresponding voxel position is plotted (right side of the GUI). This GUI is also used to select the position of the AIF that is necessary for the computation of the parameter maps (Section 2.3.1). In the future the AIF position may also be determined automatically to further automate this step; thus, no user interaction would be necessary (Section 2.4.6).

After the image analysis, the computed parameter maps can be exported without any user interaction from the software program to the workstation (X-workplace). This workstation offers various means to visualize the perfusion parameter maps.

6.2.2 Implementation

The software program is implemented in the C++ programming language. It uses several open source software libraries. The most relevant libraries are listed below.

- **Insight Toolkit (ITK)** [152, 153]: This library is used for various medical image processing tasks in the image reconstruction step (Chapter 4) and the image analysis step (Section 2.3) such as data interpolation, noise reduction and segmentation.
- **Visualization Toolkit (VTK)** [154]: This library is used for visualization of the reconstructed C-arm CT data. For example, MPR views can be displayed for the selection of the VOI or reconstructed time-attenuation curves can be inspected in a dedicated GUI (Figure 6.4(b)).
- **DICOM Toolkit (DCMTK)** [155]: This library is used for handling of the DICOM files. For example, the dicom tags of the reconstructed 4-D C-arm CT data must be set correctly such that it can be exported to the workstation.
- **Fox Toolkit** [156]: This library is used for the implementation of the GUI (Figure 6.4).

Furthermore, the software program uses a few libraries that, for example, implement common C-arm CT pre-processing routines [13] which are property of Siemens AG and are not publicly available.

The backprojection step during the image reconstruction [15] is implemented on the graphics card using the compute unified device architecture (CUDA) [157] to achieve a higher computational speed when compared to an implementation on the central processing unit (CPU) [114]. The motion correction step (Section 2.4.1) is implemented using an image registration algorithm that is based on mutual information (MI) [158].

Figure 6.3 shows two examples of the GUI of the software program. In Figure 6.4(a) the patient browser is depicted. This browser acts as an interface to the database of the program. For a given VOI definition, several reconstruction can exist which were generated using different sets of reconstruction parameters. This is useful to, for example, compare different reconstruction parameters such as the number M of angular interpolation intervals or the number N_{seq} of interleaved sequences (Section 4.3). In the patient browser, the different reconstructions are organized as child nodes of the VOI definition.

The GUI for displaying the reconstructed time-attenuation curves of the 4-D data set is shown in Figure 6.4(b). The user can select different visualization options. For example, baseline frames can be subtracted or a temporal MIP can be displayed.

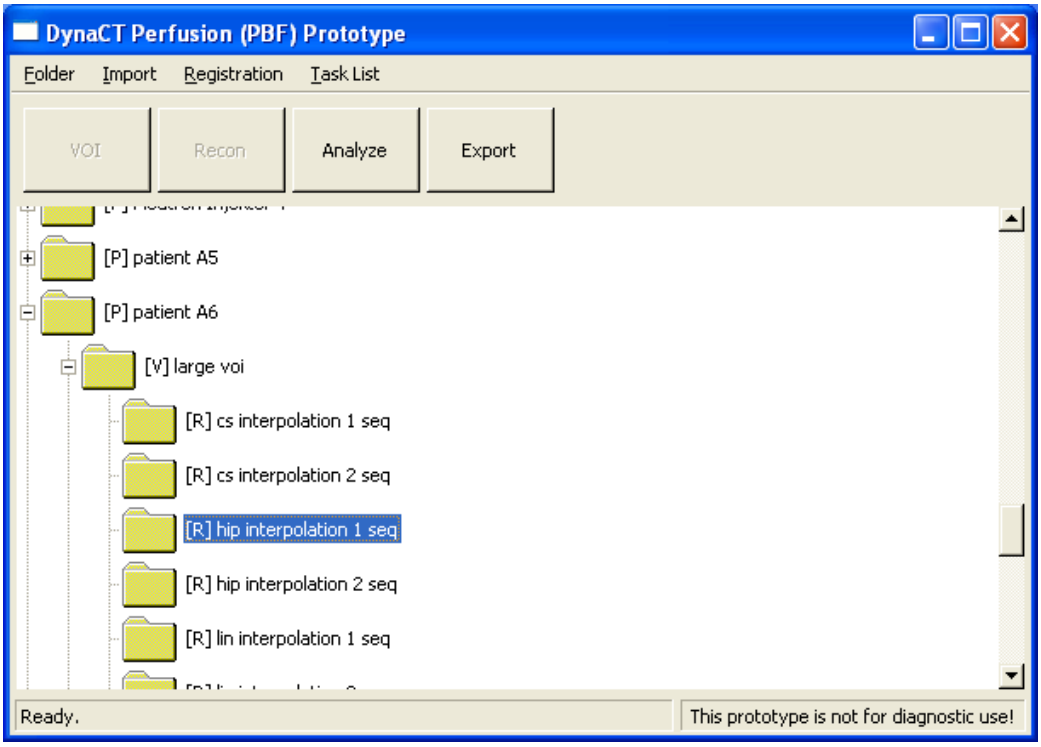

(a) patient browser

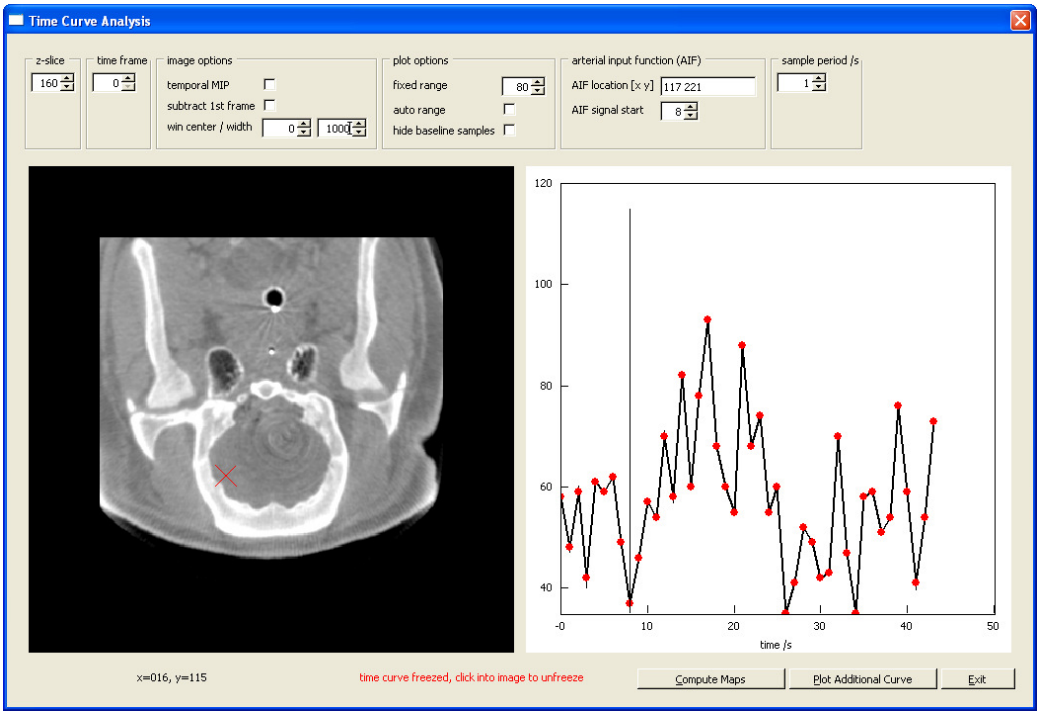

(b) time curve viewer

Figure 6.4: Examples of the graphical user interface of the software program.

Chapter 7

Summary and Outlook

7.1 Summary

Functional imaging modalities for brain perfusion measurement, such as perfusion CT and perfusion MRI, have been around for many years already. However, they are restricted to purely diagnostic imaging and cannot be used for perfusion measurement during an intervention; for example, when ischemic stroke is treated.

In this thesis, a promising new functional imaging modality — perfusion C-arm CT — was investigated that overcomes this limitation and provides technical means for a more effective stroke treatment. It is conducted using an interventional C-arm angiography system. Nowadays, these systems constitute an integral part of catheter-guided stroke therapy procedures. Their main application is to provide 2-D images for catheter guidance, but also 3-D imaging (C-arm CT) is possible using these systems. Using C-arm CT for 4-D imaging of dynamic perfusion had, in fact, been suggested prior to the start of this thesis already. However, only basic theoretical simulations had been carried out at that time.

As part of the work on this thesis, the first *in vivo* measurements of dynamic perfusion (cerebral blood flow) using C-arm CT were conducted and the feasibility of this new functional imaging modality could be demonstrated. Since perfusion C-arm CT imaging is still a novel field of research, this thesis could address several different new scientific topics which are relevant for perfusion C-arm CT imaging. Image reconstruction and image analysis topics were covered, but also new injection protocols were investigated and fundamental image quality measurements were carried out.

In the introduction of this thesis (**Chapter 1**), a description of the state-of-the-art stroke management workflow and a new stroke management protocol using interventional perfusion imaging were presented. This protocol could lead to faster and also more reliable stroke treatment. Next, a summary of C-arm CT imaging and a brief overview of the two major challenges of perfusion C-arm CT imaging that had been identified were given. First, the comparably long C-arm rotation time causes a low temporal sampling frequency and, second, since the acquired data is inconsistent due to the time-varying attenuation values caused by the contrast agent flow, image reconstruction artifacts can arise.

The following chapter (**Chapter 2**) provided a review of the state-of-the-art image analysis methods for perfusion quantification using CT or MRI. This review was focused on deconvolution-based methods which are employed most frequently. The existing methods from perfusion CT and perfusion MRI can be applied in an equivalent way to the reconstructed data from perfusion C-arm CT imaging. Therefore, these image analysis methods were also used to compute the perfusion parameters from the simulated and measured C-arm CT data that have been presented in this thesis. Compared to previous reviews in this field, this chapter established a direct link between the theoretical physiological model of capillary blood flow and the actual practical computer implementation. In particular, the necessary simplifications of the model such that it can be used with real data were highlighted.

Chapter 3 was concerned with one of the two major challenges that had been stated before: image reconstruction artifacts can arise due to the varying attenuation values during the time of one C-arm rotation (typically 3–5 seconds for 200°). For example, if the contrast agent concentration inside an arterial vessel varies while the projection data are acquired, an artifact around this vessel will appear in the reconstructed image. This artifact can lead to incorrectly computed perfusion parameters in the tissue region around the artery. In this chapter, this kind of artifact was investigated for the particular case of the filtered backprojection (FBP) reconstruction. This analytical and computationally fast image reconstruction method is the most commonly employed method in (C-arm) CT imaging. Interestingly, this kind of reconstruction artifact has already been described in the late 1970s, at a time when CT scanners used lower rotation speeds, but no dedicated model of these artifacts had existed so far.

The intention of this theoretically oriented chapter is to better understand these artifacts and to systematically investigate corresponding artifact reduction strategies. A novel spatio-temporal artifact model was derived by a mathematical analysis of the FBP algorithm. The novel concept of derivative-weighted point spread functions (DWPSF) — these are computed from the scanning and reconstruction parameters — was introduced in order to describe the spatial spread of the artifacts. The DWPSFs are weighted with the derivative values of the time-attenuation curve and the C-arm rotation speed. The model was validated quantitatively using numerical simulations (0.3–1.1 HU root mean squared deviations) and qualitatively using data of a flow phantom that had been scanned using a clinical C-arm CT system. The measured artifacts could be explained very well by the artifact model.

Furthermore, artifact reduction strategies were investigated for future C-arm CT systems that would be able to perform continuous, uni-directional C-arm rotations. It could be shown that with optimized redundancy weighting function parameters the spatial spread of the artifacts around a typical arterial vessel can be reduced by about 70%. Finally, an inversion of the artifact model could be used as the basis for novel dynamic reconstruction algorithms that further minimize these artifacts.

The main practical contribution of this thesis was presented in **Chapter 4**. This chapter dealt with a novel combined scanning and reconstruction approach for C-arm CT perfusion imaging. Using this approach, both challenges in perfusion C-arm CT imaging, the low temporal sampling frequency and the image reconstruction artifacts, can be tackled. The temporal sampling frequency is increased by using interleaved

scanning (IS) which involves several multi-rotational scan sequences, each being accompanied by a new contrast agent bolus injection. Each sequence has a different temporal delay between the start of injection and the start of scanning. Thus, for each interleaved sequence, samples of the time-attenuation curve are acquired at different relative time points after the injection.

The reconstruction artifacts due to inconsistent data can be reduced by partial reconstruction interpolation (PRI). To this end, a complete and consistent set of projection data, which corresponds to a particular time point, is estimated by temporal interpolation of the available projection data at earlier and later time points. The interpolation is not done in projection space but partially backprojected volumes are considered in order to increase the computational speed. A Feldkamp-type image reconstruction algorithm is applied to generate these partially backprojected volumes. This analytical algorithm can be implemented such that it is computationally very fast, which is inevitable for its use in interventional perfusion imaging during stroke treatment.

The combination of IS and PRI, denoted as IS-PRI, was evaluated with simulations and an *in vivo* study in 5 healthy pigs. In the simulations, the cerebral blood flow values (unit: ml/100g/min) were 60 (healthy tissue) and 20 (pathological tissue). For one scan sequence the values were estimated with standard deviations of 14.3 and 2.9, respectively. For two interleaved sequences the standard deviations decreased to 3.6 and 1.5, respectively. Perfusion CT was used to validate the *in vivo* results. With two interleaved sequences promising correlations ranging from $r_{\text{corr}} = 0.63$ to $r_{\text{corr}} = 0.94$ were achieved. The results suggest that C-arm CT tissue perfusion imaging is feasible with two interleaved scan sequences already.

The IS-PRI approach assumes that consecutive contrast agent bolus injections lead to similar contrast agent flow patterns in the brain. In order to promote that this assumption is valid, a contrast bolus injection at the aortic arch has been applied during the *in vivo* studies. The shorter traveling time to the brain, when compared to an intra-venous injection, reduces the influence of physiological variations such as the heart rate. Additionally, the contrast-to-noise ratio in the reconstructed images is increased because a higher fraction of contrast agent actually arrives in the brain. It is, however, required that equal amounts of contrast agent flow into both common carotid arteries (CCA) in order to compare perfusion between the left and right hemispheres.

To address this requirement, in **Chapter 5** a novel method to quantify the contrast agent bolus distribution between the two CCAs was presented. It is a fully automatic method that uses 2-D digital subtraction angiography (DSA) images following a test bolus injection. Both CCAs are segmented using a dedicated spatio-temporal weighting and the relative contrast agent distribution is computed. The method was tested on DSA data sets from 5 healthy pigs, the same that were used for the investigations in the previous chapter, and it achieved successful segmentation of both CCAs in all data sets. The results showed that the contrast agent is uniformly distributed (mean relative difference less or equal than 10%) if the injection location is properly chosen.

The following chapter of this thesis, **Chapter 6**, addressed two further topics in perfusion C-arm CT imaging that were identified to be practically relevant. In Sec-

tion 6.1, image quality measurements were conducted to verify the linearity between the measured X-ray attenuation values and underlying contrast agent concentration. The results showed a very high linear correlation ($r_{\text{corr}} \geq 0.993$) which, in fact, is a requirement when standard image analysis methods are to be applied to the measured data. In Section 6.2, a software program was described that had been developed as part of the work on this thesis. It implements the workflow of a complete perfusion C-arm CT examination including image reconstruction and image analysis. Furthermore, it can be used for clinical studies and it has, for example, the capability to perform 4-D image registration with a reference perfusion CT scan.

In summary, through the methods developed, the measurements conducted and results obtained, this thesis made a number of significant and original contributions, both on a practical and on a theoretical level, to the novel and highly relevant research field of interventional C-arm CT perfusion imaging. For the first time, the feasibility of perfusion C-arm CT imaging could be demonstrated using *in vivo* data. Based on this work, optimized stroke treatment in the interventional suite could be available in a few years and provide better care for stroke patients.

7.2 Outlook

This thesis is the first comprehensive work on C-arm CT perfusion imaging. Naturally, further research in this field is possible and will be conducted in the future.

Future research may focus on reducing the amount of contrast agent and X-ray radiation that is applied to the patient. This could be accomplished by new image reconstruction algorithms or new C-arm CT system technologies. New iterative model-based image reconstruction algorithms (Section 4.1.2) could potentially be used for perfusion imaging. With these algorithms, the computational complexity is currently the main limiting factor, but advances in computer hardware may make this approach become feasible. New iterative approaches based on compressed sensing with a prior image [159, 160] could be used to lower the radiation dose by acquiring less projections and exploiting correlations between the individual time frames. When considering only projection data from a limited angular interval, the temporal resolution of the reconstructed data could be improved (Section 4.1.2). However, it is required that small attenuation value changes due to contrast agent flow in tissue are still noticeable when considering less projection data.

Besides algorithmic advances, new C-arm CT system hardware could lead to new scanning approaches. The sliding-window reconstruction approach with optimized windowing function, presented in Chapter 3, could be implemented with a (quasi-)continuously rotating C-arm CT system. Such a device could be realized if a robotic C-arm CT system (Figure 1.3(b)) was equipped with slip-ring technology [161], mainly to accomplish the electrical power supply, or a device for winding the supply cable around one axis [162]. A biplane C-arm CT system (Figure 1.3(c)) that was capable of acquiring projection data with both planes could be used to conduct an interleaved-scanning-type protocol with only one contrast agent bolus injection (Section 4.4.3).

Finally, also different applications for interventional perfusion imaging — besides cerebral perfusion imaging for stroke diagnosis — are possible. Perfusion C-arm CT imaging of the liver, for example, could enhance certain hepatic interventional procedures, such as intra-arterial embolization [9, 163].

Appendix A

Algebraic Deconvolution with a Block-circulant Matrix

The matrix $\boldsymbol{A}$ in Equation (2.31) can be replaced by a block-circulant matrix $\boldsymbol{A}_{\text{circ}}$ to reduce the influence of the bolus delay, cf. Section 2.3.1, and thus to become independent of time shifts in the tissue TCC. Several studies actually exhibited an improvement of the accuracy of the perfusion estimates when using this alternative discretization method compared to the approach given by Equation (2.29) [59, 60, 164]. On the other hand, in a receiver operating characteristics analysis — concerning infarct prediction in acute stroke patients — both discretization methods led to almost equal results [48].

The elements $a_{i,j}$ of $\boldsymbol{A} \in \mathbb{R}^{N\times N}$ — with i denoting the row index ($i = 1, \ldots, N$) and j denoting the column index ($j = 1, \ldots, N$) as usual — are defined as

$$a_{i,j} = \begin{cases} \Delta t\, c_{\text{art}}(t_{i-j+1}) & \text{for } j \leq i\ , \\ 0 & \text{for } j > i\ , \end{cases} \tag{A.1}$$

see Equation (2.30). In order to assemble the block-circulant matrix $\boldsymbol{A}_{\text{circ}}$, the size of the time series $c_{\text{art}}(t_j)$ must be increased from N to M ($M \geq 2N$) using zero-padding. The the new zero-padded time series is denoted as $c_{\text{art,pad}}(t_j)$ The size of $c_{\text{voi}}(t_j)$ must be changed accordingly in order to retain consistency in Equation (2.31).

The elements $(a_{\text{circ}})_{i,j}$ of the block-circulant matrix $\boldsymbol{A}_{\text{circ}} \in \mathbb{R}^{M\times M}$ can then be defined as

$$(a_{\text{circ}})_{i,j} = \begin{cases} \Delta t\, c_{\text{art,pad}}(t_{i-j+1}) & \text{for } j \leq i\ , \\ \Delta t\, c_{\text{art,pad}}(t_{M+i-j+1}) & \text{for } j > i\ . \end{cases} \tag{A.2}$$

As an example, for $M = 2\,N$, the matrix $\boldsymbol{A}_{\mathrm{circ}}$ has the following structure:

$$\boldsymbol{A}_{\mathrm{circ}} = \Delta t \left(\begin{array}{cccc|cccc} c_{\mathrm{art}}(t_1) & 0 & \dots & 0 & 0 & c_{\mathrm{art}}(t_N) & \dots & c_{\mathrm{art}}(t_2) \\ c_{\mathrm{art}}(t_2) & c_{\mathrm{art}}(t_1) & \dots & 0 & 0 & 0 & \dots & c_{\mathrm{art}}(t_3) \\ \vdots & \vdots & \ddots & \vdots & \vdots & \vdots & \ddots & \vdots \\ c_{\mathrm{art}}(t_N) & c_{\mathrm{art}}(t_{N-1}) & \dots & c_{\mathrm{art}}(t_1) & 0 & 0 & \dots & 0 \\ \hline 0 & c_{\mathrm{art}}(t_N) & \dots & c_{\mathrm{art}}(t_2) & c_{\mathrm{art}}(t_1) & 0 & \dots & 0 \\ 0 & 0 & \dots & c_{\mathrm{art}}(t_3) & c_{\mathrm{art}}(t_2) & c_{\mathrm{art}}(t_1) & \dots & 0 \\ \vdots & \vdots & \ddots & \vdots & \vdots & \vdots & \ddots & \vdots \\ 0 & 0 & \dots & 0 & c_{\mathrm{art}}(t_N) & c_{\mathrm{art}}(t_{N-1}) & \dots & c_{\mathrm{art}}(t_1) \end{array}\right). \quad \text{(A.3)}$$

The horizontal and vertical lines drawn in Equation (A.3) subdivide the matrix into four quadrants. As can be seen, the matrix $\boldsymbol{A}$ is a submatrix of $\boldsymbol{A}_{\mathrm{circ}}$, and it appears in the upper left and lower right quadrant.

Appendix B

Derivation of Equations (3.11) and (3.12)

To derive Equation (3.11) and Equation (3.12), first the delta function in Equation (3.10) is evaluated using the identity

$$\int f(u)\,\delta(u^*(\boldsymbol{x},\lambda(t))-u)\,\mathrm{d}u = f(u^*(\boldsymbol{x},\lambda(t))) \tag{B.1}$$

and then the result is split into the following two functions:

$$\mu_{\mathrm{rec}}(\boldsymbol{r},t_{\mathrm{rec}}) = \iint \hat{\chi}(\boldsymbol{r},\boldsymbol{x},t_{\mathrm{rec}})\,\mathrm{d}x\,\mathrm{d}y \tag{B.2}$$

$$\begin{aligned}\hat{\chi}(\boldsymbol{r},\boldsymbol{x},t_{\mathrm{rec}}) = \int & \frac{R\,D^2}{(R-\boldsymbol{r}^{\mathrm{T}}\boldsymbol{e}_{\mathrm{w}}(\lambda(t)))^2}\,h_{\mathrm{ramp}}\Big(u^*(\boldsymbol{r},\lambda(t))-u^*(\boldsymbol{x},\lambda(t))\Big)\\ &\cdot\ \mu\Big(\boldsymbol{x},\lambda(t)\Big)\left((u^*(\boldsymbol{x},\lambda(t)))^2+D^2\right)^{-1/2}\\ &\cdot\ w_\Lambda\Big(\lambda(t)-\lambda(t_{\mathrm{rec}}),\arctan(u^*(\boldsymbol{x},\lambda(t))/D)\Big)\,\mathrm{d}t\ .\end{aligned} \tag{B.3}$$

By re-writing $\hat{\chi}(\boldsymbol{r},\boldsymbol{x},t_{\mathrm{rec}})$ such that it depends on the distance vector $\boldsymbol{s}=\boldsymbol{r}-\boldsymbol{x}$ the expressions shown in Equation (3.11) and Equation (3.12) are obtained.

Appendix C

Derivation of Equation (3.14)

It shall be proven that the n-th order total derivative of a function $\mu(\lambda(t))$, which has the property $\mathrm{d}^2\lambda/\mathrm{d}t^2 = 0$, is given by

$$\frac{\mathrm{d}^n\mu}{\mathrm{d}t^n} = \frac{\partial^n\mu}{\partial\lambda^n}\left(\frac{\mathrm{d}\lambda}{\mathrm{d}t}\right)^n . \tag{C.1}$$

Using the following definition

$$D_k \equiv \frac{\partial^k\mu}{\partial\lambda^k}\left(\frac{\mathrm{d}\lambda}{\mathrm{d}t}\right)^k . \tag{C.2}$$

and by applying the product rule of differentiation one gets

$$\frac{\mathrm{d}}{\mathrm{d}t}D_k = \frac{\mathrm{d}}{\mathrm{d}t}\frac{\partial^k\mu}{\partial\lambda^k}\left(\frac{\mathrm{d}\lambda}{\mathrm{d}t}\right)^k + \frac{\partial^k\mu}{\partial\lambda^k}\frac{\mathrm{d}}{\mathrm{d}t}\left(\frac{\mathrm{d}\lambda}{\mathrm{d}t}\right)^k . \tag{C.3}$$

The first term in Equation (C.3) can be re-arranged to

$$\begin{aligned}\frac{\mathrm{d}}{\mathrm{d}t}\frac{\partial^k\mu}{\partial\lambda^k}\left(\frac{\mathrm{d}\lambda}{\mathrm{d}t}\right)^k &= \frac{\partial^k}{\partial\lambda^k}\frac{\mathrm{d}\mu}{\mathrm{d}t}\left(\frac{\mathrm{d}\lambda}{\mathrm{d}t}\right)^k \\ &= \frac{\partial^k}{\partial\lambda^k}\left(\frac{\partial\mu}{\partial\lambda}\frac{\mathrm{d}\lambda}{\mathrm{d}t}\right)\left(\frac{\mathrm{d}\lambda}{\mathrm{d}t}\right)^k \\ &= \frac{\partial^{k+1}\mu}{\partial\lambda^{k+1}}\left(\frac{\mathrm{d}\lambda}{\mathrm{d}t}\right)^{k+1} \\ &= D_{k+1} .\end{aligned} \tag{C.4}$$

Re-writing the second term in Equation (C.3) gives

$$\frac{\partial^k\mu}{\partial\lambda^k}\frac{\mathrm{d}}{\mathrm{d}t}\left(\frac{\mathrm{d}\lambda}{\mathrm{d}t}\right)^k = \frac{\partial^k\mu}{\partial\lambda^k}\left(k\left(\frac{\mathrm{d}\lambda}{\mathrm{d}t}\right)^{k-1}\frac{\mathrm{d}^2\lambda}{\mathrm{d}t^2}\right) = 0 . \tag{C.5}$$

In the last equation it was used that the second order derivative of $\lambda(t)$ is zero. Combining Equation (C.3), Equation (C.4) and Equation (C.5) yields

$$\frac{\mathrm{d}}{\mathrm{d}t}D_k = D_{k+1} . \tag{C.6}$$

The n-th order derivative of D_k can be expressed by applying Equation (C.6) iteratively:

$$\frac{\mathrm{d}^n}{\mathrm{d}t^n} D_k = D_{k+n} \; . \tag{C.7}$$

Now, it can be shown that for $n \geq 1$ one gets

$$\frac{\mathrm{d}^n \mu}{\mathrm{d}t^n} = \frac{\mathrm{d}^{n-1}}{\mathrm{d}t^{n-1}} \frac{\mathrm{d}\mu}{\mathrm{d}t} = \frac{\mathrm{d}^{n-1}}{\mathrm{d}t^{n-1}} D_1 = D_{1+(n-1)} = \frac{\partial^n \mu}{\partial \lambda^n} \left(\frac{\mathrm{d}\lambda}{\mathrm{d}t} \right)^n \; , \tag{C.8}$$

which is the same expression as in Equation (C.1).

List of Figures

List of Tables

List of Algorithms

List of Symbols and Abbreviations

In this section, first a description of the notation will be provided followed by a list of the symbols and abbreviations.

In this thesis, scalars and scalar-valued functions are written in italic lower or upper case letters (e.g., μ, F). As an exception, if the variable is an abbreviation (e.g., CBF) then it is not written in italic letters. Vectors and vector-valued functions are written in italic bold lower case letters (e.g., $\boldsymbol{k}$). Matrices and matrix-valued functions are written in italic bold upper case letters (e.g., $\boldsymbol{A}$).

Symbols

$\boldsymbol{a}$	X-ray source location (Equation (3.1))
A	maximum enhancement (Section 3.4)
$\boldsymbol{A}$	matrix containing arterial input function values (Equation (2.31))
$\boldsymbol{A}_{\mathrm{circ}}$	$\boldsymbol{A}$ constructed as a block-circulant matrix (Equation (A.3))
c_{art}	contrast agent concentration at arterial inlet (Table 2.1)
$c_{\mathrm{art,pad}}$	zero-padded function c_{art} (Appendix A)
c_{max}	maximum contrast agent concentration (Section 2.2.4)
c_{ven}	contrast agent concentration at venous outlet (Equation (2.6))
c_{voi}	average contrast agent concentration within VOI (Equation (2.14))
$\boldsymbol{c}$	vector containing time-concentration curve values (Equation (2.31))
D	source-to-detector distance (Section 3.2)
$\boldsymbol{e}_{\mathrm{u}}, \boldsymbol{e}_{\mathrm{w}}$	unit vectors (Equations (3.3) and (3.4))
$f^{(\mathrm{tikh})}$	filter factors for Tikhonov regularization (Equation (2.37))
$f^{(\mathrm{tsvd})}$	filter factors for TSVD regularization (Equation (2.36))
F	volume flow (Table 2.1)
G	Gaussian-type function (Equation (5.2))
h_{cap}	PDF of transit times in capillary bed (Table 2.1)
h_{ramp}	ramp filter kernel (Section 3.2)
H	unit step function (Section 3.4)
k	flow-scaled residue function (Equation (2.18))
$\boldsymbol{k}$	vector containing flow-scaled residue function values (Equation (2.31))
$\boldsymbol{k}_l$	$\boldsymbol{k}$ computed using regularization (Tikhonov or TSVD) (Equation (2.35))
$\boldsymbol{k}_{\mathrm{ls}}$	$\boldsymbol{k}$ computed using least-squares approach (Equation (2.34))
K_{ct}	constant of proportionality between contrast agent concentration and X-ray attenuation values (Section 2.4.4)
K_{mr}	constant of proportionality between contrast agent concentration and received MR signal (Section 2.4.4)
l	absolute regularization parameter (Equation (2.38))

l_{rel}	relative regularization parameter (Equation (2.38))
L	number of view angles per partial backprojection (Section 4.2.3)
$m_{\mathrm{c,voi}}$	mass of contrast agent within VOI (Equation (2.5))
$m_{\mathrm{c,voi,in}}$	accumulated mass of contrast agent that entered VOI (Equation (2.3))
$m_{\mathrm{c,voi,out}}$	accumulated mass of contrast agent that left VOI (Equation (2.4))
m_{Λ}	redundancy weighting function for interval length Λ (Equation (3.9))
M	number of angular interpolation intervals (Section 4.2.3)
N_{detpix}	number of detector pixels (Table 3.1)
N_{lz}	number of leading zeros in a time series (Section 2.3.2)
N_{rot}	number of C-arm rotations (Section 4.2.1)
N_{seq}	number of interleaved sequences (Section 4.2.2)
N_{tp}	number of interpolation time points (Algorithm 4.1)
N_{views}	number of views per C-arm rotation (Table 3.1)
N_{vox}	number of voxels (Algorithm 2.1)
p	measured projection value (Section 3.2)
$\tilde{p}$	estimated projection value (Equation (4.3))
$\hat{p}$	bi-linear interpolation of pre-processed projection values (Section 4.2.3)
p_{cvm}	contrast agent volume map (Equation (5.8))
p_{sub}	baseline-subtracted projection value (Section 5.2.1)
p_{tMIP}	temporal maximum intensity projection of p_{sub} (Section 5.2.2)
$p^{\mathrm{w}}_{\mathrm{tMIP}}$	p_{tMIP} weighted with w_{cmb} (Section 5.2.2)
P_n	n-th order DWPSF (Equation (3.17))
P_{static}	PSF characterizing scanning and reconstruction of a static point object (Section 3.3)
$\mathcal{P}$	set of projection data (Equation (4.4))
r	residue function (Equation (2.2))
$\hat{r}$	rank of $\boldsymbol{A}$ (Section 2.3.2)
r_{corr}	linear correlation coefficient (Section 4.4.1)
$r_{\mathrm{pha,art}}$	radius of artery in mathematical phantom (Section 3.4.1)
$r_{\mathrm{pha,head}}$	radius of head in mathematical phantom (Section 3.4.1)
R	source-to-isocenter distance (Section 3.2)
s_{mr}	received MR signal (Section 2.4.4)
$s_{\mathrm{mr},0}$	baseline value of s_{mr} (Equation (2.43))
S_n	weighted spatial spread of P_n (Section 3.30)
t_0	bolus arrival time (Section 4.3.1)
t_{c}	constant temporal offset (Equation (4.1))
t_{est}	interpolation time point (Section 4.2.3)
t_{max}	time-to-peak value (Section 5.2.2)
$t_{\mathrm{max,cca}}$	measured average time-to-peak of TACs inside CCAs (Section 5.2.3)
$t_{\mathrm{max,e}}$	expected time-to-peak value (Section 5.2.2)
t_{rec}	time point associated with reconstruction (Equation (3.7))
T_{inj}	duration of contrast agent bolus injection (Section 5.2.2)
T_{rot}	time per C-arm rotation (Table 3.1)
T_{w}	waiting time between C-arm rotations (Section 4.2.1)
$T_{\mathrm{wash,in}}$	duration of contrast agent wash-in phase (Section 5.2.3)
TE	echo-time of MR sequence (Section 2.4.4)

u, v	coordinates on flat-detector(Section 3.2)
u^*	u-coordinate of intersection of X-ray and detector (Equation (3.5))
u_0	center coordinate of detector along u-coordinate (Section 5.2.2)
$\boldsymbol{u}_i, \boldsymbol{v}_i$	i-th singular vector contained in $\boldsymbol{U}$ and $\boldsymbol{V}$ (Equation (2.33))
U	width of detector (Section 5.2.2)
$\boldsymbol{U}, \boldsymbol{\Sigma}, \boldsymbol{V}$	matrices corresponding to SVD of $\boldsymbol{A}$ (Equation (2.33))
v^*	v-coordinate of intersection of X-ray and detector (Section 4.2.3)
$v_{\mathrm{max,cran}}$	v-coordinate at the cranial end of projection image (Section 5.2.2)
$\mathcal{V}_{\mathrm{cap}}$	volume of capillary bed (Table 2.1)
$\mathcal{V}_{\mathrm{voi}}$	volume of VOI (Table 2.1)
$\mathcal{V}^*_{\mathrm{voi}}$	volumes of parenchyma and interstitial space (Table 2.1)
$\mathcal{V}_{\mathrm{vox}}$	volume of voxel (Section 2.3.1)
$\hat{w}$	distance weighting function (Section 4.2.3)
w_Λ	angular sliding window function of length Λ (Equation (3.8))
w_{cmb}	combined weighting function (Section 5.2.2)
w_{spt}	spatial weighting function (Section 5.2.2)
w_{tmp}	temporal weighting function (Section 5.2.2)
α, β	shape parameters of gamma-variate function (Section 3.4)
γ	fan-angle (Section 3.2)
γ_{m}	full fan-angle (Section 3.2)
δ	Dirac delta function (Section 2.2.1)
$\Delta\lambda$	view-angle increment (Table 3.1)
$\Delta\mu_{\mathrm{art}}$	difference of attenuation value in an artery (Equation (4.12))
$\Delta\mu_{\mathrm{tis}}$	difference of attenuation value in tissue (Equation (4.13))
Δt	sampling period (Section 2.3.2)
Δu	detector pixel size (Table 3.1)
η	time scaling factor (Section 4.3.1)
κ	hematocrit correction factor (Section 2.4.5)
λ	view-angle (Equation (3.2))
λ_0	starting view-angle (Equation (3.2))
λ_{rec}	view-angle associated with reconstruction (Section 3.3)
Λ	angular interval length (Section 3.2)
μ	X-ray attenuation value (Section 2.4.4)
μ_0	baseline value of X-ray attenuation (Equation (2.41))
μ_{art}	arterial time-attenuation curve (Section 2.3.2)
μ_{mdl}	reconstruction of μ_{pha} using artifact model (Section 3.4.1)
μ_{pha}	attenuation values of mathematical phantom (Section 3.4.1)
$\mu_{\mathrm{pha,art}}$	change of attenuation values inside artery in mathematical phantom (Section 3.4.1)
μ_{rec}	reconstructed pixel value (Equation (3.7))
μ_{sim}	FBP reconstruction of μ_{pha} (Section 3.4.1)
μ_{voi}	time-attenuation curve measured in VOI (Section 2.3.2)
μ_{w}	X-ray attenuation value of water (Section 3.4)
φ	interpolation function (Section 4.2.3)
Π_n	absolute amplitude of P_n (Equation (3.25))
ρ_{voi}	mean density of the volume $\mathcal{V}_{\mathrm{voi}}$ (Table 2.1)

ρ^*_{voi}	mean density of the volume $\mathcal{V}^*_{\text{voi}}$ (Table 2.1)
σ_i	i-th singular values corresponding to SVD of $\boldsymbol{A}$ (Equation (2.33))
τ	temporal delay of scanning w.r.t. injection (Equation (4.1))
χ	reconstruction of point object (Equation (3.12))
χ_{art}	component of χ describing artifact due to time-varying attenuation values (Equation (3.21))
$\bar{\chi}_{\text{art}}$	measure for mean reconstruction artifact due to time-varying attenuation values (Equation (4.17))
χ_{static}	χ for a static object (Equation (3.19))
$\chi_{\text{theoretical}}$	χ for a theoretically exact reconstruction (Equation (3.18))
ω_{s}	angular velocity of the C-arm (Section 3.2)

Abbreviations

3DRA	3-dimensional rotational angiography (Section 1.3.1)
AIF	arterial input function (Section 2.2.1)
AUC	area under curve (Section 2.2.4)
BAT	bolus arrival time (Section 2.2.4)
BBB	blood-brain barrier (Section 2.2.1)
CBF	cerebral blood flow (Section 2.2.1)
CBV	cerebral blood volume (Section 2.2.1)
CCA	common carotid artery (Section 5.1)
CPU	central processing unit (Section 6.2.2)
CS	cubic spline (Section 4.2.4)
CSF	cerebrospinal fluid (Section 2.4.3)
CT	computed tomography (Section 1.2)
CTA	computed tomography angiography (Section 1.2)
CUDA	compute unified device architecture (Section 6.2.2)
CVM	contrast agent volume map (Section 5.2.3)
DCMTK	Dicom Toolkit (Section 6.2.2)
DICOM	digital imaging and communications in medicine (Section 6.2.2)
DSA	digital subtraction angiography (Section 1.3.1)
DSC-MRI	dynamic susceptibility contrast – magnetic resonance imaging (Section 2.4.1)
DWPSF	derivative-weighted point spread function (Section 3.3.2)
ECG	electrocardiogram (Section 4.2.1)
EPI	echo-planar imaging (Section 2.4.1)
FD-CT	flat-detector computed tomography (Section 1.3.1)
FDK	Feldkamp-Davis-Kress (Section 3.6)
FM	first moment (Section 2.2.4)
fMRI	functional magnetic resonance imaging (Section 2.4.1)
FT	Fourier transform (Section 2.3.3)
FWHM	full width at half maximum (Section 3.4.3)
Gd	gadolinium (Section 2.2.1)
GPGPU	general-purpose computing on graphics processing units (Section 3.1.1)
GT	ground truth (Section 4.3.2)
GUI	graphical user interface (Section 6.2.1)
Hct	hematocrit (Section 2.4.5)
HIP	Hermite interpolating polynomial (Section 4.2.4)

HU	Hounsfield unit (Section 1.3.1)
IA	intra-arterial (Section 1.2)
IR	injection rate (Section 5.3.2)
IS	interleaved scanning (Section 4.2.2)
IS-PRI	interleaved scanning – partial reconstruction interpolation (Section 4.2.3)
ITK	Insight Toolkit (Section 6.2.2)
IV	intra-venous (Section 1.2)
LIN	linear (Section 4.2.4)
MI	mutual information (Section 6.2.2)
MLEM	maximum likelihood expectation maximization (Section 2.3.3)
MPR	multi-planar reconstruction (Section 6.2.1)
MR	magnetic resonance (Section 1.2)
MRI	magnetic resonance imaging (Section 1.2)
MSCT	multi-slice computed tomography (Section 1.3.1)
MTT	mean transit time (Section 2.2.1)
NN	nearest neighbor (Section 4.2.4)
OI	oscillation index (Section 2.3.4)
PCT	perfusion computed tomography (Section 1.2)
PDF	probability density function (Section 2.2.1)
PFBP	partial filtered backprojection (Section 4.2.3)
PRI	partial reconstruction interpolation (Section 4.2.3)
PSF	point spread function (Section 3.3.2)
RBF	radial basis function (Section 4.2.4)
ROI	region of interest (Section 4.3.1)
SD	standard deviation (Section 4.4.2)
SNR	signal-to-noise ratio (Section 2.2.1)
SPECT	single-photon emission computed tomography (Section 3.1.2)
SVD	singular value decomposition (Section 2.3.2)
TAC	time-attenuation curve (Section 2.3.2)
TCC	time-concentration curve (Section 2.1)
TMAX	time-to-maximum (of flow-scaled residue function) (Section 2.3.1)
tMIP	temporal maximum intensity projection (Section 5.2.2)
TSVD	truncated singular value decomposition (Section 2.3.2)
TTP	time-to-peak (Section 2.2.4)
VOI	volume of interest (Section 2.2.1)
VPE	vascular pixel elimination (Section 4.4.1)
VTK	Visualization Toolkit (Section 6.2.2)
WHO	world health organization (Section 1.2)
XRII	X-ray image intensifier (Section 3.1.2)

Bibliography

[1] World Health Organization (WHO), "The top ten causes of death," Fact Sheet No. 310, November 2008.

[2] N. I. H. Papamitsakis and R. J. Adams, *A Primer on Stroke Prevention and Treatment: An Overview based on AHA/ASA Guidelines*, 1st ed. West Sussex, UK: Wiley-Blackwell, 2009, ch. Primordial and Primary Prevention of Stroke, pp. 23–34.

[3] R. G. González, J. A. Hirsch, W. J. Koroshetz, M. H. Lev, and P. W. Schaefer, Eds., *Acute Ischemic Stroke*, 1st ed. Berlin, Germany: Springer, 2006.

[4] H. P. Adams, G. del Zoppo, M. J. Alberts, D. L. Bhatt, L. Brass, A. Furlan, R. L. Grubb, R. T. Higashida, E. C. Jauch, C. Kidwell, P. D. Lyden, L. B. Morgenstern, A. I. Qureshi, R. H. Rosenwasser, P. A. Scott, and E. F. Wijdicks, "Guidelines for the early management of adults with ischemic stroke," *Stroke*, vol. 38, no. 5, pp. 1655–1711, 2007.

[5] J. L. Saver, "Time is brain — quantified," *Stroke*, vol. 37, no. 1, pp. 263–266, 2006.

[6] A. Srinivasan, M. Goyal, F. A. Azri, and C. Lum, "State-of-the-art imaging of acute stroke," *Radiographics*, vol. 26, no. suppl 1, pp. S75–S95, 2006.

[7] K. Nedeltchev, M. Arnold, C. Brekenfeld, J. Isenegger, L. Remonda, G. Schroth, and H. P. Mattle, "Pre- and in-hospital delays from stroke onset to intra-arterial thrombolysis," *Stroke*, vol. 34, no. 5, pp. 1230–1234, 2003.

[8] M. Moonis, "Intraarterial thrombolysis within the first three hours after acute ischemic stroke in selected patients," *Stroke*, vol. 40, no. 7, pp. 2611–2612, 2009.

[9] H. Ferral and J. Lorenz, Eds., *Interventional radiology*, 1st ed. New York, USA: Thieme, 2010.

[10] R. Fahrig, A. Fox, S. Lownie, and D. Holdsworth, "Use of a C-arm system to generate true three-dimensional computed rotational angiograms: preliminary in vitro and in vivo results," *American Journal of Neuroradiology*, vol. 18, pp. 1507–1514, 1997.

[11] M. Grass, R. Koppe, E. Klotz, R. Proksa, M. H. Kuhn, H. Aerts, J. Op de Beek, and R. Kemkers, "Three-dimensional reconstruction of high contrast objects using C-arm image intensifier projection data," *Computerized Medical Imaging and Graphics*, vol. 23, no. 6, pp. 311–321, 1999.

[12] W. A. Kalender and Y. Kyriakou, "Flat-detector computed tomography (FD-CT)," *European Radiology*, vol. 17, no. 11, pp. 2767–2779, 2007.

[13] N. Strobel, O. Meissner, J. Boese, T. Brunner, B. Heigl, M. Hoheisel, G. Lauritsch, M. Nagel, M. Pfister, E.-P. Rührnschopf, B. Scholz, B. Schreiber, M. Spahn, M. Zellerhoff, and K. Klingenbeck-Regn, *Multislice CT*, 3rd ed. Berlin, Germany: Springer, 2009, ch. 3D Imaging with Flat-Detector C-Arm Systems, pp. 33–51.

[14] A. C. Kak and M. Slaney, *Principles of Computerized Tomographic Imaging*, 1st ed. New York, USA: IEEE Press, 1988.

[15] T. M. Buzug, *Computed Tomography: From Photon Statistics to Modern Cone-Beam CT*, 1st ed. Berlin, Germany: Springer, 2008.

[16] L. A. Feldkamp, L. C. Davis, and J. W. Kress, "Practical cone-beam algorithm," *Journal of the Optical Society of America*, vol. A1, pp. 612–619, 1984.

[17] G. Lauritsch, J. Boese, L. Wigström, H. Kemeth, and R. Fahrig, "Towards cardiac C-arm computed tomography," *IEEE Transactions on Medical Imaging*, vol. 25, no. 7, pp. 922–934, 2006.

[18] M. Prümmer, J. Hornegger, G. Lauritsch, L. Wigström, E. Girard-Hughes, and R. Fahrig, "Cardiac C-arm CT: a unified framework for motion estimation and dynamic CT," *IEEE Transactions on Medical Imaging*, vol. 28, no. 11, pp. 1836–1849, 2009.

[19] C. Rohkohl, G. Lauritsch, L. Biller, M. Prümmer, J. Boese, and J. Hornegger, "Interventional 4D motion estimation and reconstruction of cardiac vasculature without motion periodicity assumption," *Medical Image Analysis*, vol. 14, no. 5, pp. 687–694, 2010.

[20] M. Zellerhoff, Y. Deuerling-Zheng, C. M. Strother, A. Ahmed, K. Pulfer, T. Redel, K. Royalty, J. Grinde, and D. Consigny, "Measurement of cerebral blood volume using angiographic C-arm systems," in *Proc. SPIE Medical Imaging 2009: Biomedical Applications in Molecular, Structural, and Functional Imaging,*, vol. 7262, Lake Buena Vista, USA, 2009, pp. 72620H1–8.

[21] T. Struffert, Y. Deuerling-Zheng, S. Kloska, T. Engelhorn, J. Boese, M. Zellerhoff, S. Schwab, and A. Dörfler, "Cerebral blood volume imaging by flat detector computed tomography in comparison to conventional multislice perfusion CT," *European Radiology*, vol. 21, no. 4, pp. 882–889, 2011.

[22] A. Fieselmann, A. Ganguly, Y. Deuerling-Zheng, M. Zellerhoff, J. Boese, J. Hornegger, and R. Fahrig, "A dynamic reconstruction approach for cerebral blood flow quantification with an interventional C-arm CT," in *Proc. IEEE International Symposium on Biomedical Imaging 2010*, Rotterdam, The Netherlands, 2010, pp. 53–56.

[23] A. Fieselmann, A. Ganguly, Y. Deuerling-Zheng, M. Zellerhoff, C. Rohkohl, J. Boese, J. Hornegger, and R. Fahrig, "Interventional 4-D C-arm CT perfusion imaging using interleaved scanning and partial reconstruction interpolation," *IEEE Transactions on Medical Imaging*, (in press).

[24] A. Fieselmann, A. Ganguly, Y. Deuerling-Zheng, M. Zellerhoff, M. Marks, J. Boese, and R. Fahrig, "Volume cerebral blood flow (CBF) measurement using an interventional ceiling-mounted C-arm angiography system," in *Proc. Annual Scientific Meeting ESR 2010*, Vienna, Austria, 2010, p. S186.

[25] A. Ganguly, A. Fieselmann, M. Marks, J. Rosenberg, J. Boese, Y. Deuerling-Zheng, M. Straka, G. Zaharchuk, R. Bammer, and R. Fahrig, "Cerebral CT perfusion using an interventional C-arm imaging system: Cerebral blood flow measurements," *American Journal of Neuroradiology*, vol. 32, no. 8, pp. 1525–1531, 2011.

[26] A. Ganguly, A. Fieselmann, J. Boese, C. Rohkohl, J. Hornegger, and R. Fahrig, "Evaluating the feasibility of C-arm CT for brain perfusion imaging: an in vitro study," in *Proc. SPIE Medical Imaging 2010: Visualization, Image-Guided Procedures, and Modeling*, vol. 7625, San Diego, USA, 2010, pp. 76250K1–8.

[27] A. Fieselmann, F. Dennerlein, Y. Deuerling-Zheng, J. Boese, R. Fahrig, and J. Hornegger, "A model for filtered backprojection reconstruction artifacts due to time-varying attenuation values in perfusion C-arm CT," *Physics in Medicine and Biology*, vol. 56, no. 12, pp. 3701–3717, 2011.

[28] A. Fieselmann, F. Dennerlein, Y. Deuerling-Zheng, J. Boese, R. Fahrig, and J. Hornegger, "A filter model to analyze reconstruction artifacts in perfusion C-arm CT," in *Proc. IEEE Nuclear Science Symposium and Medical Imaging Conference 2010*, Knoxville, USA, 2010, pp. 2239–2242.

[29] A. Fieselmann, M. Kowarschik, A. Ganguly, J. Hornegger, and R. Fahrig, "Deconvolution-based CT and MR brain perfusion measurement: Theoretical model revisited and practical implementation details," *International Journal of Biomedical Imaging*, vol. 2011, article ID 467563, 20 pages, 2011.

[30] A. Fieselmann, A. Ganguly, Y. Deuerling-Zheng, J. Boese, J. Hornegger, and R. Fahrig, "Automatic measurement of contrast bolus distribution in carotid arteries using a C-arm angiography system to support interventional perfusion imaging," in *Proc. SPIE Medical Imaging 2011: Visualization, Image-Guided Procedures, and Modeling*, vol. 7964, Lake Buena Vista, USA, 2011, pp. 79641W1–6.

[31] A. Fieselmann, A. Ganguly, Y. Deuerling-Zheng, J. Boese, R. Fahrig, and J. Hornegger, "Using a C-arm CT for interventional perfusion imaging: a phantom study to measure linearity between iodine concentration and Hounsfield values," in *Proc. Annual Meeting DGMP 2010*, Freiburg i. Br., Germany, 2010.

[32] K. A. Miles and M. R. Griffiths, "Perfusion CT: a worthwhile enhancement?" *British Journal of Radiology*, vol. 76, no. 904, pp. 220–231, 2003.

[33] G. Brix, J. Griebel, F. Kiessling, and F. Wenz, "Tracer kinetic modelling of tumour angiogenesis based on dynamic contrast-enhanced CT and MRI measurements," *European Journal of Nuclear Medicine and Molecular Imaging*, vol. 37, no. Suppl 1, pp. S30–S51, 2010.

[34] L. Østergaard, *Clinical MR Neuroimaging: Physiological and Functional Techniques*, 2nd ed. Cambridge, UK: Cambridge University Press, 2009, ch. Cerebral perfusion imaging by exogenous contrast agents, pp. 86–93.

[35] A. A. Konstas, G. V. Goldmakher, T.-Y. Lee, and M. H. Lev, "Theoretic basis and technical implementations of CT perfusion in acute ischemic stroke, part 1: Theoretic basis," *American Journal of Neuroradiology*, vol. 30, no. 4, pp. 662–668, 2009.

[36] K. A. Miles and C.-A. Cuenod, Eds., *Multidetector Computed Tomography in Oncology: CT Perfusion Imaging*, 1st ed. London, UK: Informa Healthcare, 2007.

[37] T.-Y. Lee, *Multidetector Computed Tomography in Cerebrovascular Disease: CT Perfusion Imaging*, 1st ed. London, UK: Informa Healthcare, 2007, ch. Scientific basis and validation, pp. 13–27.

[38] M. Mischi, J. A. den Boer, and H. H. M. Korsten, "On the physical and stochastic representation of an indicator dilution curve as a gamma variate," *Physiological Measurement*, vol. 29, pp. 281–294, 2008.

[39] S. K. Shetty and M. H. Lev, *Acute Ischemic Stroke: Imaging and Intervention*, 1st ed. Berlin, Germany: Springer, 2006, ch. CT Perfusion (CTP), pp. 87–113.

[40] J. Hsieh, *Computed Tomography: Principles, Design, Artifacts, and Recent Advances*, 2nd ed. Bellingham, USA: SPIE Publications, 2009.

[41] K. L. Zierler, "Indicator dilution methods for measuring blood flow, volume, and other properties of biological systems: A brief history and memoir," *Annals of Biomedical Engineering*, vol. 28, no. 8, pp. 836–848, 2000.

[42] F. Risse, *MRI of the Lung*, 1st ed. Berlin, Germany: Springer, 2009, ch. MR Perfusion in the Lung, pp. 25–34.

[43] P. V. Pandharipande, G. A. Krinsky, H. Rusinek, and V. S. Lee, "Perfusion imaging of the liver: Current challenges and future goals," *Radiology*, vol. 234, no. 3, pp. 661–673, 2005.

[44] M. Notohamiprodjo, M. F. Reiser, and S. P. Sourbron, "Diffusion and perfusion of the kidney," *European Journal of Radiology*, vol. 76, no. 3, pp. 337–347, 2010.

[45] T.-Y. Lee and B. Murphy, *Multidetector Computed Tomography in Cerebrovascular Disease: CT Perfusion Imaging*, 1st ed. London, UK: Informa Healthcare, 2007, ch. Implementing deconvolution analysis for perfusion CT, pp. 29–46.

[46] G. N. Stewart, "Researches on the circulation time in organs and on the influences which affect it: Parts I–III," *The Journal of Physiology*, vol. 15, no. 1-2, pp. 1–89, 1893.

[47] R. B. Buxton, *Introduction to Functional Magnetic Resonance Imaging: Principles and Techniques*, 1st ed. Cambridge, UK: Cambridge University Press, 2002.

[48] S. Christensen, K. Mouridsen, O. Wu, N. Hjort, H. Karstoft, G. Thomalla, J. Rother, J. Fiehler, T. Kucinski, and L. Østergaard, "Comparison of 10 perfusion MRI parameters in 97 sub-6-hour stroke patients using voxel-based receiver operating characteristics analysis," *Stroke*, vol. 40, no. 6, pp. 2055–2061, 2009.

[49] V. G. Kiselev, "On the theoretical basis of perfusion measurements by dynamic susceptibility contrast MRI," *Magnetic Resonance in Medicine*, vol. 46, no. 6, pp. 1113–1122, 2001.

[50] M. Wintermark, B. C. Lau, J. Chien, and S. Arora, "The anterior cerebral artery is an appropriate arterial input function for perfusion-CT processing in patients with acute stroke," *Neuroradiology*, vol. 50, no. 3, pp. 227–236, 2008.

[51] F. Calamante, D. G. Gadian, and A. Connelly, "Delay and dispersion effects in dynamic susceptibility contrast MRI: Simulations using singular value decomposition," *Magnetic Resonance in Medicine*, vol. 44, no. 3, pp. 466–473, 2000.

[52] L. H. Cheong, T. S. Koh, and Z. Hou, "An automatic approach for estimating bolus arrival time in dynamic contrast MRI using piecewise continuous regression models," *Physics in Medicine and Biology*, vol. 48, no. 5, pp. N83–N88, 2003.

[53] L. C. Shih, J. L. Saver, J. R. Alger, S. Starkman, M. C. Leary, F. Vinuela, G. Duckwiler, Y. P. Gobin, R. Jahan, J. P. Villablanca, P. M. Vespa, and C. S. Kidwell, "Perfusion-weighted magnetic resonance imaging thresholds identifying core, irreversibly infarcted tissue," *Stroke*, vol. 34, no. 6, pp. 1425–1430, 2003.

[54] F. Calamante, S. Christensen, P. M. Desmond, L. Østergaard, S. M. Davis, and A. Connelly, "The physiological significance of the time-to-maximum (Tmax) parameter in perfusion MRI," *Stroke*, vol. 41, no. 6, pp. 1169–1174, 2010.

[55] L. Willats, A. Connelly, and F. Calamante, "Improved deconvolution of perfusion MRI data in the presence of bolus delay and dispersion," *Magnetic Resonance in Medicine*, vol. 56, no. 1, pp. 146–156, 2006.

[56] L. Willats, A. Connelly, and F. Calamante, "Minimising the effects of bolus dispersion in bolus-tracking MRI," *NMR in Biomedicine*, vol. 21, no. 10, pp. 1126–1137, 2008.

[57] L. Østergaard, R. M. Weisskoff, D. A. Chesler, C. Gyldensted, and B. R. Rosen, "High resolution measurement of cerebral blood flow using intravascular tracer bolus passages. part I: Mathematical approach and statistical analysis," *Magnetic Resonance in Medicine*, vol. 36, no. 5, pp. 715–725, 1996.

[58] S. Sourbron, R. Luypaert, D. Morhard, K. Seelos, M. Reiser, and M. Peller, "Deconvolution of bolus-tracking data: a comparison of discretization methods," *Physics in Medicine and Biology*, vol. 52, no. 22, pp. 6761–6778, 2007.

[59] O. Wu, L. Østergaard, R. M. Weisskoff, T. Benner, B. R. Rosen, and A. G. Sorensen, "Tracer arrival timing-insensitive technique for estimating flow in MR perfusion-weighted imaging using singular value decomposition with a block-circulant deconvolution matrix," *Magnetic Resonance in Medicine*, vol. 50, no. 1, pp. 164–174, 2003.

[60] H.-J. Wittsack, A. M. Wohlschläger, E. K. Ritzl, R. Kleiser, M. Cohnen, R. J. Seitz, and M. U., "CT-perfusion imaging of the human brain: advanced deconvolution analysis using circulant singular value decomposition," *Computerized Medical Imaging and Graphics*, vol. 32, no. 1, pp. 67–77, 2008.

[61] G. H. Golub and C. F. Van Loan, *Matrix Computations*, 3rd ed. Baltimore, USA: The Johns Hopkins University Press, 1996.

[62] W. H. Press, S. A. Teukolsky, W. T. Vetterling, and B. P. Flannery, *Numerical Recipes*, 3rd ed. Cambridge, UK: Cambridge University Press, 2007.

[63] P. C. Hansen, "Deconvolution and regularization with Toeplitz matrices," *Numerical Algorithms*, vol. 29, no. 4, pp. 323–378, 2002.

[64] P. C. Hansen, *Discrete Inverse Problems: Insight and Algorithms*, 1st ed. Philadelphia, USA: SIAM, 2010.

[65] P. C. Hansen, "Regularization tools version 4.0 for Matlab 7.3," *Numerical Algorithms*, vol. 46, no. 2, pp. 189–194, 2007.

[66] P. A. Jansson, Ed., *Deconvolution of Images and Spectra*, 2nd ed. New York, USA: Academic Press, 1997.

[67] G. T. Gobbel and J. R. Fike, "A deconvolution method for evaluating indicator-dilution curves," *Physics in Medicine and Biology*, vol. 39, no. 11, pp. 1833–1854, 1994.

[68] R. Wirestam and F. Ståhlberg, "Wavelet-based noise reduction for improved deconvolution of time-series data in dynamic susceptibility-contrast MRI," *Magnetic Resonance Materials in Physics, Biology and Medicine*, vol. 18, no. 3, pp. 113–118, 2005.

[69] K. A. Rempp, G. Brix, F. Wenz, C. R. Becker, F. Gückel, and W. J. Lorenz, "Quantification of regional cerebral blood flow and volume with dynamic susceptibility contrast-enhanced MR imaging," *Radiology*, vol. 193, no. 3, pp. 637–641, 1994.

[70] D. Alsop and G. Schlaug, "The equivalence of SVD and Fourier deconvolution for dynamic susceptibility contrast analysis," in *Proc. Joint Annual Meeting ISMRM-ESMRMB 2001*, Glasgow, UK, 2001, p. 1581.

[71] M. Salluzzi, R. Frayne, and M. R. Smith, "An alternative viewpoint of the similarities and differences of SVD and FT deconvolution algorithms used for quantitative MR perfusion studies," *Magnetic Resonance in Medicine*, vol. 23, no. 3, pp. 481–492, 2005.

[72] P. Gall, P. Emerich, B. F. Kjølby, E. Kellner, I. Mader, and V. G. Kiselev, "On the design of filters for Fourier and oSVD-based deconvolution in bolus tracking perfusion MRI," *Magnetic Resonance Materials in Physics, Biology and Medicine*, vol. 23, no. 3, pp. 187–195, 2010.

[73] P. Gall, B. F. Kjølby, and V. G. Kiselev, "Equivalence of Fourier and oSVD deconvolution in dynamic perfusion measurements: Mutual filter transform," in *Proc. Joint Annual Meeting ISMRM-ESMRMB 2007*, Berlin, Germany, 2007, p. 1441.

[74] J. R. Petrella and J. M. Provenzale, "MR perfusion imaging of the brain: Techniques and applications," *American Journal of Roentgenology*, vol. 175, no. 1, pp. 207–219, 2000.

[75] K. B. Larson, W. H. Perman, J. S. Perlmutter, M. H. Gado, J. M. Ollinger, and K. L. Zierler, "Tracer-kinetic analysis for measuring regional cerebral blood flow by dynamic nuclear magnetic resonance imaging," *Journal of Theoretical Biology*, vol. 170, no. 1, pp. 1–14, 1994.

[76] W. G. Schreiber, F. Gückel, P. Stritzke, P. Schmiedek, A. Schwartz, and G. Brix, "Cerebral blood flow and cerebrovascular reserve capacity: estimation by dynamic magnetic resonance imaging," *Journal of Cerebral Blood Flow & Metabolism*, vol. 18, no. 10, pp. 1143–1156, 1998.

[77] E. P. Vonken, F. J. Beekman, C. J. Bakker, and M. A. Viergever, "Maximum likelihood estimation of cerebral blood flow in dynamic susceptibility contrast MRI," *Magnetic Resonance in Medicine*, vol. 41, no. 2, pp. 343–350, 1999.

[78] I. K. Andersen, A. Szymkowiak, C. E. Rasmussen, L. G. Hanson, J. R. Marstrand, H. B. Larsson, and L. K. Hansen, "Perfusion quantification using Gaussian process deconvolution," *Magnetic Resonance in Medicine*, vol. 48, no. 2, pp. 351–361, 2002.

[79] F. Zanderigo, A. Bertoldo, G. Pillonetto, and C. Cobelli, "Nonlinear stochastic regularization to characterize tissue residue function in bolus-tracking MRI: Assessment and comparison with SVD, block-circulant SVD, and Tikhonov," *IEEE Transactions on Biomedical Engineering*, vol. 56, no. 5, pp. 1287–1297, 2009.

[80] J. C. Kosior and R. Frayne, "PerfTool: A software platform for investigating bolus-tracking perfusion imaging quantification strategies," *Journal of Magnetic Resonance Imaging*, vol. 25, no. 3, pp. 653–659, 2007.

[81] K. Kudo, M. Sasaki, K. Yamada, S. Momoshima, H. Utsunomiya, H. Shirato, and K. Ogasawara, "Differences in CT perfusion maps generated by different commercial software: Quantitative analysis by using identical source data of acute stroke patients," *Radiology*, vol. 254, no. 1, pp. 200–209, 2010.

[82] A. A. Konstas, G. V. Goldmakher, T.-Y. Lee, and M. H. Lev, "Theoretic basis and technical implementations of CT perfusion in acute ischemic stroke, part 2: Technical implementations," *American Journal of Neuroradiology*, vol. 30, no. 5, pp. 885–892, 2009.

[83] S. Sourbron, M. Dujardin, S. Makkat, and R. Luypaert, "Pixel-by-pixel deconvolution of bolus-tracking data: optimization and implementation," *Physics in Medicine and Biology*, vol. 52, no. 2, pp. 429–447, 2007.

[84] P. C. Hansen, "Analysis of discrete ill-posed problems by means of the L-curve," *SIAM Review*, vol. 34, no. 4, pp. 561–580, 1992.

[85] F. Calamante, D. G. Gadian, and A. Connelly, "Quantification of bolus-tracking MRI: Improved characterization of the tissue residue function using Tikhonov regularization," *Magnetic Resonance in Medicine*, vol. 50, no. 6, pp. 1237–1247, 2003.

[86] S. Sourbron, R. Luypaert, P. V. Schuerbeek, M. Dujardin, and T. Stadnik, "Choice of the regularization parameter for perfusion quantification with MRI," *Physics in Medicine and Biology*, vol. 49, no. 14, pp. 3307–3324, 2004.

[87] A. Fieselmann, F. Risse, C. Fink, and W. Semmler, "A novel method to determine the Tikhonov regularization parameter for pulmonary perfusion quantification with MRI," in *Proc. Joint Annual Meeting ISMRM-ESMRMB 2007*, Berlin, Germany, 2007, p. 2764.

[88] A. M. Smith, C. B. Grandin, T. Duprez, F. Mataigne, and G. Cosnard, "Whole brain quantitative CBF, CBV, and MTT measurements using MRI bolus tracking: implementation and application to data acquired from hyperacute stroke patients," *Journal of Magnetic Resonance Imaging*, vol. 12, no. 3, pp. 400–410, 2000.

[89] L. Zhang, C. Chefd'hotel, and G. Bousquet, "Group-wise motion correction of brain perfusion images," in *Proc. IEEE International Symposium on Biomedical Imaging 2010*, Rotterdam, The Netherlands, 2010, pp. 832–835.

[90] T. R. Oakes, T. Johnstone, K. S. Ores Walsh, L. L. Greischar, A. L. Alexander, A. S. Fox, and R. J. Davidson, "Comparison of fMRI motion correction software tools," *Neuroimage*, vol. 28, no. 3, pp. 529–543, 2005.

[91] R. K. Kosior, J. C. Kosior, and R. Frayne, "Improved dynamic susceptibility contrast (DSC)-MR perfusion estimates by motion correction," *Journal of Magnetic Resonance Imaging*, vol. 26, no. 4, pp. 1167–1172, 2007.

[92] N. Saito, K. Kudo, T. Sasaki, M. Uesugi, K. Koshino, M. Miyamoto, and S. Suzuki, "Realization of reliable cerebral-blood-flow maps from low-dose CT perfusion images by statistical noise reduction using nonlinear diffusion filtering," *Radiological Physics and Technology*, vol. 1, no. 1, pp. 62–74, 2008.

[93] P. Montes and G. Lauritsch, "Low-noise dynamic reconstruction for X-ray tomographic perfusion studies using low sampling rates," *International Journal of Biomedical Imaging*, vol. 2009, article ID 108028, 13 pages, 2009.

[94] H. Bruder, R. Raupach, E. Klotz, K. Stierstorfer, and T. Flohr, "Spatio-temporal filtration of dynamic CT data using diffusion filters," in *Proc. SPIE Medical Imaging 2009: Physics of Medical Imaging*, vol. 7258, Orlando, USA, 2009, pp. 7258571–10.

[95] A. M. Mendrik, E.-J. Vonken, B. van Ginneken, H. W. de Jong, A. Riordan, T. van Seeters, E. J. Smit, M. A. Viergever, and M. Prokop, "TIPS bilateral noise reduction in 4D CT perfusion scans produces high-quality cerebral blood flow maps," *Physics in Medicine and Biology*, vol. 56, no. 13, pp. 3857–3872, 2011.

[96] T.-Y. Lee, B. Murphy, X. Chen, and K. A. Miles, *Multidetector Computed Tomography in Cerebrovascular Disease: CT Perfusion Imaging*, 1st ed. London, UK: Informa Healthcare, 2007, ch. Image Processing, pp. 57–69.

[97] J. A. Maldjian, J. Chalela, S. E. Kasner, D. Liebeskind, and J. A. Detre, "Automated CT segmentation and analysis for acute middle cerebral artery stroke," *American Journal of Neuroradiology*, vol. 22, no. 6, pp. 1050–1055, 2001.

[98] K. Kudo, S. Terae, C. Katoh, M. Oka, T. Shiga, N. Tamaki, and K. Miyasaka, "Quantitative cerebral blood flow measurement with dynamic perfusion CT using the vascular-pixel elimination method: Comparison with $H_2^{15}O$ positron emission tomography," *American Journal of Neuroradiology*, vol. 24, no. 3, pp. 419–426, 2003.

[99] P. Dawson, *Textbook of Contrast Media*, 1st ed. London, UK: Informa Healthcare, 1999, ch. Functional and physiological imaging, pp. 75–94.

[100] K. A. Miles, H. Young, S. L. Chica, and P. D. Esser, "Quantitative contrast-enhanced computed tomography: is there a need for system calibration?" *European Radiology*, vol. 17, no. 4, pp. 919–926, 2007.

[101] B. F. Kjølby, L. Østergaard, and V. G. Kiselev, "Theoretical model of intravascular paramagnetic tracers effect on tissue relaxation," *Magnetic Resonance in Medicine*, vol. 56, no. 1, pp. 187–197, 2006.

[102] L. Knutsson, F. Ståhlberg, and R. Wirestam, "Absolute quantification of perfusion using dynamic susceptibility contrast MRI: pitfalls and possibilities," *Magnetic Resonance Materials in Physics, Biology and Medicine*, vol. 23, no. 1, pp. 1–21, 2010.

[103] M. J. van Osch, E.-J. Vonken, M. A. Viergever, J. van der Grond, and C. J. Bakker, "Measuring the arterial input function with gradient echo sequences," *Magnetic Resonance in Medicine*, vol. 49, no. 6, pp. 1067–1076, 2003.

[104] M. Mlynash, I. Eyngorn, R. Bammer, M. Moseley, and D. C. Tong, "Automated method for generating the arterial input function on perfusion-weighted MR imaging: Validation in patients with stroke," *American Journal of Neuroradiology*, vol. 26, no. 6, pp. 1479–1486, 2005.

[105] K. Mouridsen, S. Christensen, L. Gyldensted, and L. Østergaard, "Automatic selection of arterial input function using cluster analysis," *Magnetic Resonance in Medicine*, vol. 55, no. 3, pp. 524–531, 2006.

[106] A. Singh, R. K. S. Rathore, M. Haris, S. K. Verma, N. Husain, and R. K. Gupta, "Improved bolus arrival time and arterial input function estimation for tracer kinetic analysis in DCE-MRI," *Journal of Magnetic Resonance Imaging*, vol. 29, no. 1, pp. 166–176, 2009.

[107] F. Calamante, M. Mørup, and L. K. Hansen, "Defining a local arterial input function for perfusion MRI using independent component analysis," *Magnetic Resonance in Medicine*, vol. 52, no. 4, pp. 789–797, 2004.

[108] L. Knutsson, E. M. Larsson, O. Thilmann, F. Ståhlberg, and R. Wirestam, "Calculation of cerebral perfusion parameters using regional arterial input functions identified by factor analysis," *Journal of Magnetic Resonance Imaging*, vol. 23, no. 4, pp. 444–453, 2006.

[109] R. Grüner, B. T. Bjørnarå, G. Moen, and T. Taxt, "Magnetic resonance brain perfusion imaging with voxel-specific arterial input functions," *Journal of Magnetic Resonance Imaging*, vol. 23, no. 3, pp. 273–284, 2006.

[110] C. Lorenz, T. Benner, P. J. Chen, C. J. Lopez, H. Ay, M. W. Zhu, N. M. Menezes, H. Aronen, J. Karonen, Y. Liu, J. Nuutinen, and A. G. Sorensen, "Automated perfusion-weighted MRI using localized arterial input functions," *Journal of Magnetic Resonance Imaging*, vol. 24, no. 5, pp. 1133–1139, 2006.

[111] W. Lin, A. Celik, C. Derdeyn, H. An, Y. Lee, T. Videen, L. Østergaard, and W. J. Powers, "Quantitative measurements of cerebral blood flow in patients with unilateral carotid artery occlusion: a PET and MR study," *Journal of Magnetic Resonance Imaging*, vol. 14, no. 6, pp. 659–667, 2001.

[112] A. E. Hansen, H. Pedersen, E. Rostrup, and H. B. W. Larsson, "Partial volume effect (PVE) on the arterial input function (AIF) in T1-weighted perfusion imaging and limitations of the multiplicative rescaling approach," *Magnetic Resonance in Medicine*, vol. 62, no. 4, pp. 1055–1059, 2009.

[113] L. Knutsson, S. Börjesson, E.-M. Larsson, J. Risberg, L. Gustafson, U. Passant, F. Ståhlberg, and R. Wirestam, "Absolute quantification of cerebral blood flow in normal volunteers: correlation between Xe-133 SPECT and dynamic susceptibility contrast MRI," *Journal of Magnetic Resonance Imaging*, vol. 26, no. 4, pp. 913–920, 2007.

[114] C. Rohkohl, B. Keck, H. Hofmann, and J. Hornegger, "RabbitCT – an open platform for benchmarking 3D cone-beam reconstruction algorithms," *Medical Physics*, vol. 36, no. 9, pp. 3940–3944, 2009.

[115] X. Pan, E. Sidky, and M. Vannier, "Why do commercial CT scanners still employ traditional, filtered back-projection for image reconstruction?" *Inverse Problems*, vol. 25, no. 12, p. 123009 (36 pp), 2009.

[116] J. E. Holden and W. R. Ip, "Continuous time-dependence in computed tomography," *Medical Physics*, vol. 5, no. 6, pp. 485–490, 1978.

[117] W. R. Ip, J. E. Holden, and S. S. Winkler, "A study of image discrepancies due to object time-dependence in transmission and emission tomography," *Physics in Medicine and Biology*, vol. 28, no. 8, pp. 953–962, 1983.

[118] K. L. Garden, R. Bates, M. Won, and H. Chikwanda, "Computerized tomographic imaging is insensitive to density variation during scanning," *Image and Vision Computing*, vol. 2, no. 2, pp. 76–84, 1984.

[119] B. D. Bok, A. N. Bice, M. Clausen, D. F. Wong, and H. N. Wagner, "Artifacts in camera based single photon emission tomography due to time activity variation," *European Journal of Nuclear Medicine*, vol. 13, no. 9, pp. 439–442, 1987.

[120] K. Nakajima, N. Shuke, J. Taki, T. Ichihara, N. Motomura, H. Bunko, and K. Hisada, "A simulation of dynamic SPECT using radiopharmaceuticals with rapid clearance," *Journal of Nuclear Medicine*, vol. 33, no. 6, pp. 1200–1206, 1992.

[121] R. Fahrig, "Computed rotational angiography: Use of a C-arm-mounted XRII for 3D imaging of intracranial vessels during neuro-interventional procedures," Ph.D. dissertation, University of Western Ontario, London, ON, Canada, 1999.

[122] P. Montes and G. Lauritsch, "A temporal interpolation approach for dynamic reconstruction in perfusion CT," *Medical Physics*, vol. 34, no. 7, pp. 3077–3092, 2007.

[123] M. D. Silver, "A method for including redundant data in computed tomography," *Medical Physics*, vol. 27, no. 4, pp. 773–774, 2000.

[124] M. Ohkubo, S. Wada, S. Ida, M. Kunii, A. Kayugawa, T. Matsumoto, K. Nishizawa, and K. Murao, "Determination of point spread function in computed tomography accompanied with verification," *Medical Physics*, vol. 36, no. 6, pp. 2089–2097, 2009.

[125] G. L. Zeng, "Nonuniform noise propagation by using the ramp filter in fan-beam computed tomography," *IEEE Transactions on Medical Imaging*, vol. 23, no. 6, pp. 690–695, 2004.

[126] E. Siebert, G. Bohner, M. Dewey, F. Masuhr, K. T. Hoffmann, J. Mews, F. Engelken, H. C. Bauknecht, S. Diekmann, and R. Klingebiel, "320-slice CT neuroimaging: initial clinical experience and image quality evaluation," *British Journal of Radiology*, vol. 82, no. 979, pp. 561–570, 2009.

[127] C. Neukirchen, M. Giordano, and S. Wiesner, "An iterative method for tomographic x-ray perfusion estimation in a decomposition model-based approach," *Medical Physics*, vol. 37, no. 12, pp. 6125–6141, 2010.

[128] M. Beister, Y. Kyriakou, and W. Kalender, "Increased temporal resolution for dynamic perfusion CT (PCT) with C-arm flat-detector CT," in *Proc. Scientific Assembly and Annual Meeting of the RSNA 2010*, Chicago, USA, 2010.

[129] C. Neukirchen, "An extended temporal interpolation approach for dynamic object reconstruction," in *Proc. International Meeting on Fully Three-Dimensional Image Reconstruction in Radiology and Nuclear Medicine 2011*, Potsdam, Germany, 2011, pp. 379–382.

[130] M. Wintermark, W. S. Smith, N. U. Ko, M. Quist, P. Schnyder, and W. P. Dillon, "Dynamic perfusion CT: optimizing the temporal resolution and contrast volume for calculation of perfusion CT parameters in stroke patients." *American Journal of Neuroradiology*, vol. 25, no. 5, pp. 720–729, 2004.

[131] M. Wiesmann, S. Berg, G. Bohner, R. Klingebiel, V. Schöpf, B. M. Stoeckelhuber, I. Yousry, J. Linn, and U. Missler, "Dose reduction in dynamic perfusion CT of the brain: effects of the scan frequency on measurements of cerebral blood flow, cerebral blood volume, and mean transit time." *European Radiology*, vol. 18, no. 12, pp. 2967–2974, 2008.

[132] C. T. Badea, S. M. Johnston, E. Subashi, Y. Qi, L. W. Hedlund, and G. A. Johnson, "Lung perfusion imaging in small animals using 4D micro-CT at heartbeat temporal resolution," *Medical Physics*, vol. 37, no. 1, pp. 54–62, 2010.

[133] F. N. Fritsch and R. E. Carlson, "Monotone piecewise cubic interpolation," *SIAM Journal on Numerical Analysis*, vol. 17, pp. 238–246, 1980.

[134] M. D. Buhmann, *Radial Basis Functions: Theory and Implementations*, 1st ed. Cambridge, UK: Cambridge University Press, 2003.

[135] N. Neophytou, F. Xu, and K. Mueller, "Hardware acceleration vs. algorithmic acceleration: Can GPU-based processing beat complexity optimization for CT?" in *Proc. SPIE Medical Imaging 2007: Physics of Medical Imaging*, vol. 6510, San Diego, USA, 2007, pp. 65105F1–9.

[136] P. Montes, "Dynamic cone-beam reconstruction for perfusion computed tomography," Ph.D. dissertation, University of Heidelberg, Germany, 2006.

[137] J. Bredno, M. E. Olszewski, and M. Wintermark, "Simulation model for contrast agent dynamics in brain perfusion scans," *Magnetic Resonance in Medicine*, vol. 6, no. 1, pp. 280–290, 2010.

[138] L. A. Shepp and B. F. Logan, "The Fourier reconstruction of a head section," *IEEE Transactions on Nuclear Science*, vol. NS-21, pp. 21–43, 1974.

[139] A. Fieselmann, "DIPPO — a digital brain perfusion phantom," http://www5.cs.fau.de/~fieselma/data/, accessed April 01, 2011.

[140] P. Sauleaua, E. Lapoublea, D. Val-Lailleta, and C.-H. Malberta, "The pig model in brain imaging and neurosurgery," *The International Journal of Animal Biosciences*, vol. 3, no. 8, pp. 1138–1151, 2009.

[141] D. Morhard, C. D. Wirth, G. Fesl, C. Schmidt, M. F. Reiser, C. R. Becker, and B. Ertl-Wagner, "Advantages of extended brain perfusion computed tomography: 9.6 cm coverage with time resolved computed tomography-angiography in comparison to standard stroke-computed tomography," *Investigative Radiology*, vol. 45, no. 7, pp. 363–369, 2010.

[142] R. Fahrig, R. Dixon, T. Payne, R. Morin, A. Ganguly, and N. Strobel, "Dose and image quality for a cone-beam C-arm CT system," *Medical Physics*, vol. 33, no. 12, pp. 4541–50, 2006.

[143] L. Østergaard, "Principles of cerebral perfusion imaging by bolus tracking," *Journal of Magnetic Resonance Imaging*, vol. 22, no. 6, pp. 710–717, 2005.

[144] M. Wintermark, *Multislice CT*, 3rd ed. Berlin, Germany: Springer, 2009, ch. Cerebral Perfusion CT: Techniques and Clinical Applications, pp. 111–122.

[145] M. Takahashi, H. Bussaka, and N. Nakagawa, "Evaluation of the cerebral vasculature by intraarterial DSA – with emphasis on in vivo resolution," *Neuroradiology*, vol. 26, no. 4, pp. 253–259, 1984.

[146] H. Gray, *Anatomy of the human body*, 20th ed., W. H. Lewis, Ed. Philadelphia, USA: Lea & Febiger, 1918, (reproductions of the images are available at http://en.wikipedia.org/wiki/File:Gray505.png and http://en.wikipedia.org/wiki/File:Gray513.png, accessed May 10, 2011).

[147] C. Kirbas and F. Quek, "A review of vessel extraction techniques and algorithms," *ACM Computing Surveys*, vol. 36, no. 2, pp. 81–121, 2004.

[148] D. Schuldhaus, M. Spiegel, T. Redel, M. Polyanskaya, T. Struffert, J. Hornegger, and A. Dörfler, "2-D vessel segmentation using local adaptive contrast enhancement," in *Proc. Bildverarbeitung für die Medizin 2011*, Lübeck, Germany, 2011, pp. 109–113.

[149] L. Y. Du, J. Umoh, H. N. Nikolov, S. I. Pollmann, T.-Y. Lee, and D. W. Holdsworth, "A quality assurance phantom for the performance evaluation of volumetric micro-CT systems," *Physics in Medicine and Biology*, vol. 52, no. 23, pp. 7087–7108, 2007.

[150] K. Taguchi, Y. Funama, M. Zhang, E. K. Fishman, and J. F. Geschwind, "Quantitative measurement of iodine concentration in the liver using abdominal C-arm computed tomography," *Academic Radiology*, vol. 16, no. 2, pp. 200–208, 2009.

[151] P. Quaet-Faslem and J. Regn, "User interface design for interventional X-ray systems," in *Proc. UPA 2007 Conference – Patterns: Blueprints for Usability*, Austin, USA, 2007.

[152] L. Ibanez, W. Schroeder, L. Ng, and J. Cates, *The ITK Software Guide*, 2nd ed. Clifton Park, USA: Kitware, Inc., 2005.

[153] T. S. Yoo and D. N. Metaxas, "Open science – combining open data and open source software: Medical image analysis with the Insight Toolkit," *Medical Image Analysis*, vol. 9, no. 6, pp. 503–506, 2005.

[154] W. Schroeder, K. Martin, and B. Lorensen, *The Visualization Toolkit: An Object-Oriented Approach To 3D Graphics*, 4th ed. Clifton Park, USA: Kitware, Inc., 2006.

[155] M. Eichelberg, J. Riesmeier, T. Wilkens, A. J. Hewett, A. Barth, and P. Jensch, "Ten years of medical imaging standardization and prototypical implementation: the DICOM standard and the OFFIS DICOM toolkit (DCMTK)," in *Proc. SPIE Medical Imaging 2004: PACS and Imaging Informatics*, vol. 5371, San Diego, USA, 2004, pp. 57–68.

[156] S. Koranne, *Handbook of Open Source Tools*, 1st ed. Berlin, Germany: Springer, 2010.

[157] J. Sanders and E. Kandrot, *CUDA by Example*, 1st ed. Amsterdam, The Netherlands: Addison-Wesley, 2010.

[158] P. Viola and W. M. Wells, III, "Alignment by maximization of mutual information," *International Journal of Computer Vision*, vol. 24, no. 2, pp. 137–154, 1997.

[159] G.-H. Chen, J. Tang, and S. Leng, "Prior image constrained compressed sensing (PICCS): a method to accurately reconstruct dynamic CT images from highly undersampled projection data sets," *Medical Physics*, vol. 35, no. 2, pp. 660–663, 2008.

[160] J. C. Ramirez-Giraldo, J. Trzasko, S. Leng, L. Yu, A. Manduca, and C. H. McCollough, "Nonconvex prior image constrained compressed sensing (NCPICCS): Theory and simulations on perfusion CT," *Medical Physics*, vol. 38, no. 4, pp. 2157–2167, 2011.

[161] H. Botsch, H. Oester, and S. Sattler, "Röntgensystem (X-ray system has C-arm movably arranged on positioning fixture for holding recording system with X-ray detector and X-ray source comprising high voltage generating device for supplying recording system with high voltage)," German patent application DE102009018283A1, April 21, 2009.

[162] J. Boese, M. Maschke, and H.-D. Wolf, "Röntgensystem und Verfahren zum Betrieb eines Röntgensystems (X-ray system, particularly angiography X-ray system for use in cardiology, comprises multiaxle, three-dimensional adjustable robot arm, which is fastened at distal end by fastening element)," German patent application DE102008035195A1, July 28, 2008.

[163] R. J. Lewandowski, J.-F. Geschwind, E. Liapi, and R. Salem, "Transcatheter intraarterial therapies: Rationale and overview," *Radiology*, vol. 259, no. 3, pp. 641–657, 2011.

[164] M. Sasaki, K. Kudo, K. Ogasawara, and S. Fujiwara, "Tracer delay-insensitive algorithm can improve reliability of CT perfusion imaging for cerebrovascular steno-occlusive disease: Comparison with quantitative single-photon emission CT," *American Journal of Neuroradiology*, vol. 30, no. 1, pp. 188–193, 2009.